ISSN 8755-6839

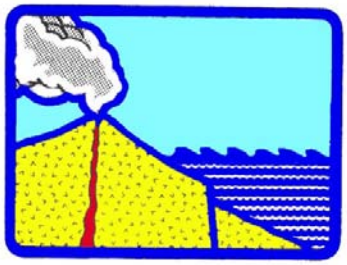

SCIENCE OF TSUNAMI HAZARDS

The International Journal of The Tsunami Society

Volume 25 Number 1 Published Electronically 2006

WWW.STHJOURNAL.ORG

OBJECTIVE: **The Tsunami Society** publishes this journal to increase and disseminate knowledge about tsunamis and their hazards.

DISCLAIMER: Although these articles have been technically reviewed by peers, **The Tsunami Society** is not responsible for the veracity of any statement, opinion or consequences.

Submit manuscripts of articles, notes or letters to the Editor. If an article is accepted for publication the author(s) must submit a scan ready manuscript, a Doc, TeX or a PDF file in the journal format. Issues of the journal are published electronically in PDF format. Recent journal issues are available at

http://www.sthjournal.org.

Tsunami Society members will be advised by e-mail when a new issue is available. There are no page charges or reprints for authors.

Issues of the journal from 1982 thru 2005 are available in PDF format at

http://epubs.lanl.gov/tsunami/

and on a CD-ROM from the Society to Tsunami Society members.

ISSN 8755-6839 **http://www.sthjournal.org**

Published Electronically by The Tsunami Society in Honolulu, Hawaii, USA

EMERGENCY PLANNING IN NORTHERN ALGERIA BASED ON REMOTE SENSING DATA IN RESPECT TO TSUNAMI HAZARD PREPAREDNESS

Barbara Theilen-Willige
Technical University of Berlin, Institute of Applied Geosciences
Department of Hydrology and Bureau of Applied Geoscientific Remote Sensing (BAGF)
Stockach, Germany

ABSTRACT

LANDSAT ETM and Digital Elevation Model (DEM) data from the coastal areas of Algeria were investigated in order to detect traces of earlier tsunami events. Digital image processing methods used to produce morphometric maps - such as hillshade, slope, minimum and maximum curvature maps based on the SRTM DEM data - contribute to the detection of morphologic traces that might be related to catastrophic tsunami events. These maps combined with LANDSAT ETM and seismotectonic data in a GIS environment allow the delineation of areas with potential tsunami risk. The evaluations of LANDSAT ETM imageries merged with digitally processed and enhanced SRTM data clearly show areas that must have been flooded in earlier times. In some cases morphological traces of flood waves as curvilinear scarps open to the seaside or traces of abrasion are clearly visible.

1. INTRODUCTION

Images from earth observing satellites have become a valuable support tool for tsunami damage detection in the aftermath of the disaster. This contribution, however, considers the use of remote sensing data for the detection of traces indicating past, catastrophic tsunami events as it can be assumed that coastal areas that were hit in the past by catastrophic tsunamis might be affected by similar events in the future again. This study concentrates on tsunami risk mapping for areas where no severe tsunami has occurred recently, but the geomorphologic and topographic features and characteristics are similar to areas hit by recent catastrophic tsunamis as Sumatra and where historical records of tsunamis are available and reliable. A tsunami hazard map of such an area that predicts the location of future tsunami occurrences is required. Most detailed maps of those areas susceptible to tsunami flooding are an important step towards disaster preparedness and mitigation.

The coastal areas of Northern Algeria are investigated more detailed with the help of remote sensing data in order to detect typical geomorphologic and hydrologic features assumed to be related to past tsunamis as described in Fig.1. The areas prone to flooding hazard or to landslide hazard are delineated and mapped. These maps could be used as contribution to emergency planning in coastal areas of Algeria.

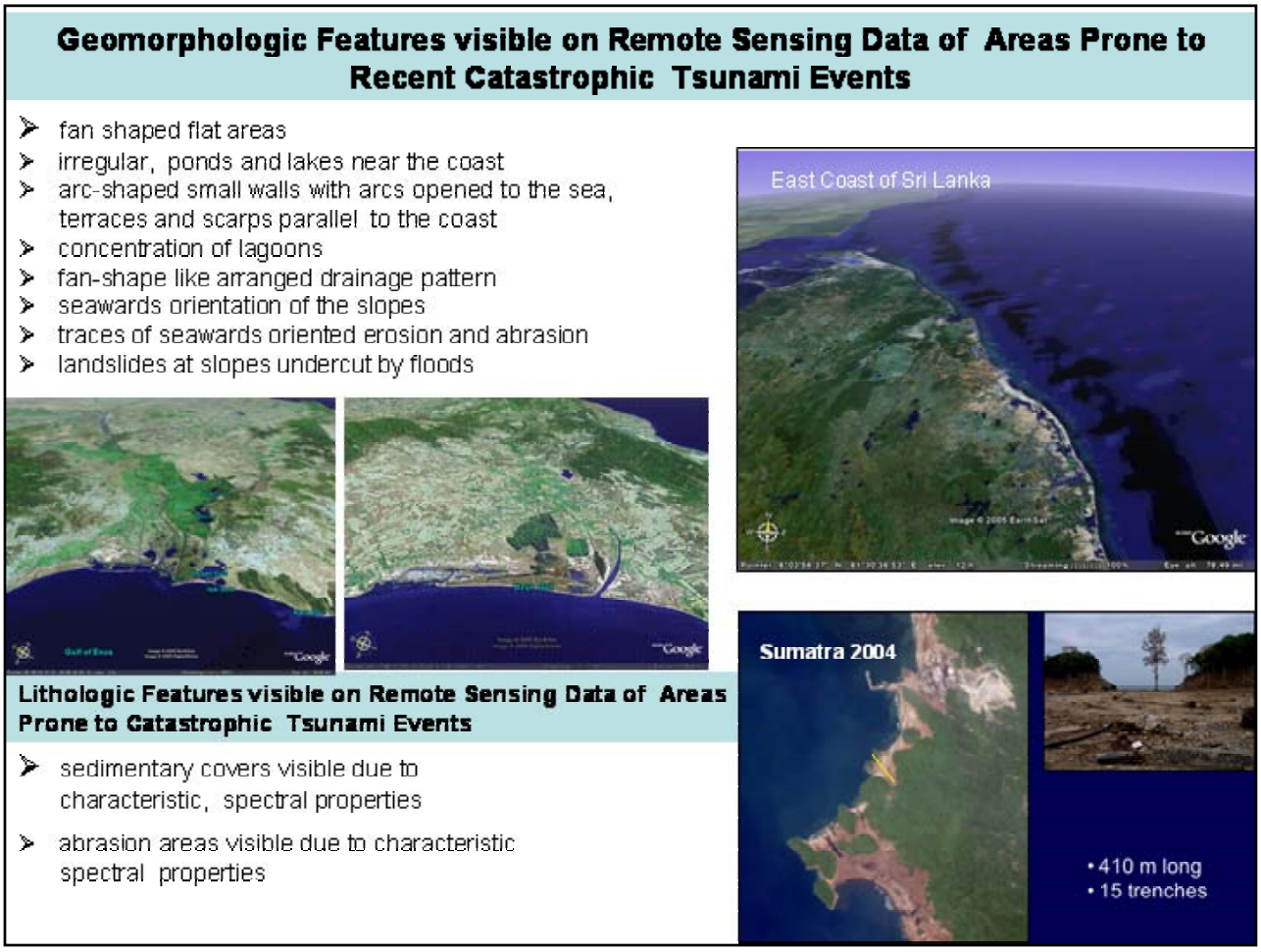

Fig.1: Typical morphologic and hydrologic features of tsunami prone areas

2. APPROACH

A concept of multi-hazard assessment is developed based on remote sensing data and GIS methods. This approach enables to asses the geohazards in respect to their different and complex dependencies. It focuses on a hazard map that might be useful as base for local and regional planning decisions of local governments and stakeholders of the civil society. The findings can be converted to recommendations for the local governments such as towns and villages in order to plan disaster-reducing activities.

This study considers the support provided by remote sensing data, including DEM data acquired by Space Shuttle Missions, and a GIS based spatial databases for the delineation of potential risk sites in Algeria. On a regional scale the areas of potential tsunami risk are determined by an integration of remote sensing data, geologic, seismotectonic and topographic data. The evaluation of digital topographic data is of great importance as it contributes to the detection of the specific geomorphologic/ topographic settings of tsunami prone areas. LANDSAT ETM and DEM data were used as layers for generating a Tsunami Hazard GIS and combined with different geodata and other thematic maps.

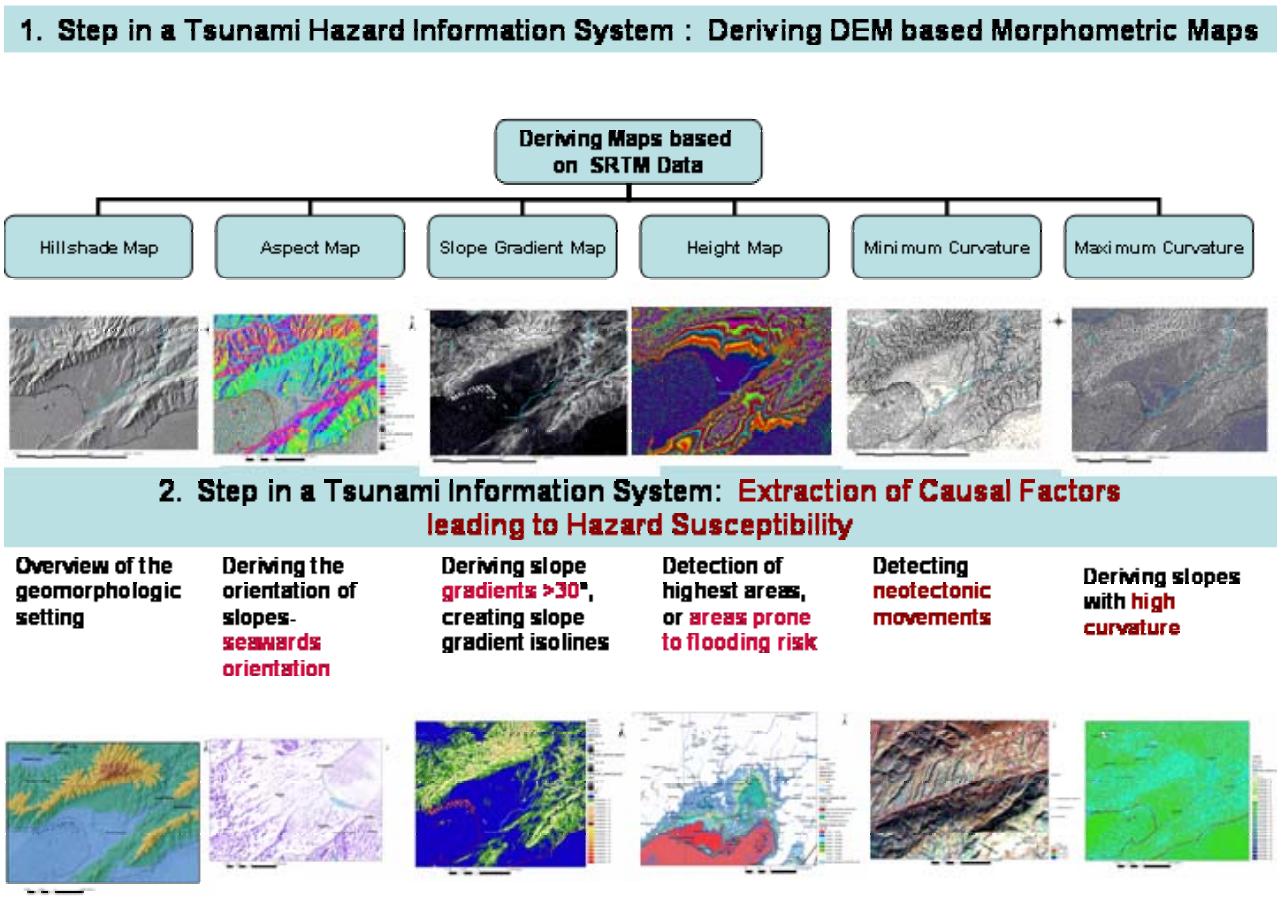

Fig.2: Deriving Morphometric Maps based on SRTM Data and Extraction of Causal Factors leading to Natural Hazards (Theilen-Willige, 2006)

For the objectives of this study digital elevation data have been evaluated: **S**huttle **R**adar **T**opography **M**ission - SRTM, 90 m resolution) data provided by the University of Maryland, Global Land Cover Facility (http://glcfapp.umiacs. umd.edu: 8080/esdi/) and GTOPO30 data provided by USGS (http://www.diva-gis.org/Data.htm, 1 km resolution) were used as base maps.

The digital topographic data were merged with LANDSAT ETM data (Band 8: 15 m resolution). For enhancing the LANDSAT ETM data digital image processing procedures have been carried out. Various image tools delivered by ENVI Software/ CREASO were tested, for example to find the best suited contrast-stretching parameters. With digital image processing techniques maps can be generated to meet specific requirements considering risk mapping. For getting a geomorphologic overview SRTM data terrain parameters were extracted from a DEM as shaded relief, aspect and slope degree, minimum and maximum curvature or plan convexity maps using ENVI and ArcMap software (Fig.3). Many of the morphometric parameters measured from a DEM vary with the size of grid used to model the surface (WOOD, 2002). The various data sets as LANDSAT ETM data, topographic, geological and geophysical data from the study regions were integrated as layers into GIS using the software ArcView GIS 3.3 with the extensions Spatial Analyst und 3D-Analyst and ArcGIS 9.1 of. Other geodata as provided by ESRI ArcIMS Server or USGS Natural Hazards Support System were included, so earthquake data or bathymetric maps. As a complementary tool Google Earth Software was used in order to benefit from the 3D imageries of the various investigation areas (http://earth.google.com/).

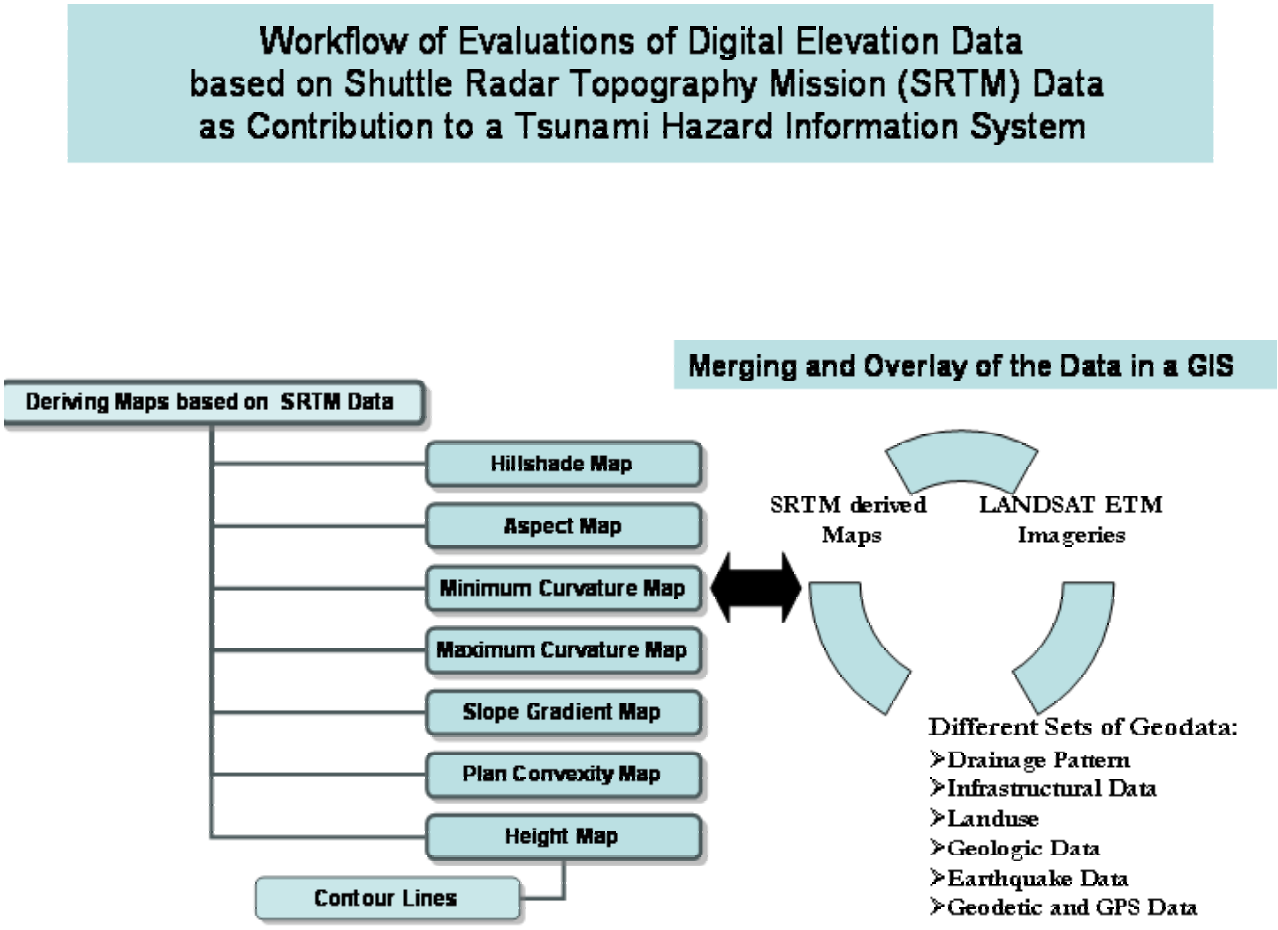

Fig.3: Workflow

Geomorphometric parameters as slope degree, minimum or maximum curvature provides information of the terrain morphology indicating geomorphologic features (see Fig.2) that might be related to tsunami events. These SRTM derived, morphometric parameters correspond to groups of 0, 1st and 2nd order differentials, where the 1st and 2nd order functions have

components in the XY and orthogonal planes. A systematic GIS approach is recommended for tsunami risk site detection as described in Fig.3 extracting geo-morphometric parameters based on the SRTM DEM data as part of a Tsunami Information System. LANDSAT ETM data were used as well for deriving information of surface-near water currents in the coastal areas that might help to a better understanding of the influence of the coastal morphology on streaming mechanisms

Fig.6 including different geodata sets describes the next step schematically

Potential risk sites for hazardous tsunami waves were identified by analyzing areas in Algeria showing heights below 20 m above sea level based on GTOPO30 height data (Fig.4). These areas below 20 m height were studied then more detailed evaluating LANDSAT ETM and SRTM data.

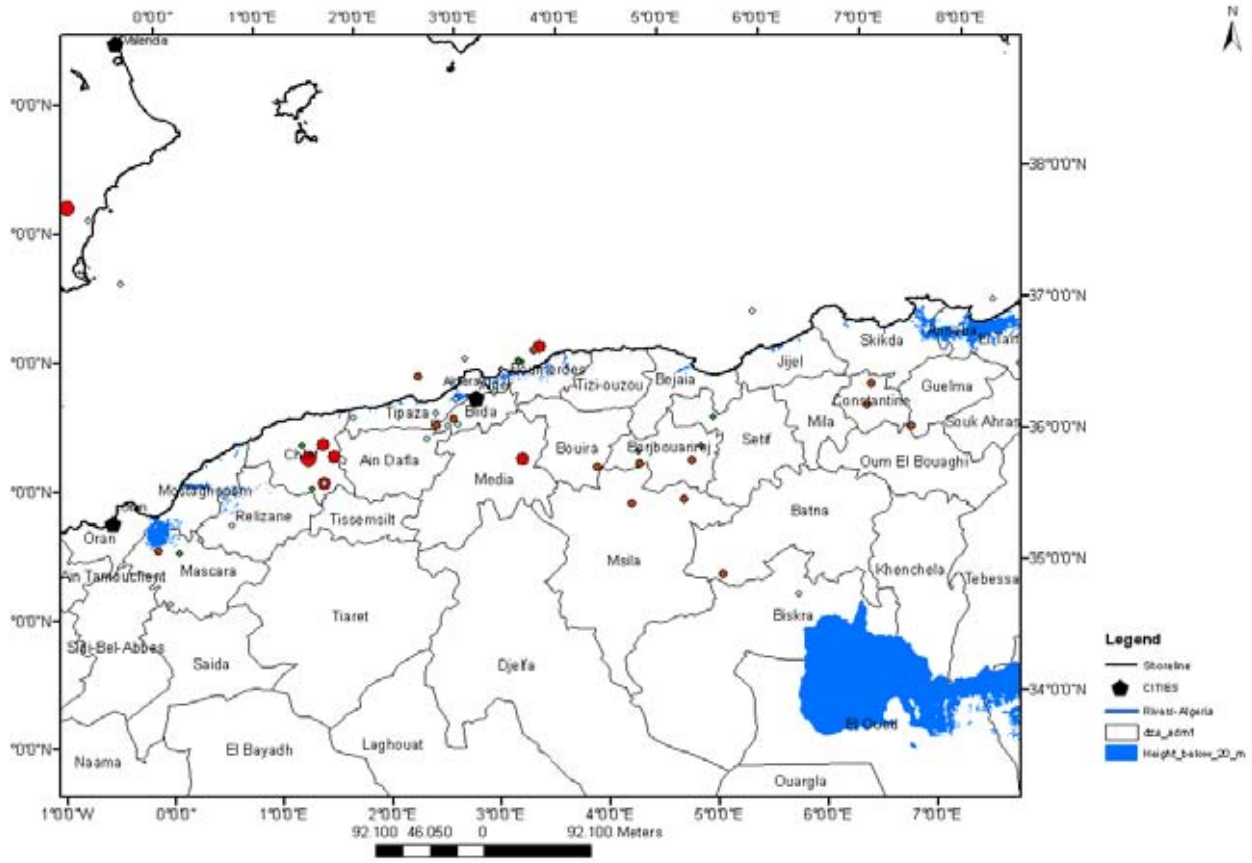

Fig.4: Potential tsunami hazard sites in Algeria

3. EVALUATION OF SRTM AND LANDSAT ETM DATA FROM COASTAL AREAS OF ALGERIA

Investigation areas were selected where the evaluation of SRTM, LANDSAT ETM and other geodata allows the assumption that catastrophic tsunami events might have occurred in the geologic past. As first example the area of Gulf of Stora and Bone/ Northeast Algeria is presented.

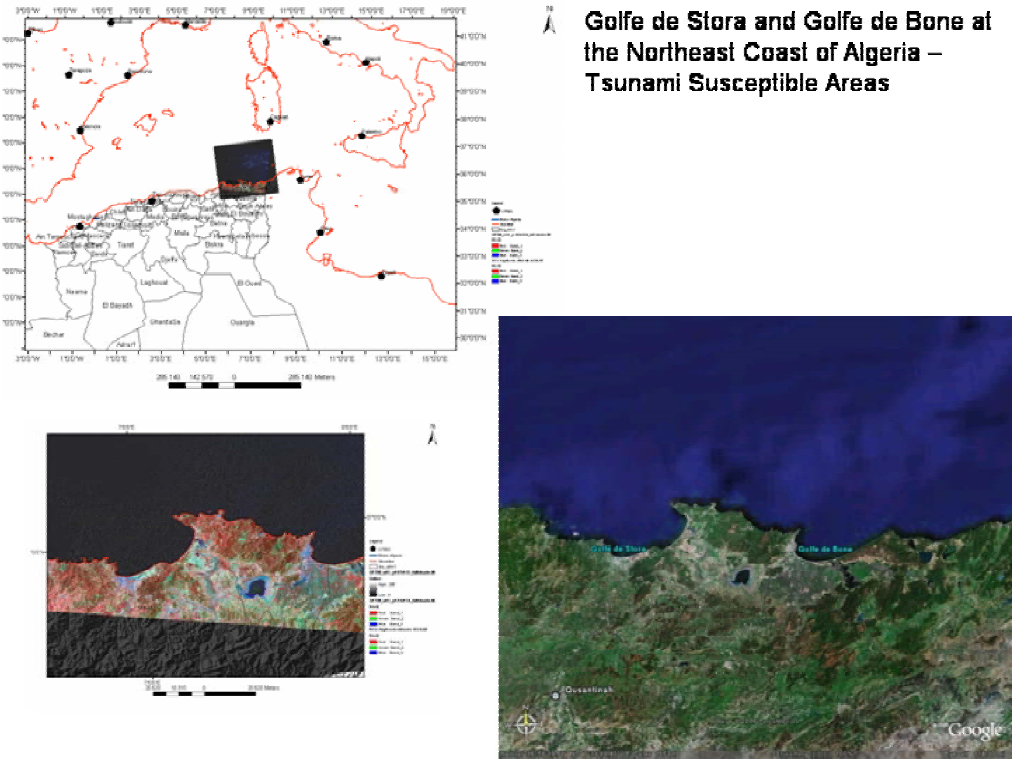

Fig.5: Position of the investigation area

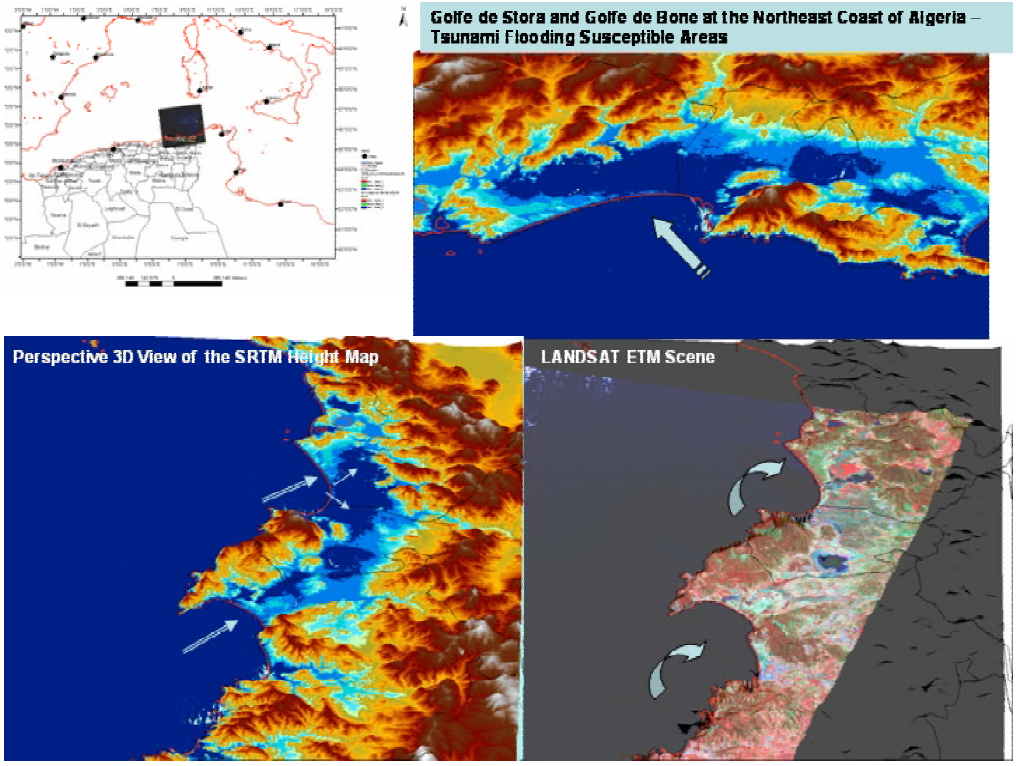

Fig.6: Perspective 3D views of the SRTM based height map and LANDSAT scene

Fig.7 presents a map indicating areas susceptible to flooding in case of a mega-tsunami. A map like this could be of use for land use and emergency planning. In the lowest areas (<10 m above sea level) the potential flooding risk must be considered.

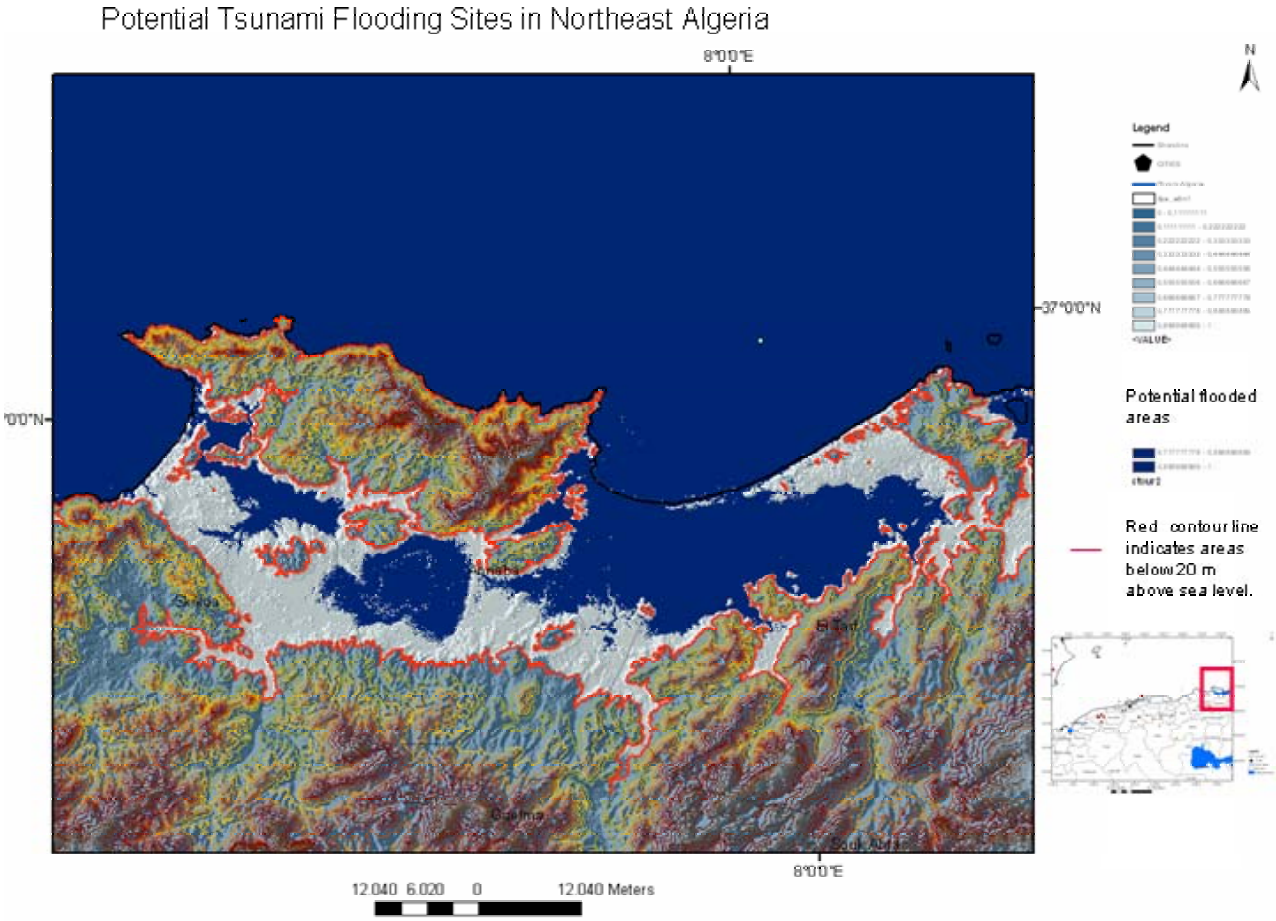

Fig.7: Areas susceptible to flooding in case of a mega-tsunami as indicated by the red contour line and blue colours

Fig.8 shows amplifications of LANDSAT ETM scenes of this area allowing the detection of traces of erosional features that could be explained by abrasion. Linear and parallel traces of erosion, oriented perpendicular to the shore, ending in arc-shaped walls, opened towards the sea, are obviously related to catastrophic flood waves.

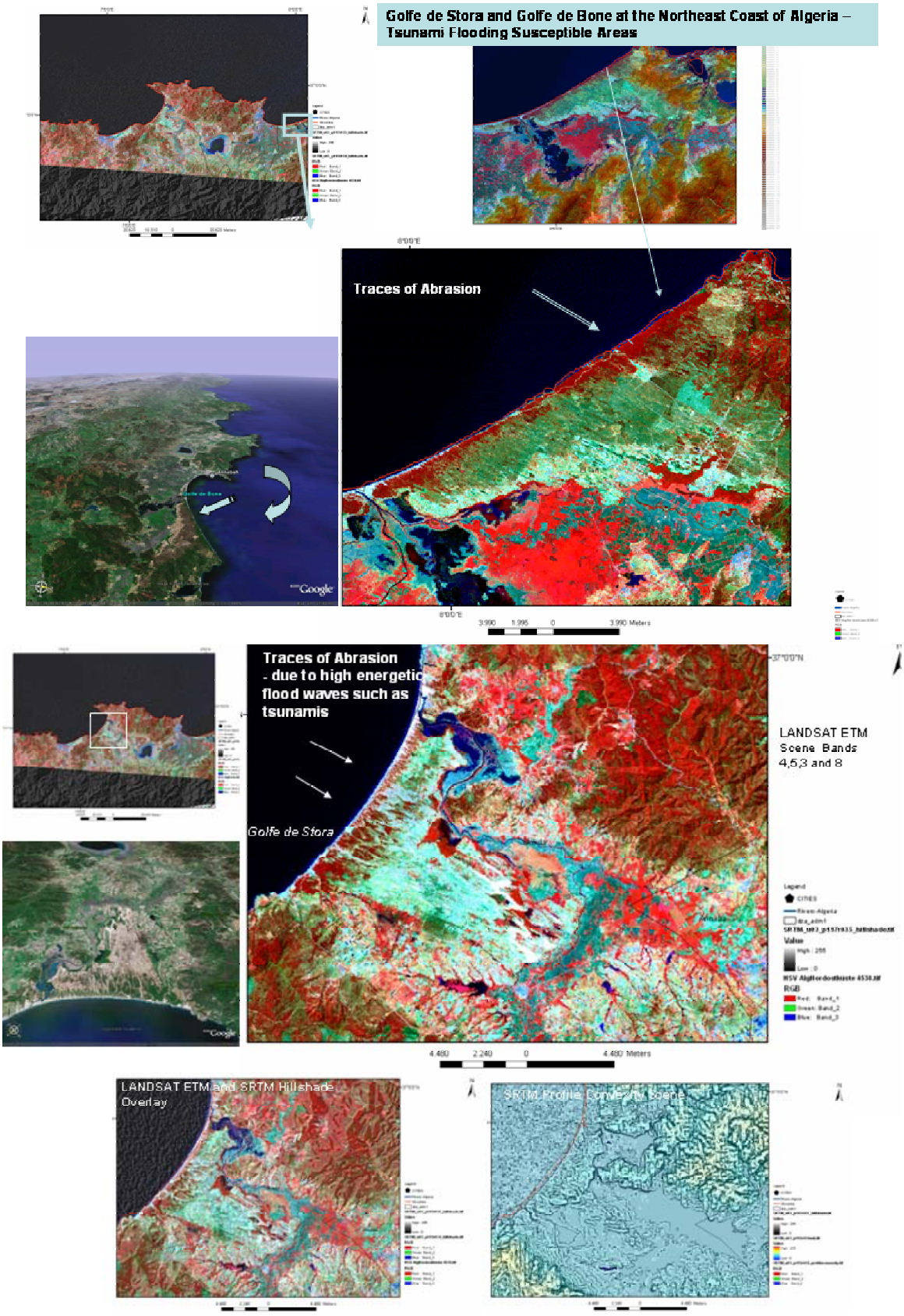

Figs. 8 a and b: Traces of catastrophic flooding visible on LANDSAT ETM scenes and morphometric maps

The next example for the use of remote sensing and GIS methodology for tsunami hazard site detection is shown from the northwest coast (Fig.9). The evaluations of LANDSAT ETM data and SRTM based morphometric maps lead to the conclusion that there is a strong evidence of past, catastrophic tsunami events.

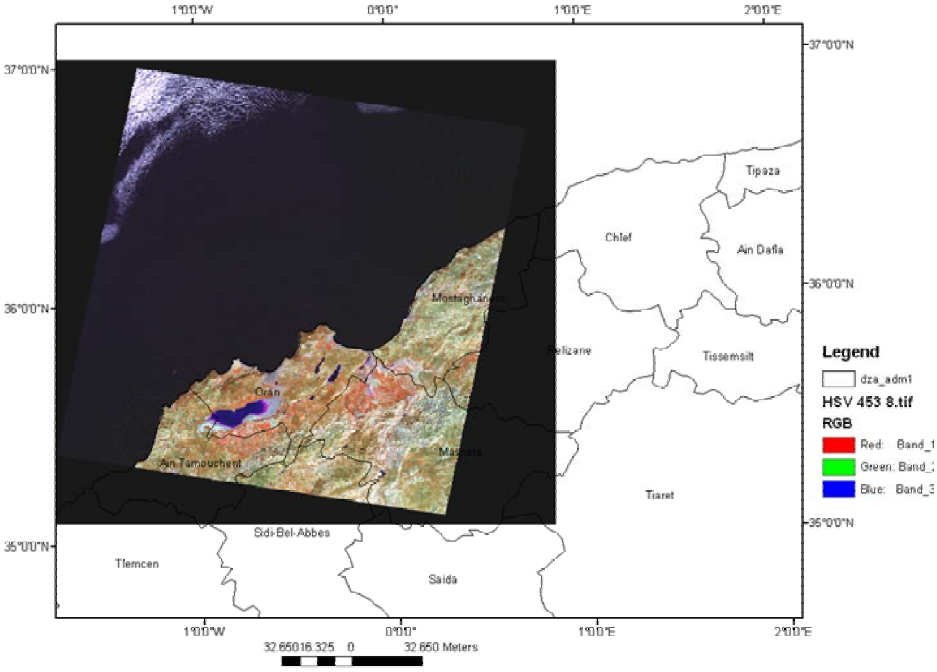

Fig.9: Position of the example in NW Algeria

Fig.10 presents a perspective view of the area.

Fig.10: Perspective View based on Google Earth data

The following Figs.11 a-c show the results of the merge of SRTM morphometric maps and LANDSAT ETM scenes enhancing areas susceptible to flooding.

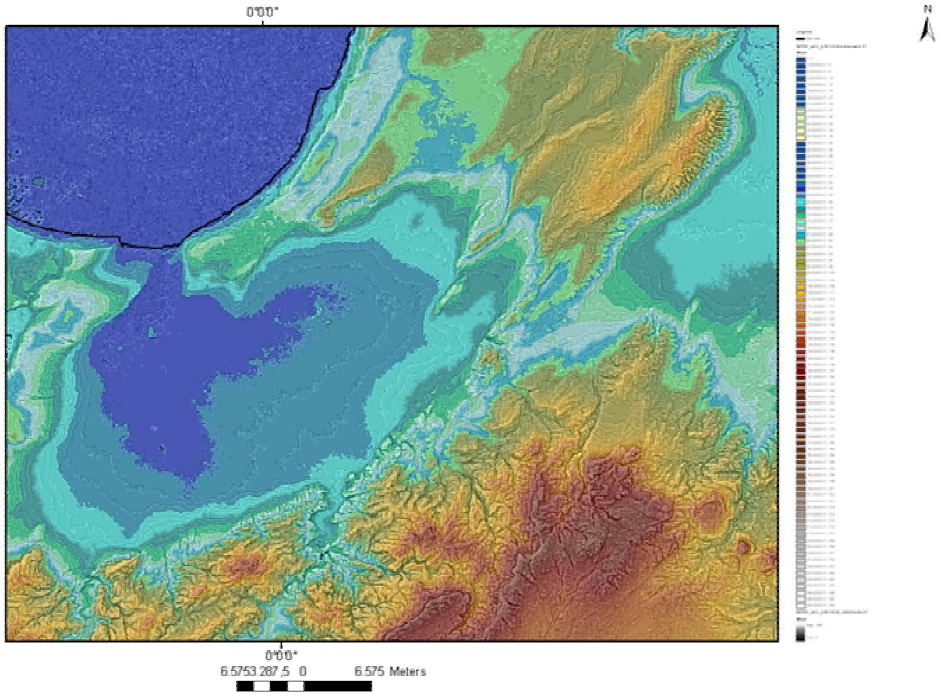

Fig. 11 a: Height map based on SRTM DEM data indicating the lowest areas

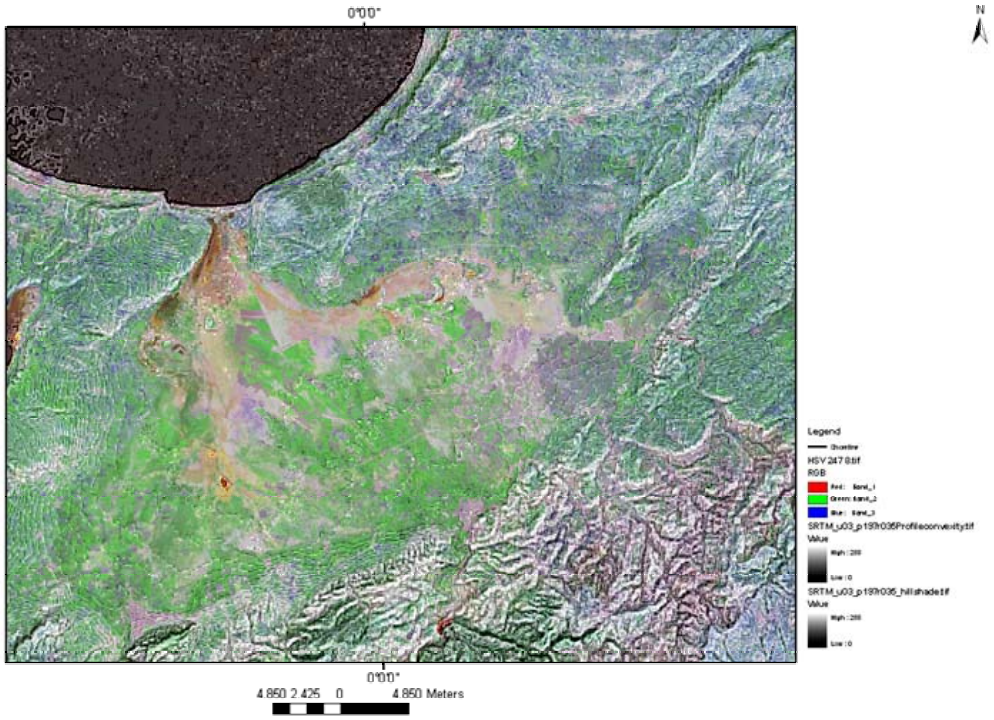

Fig. 11 b: LANDSAT ETM scenes (different band combinations) merged with SRTM Profile Convexity morphometric map

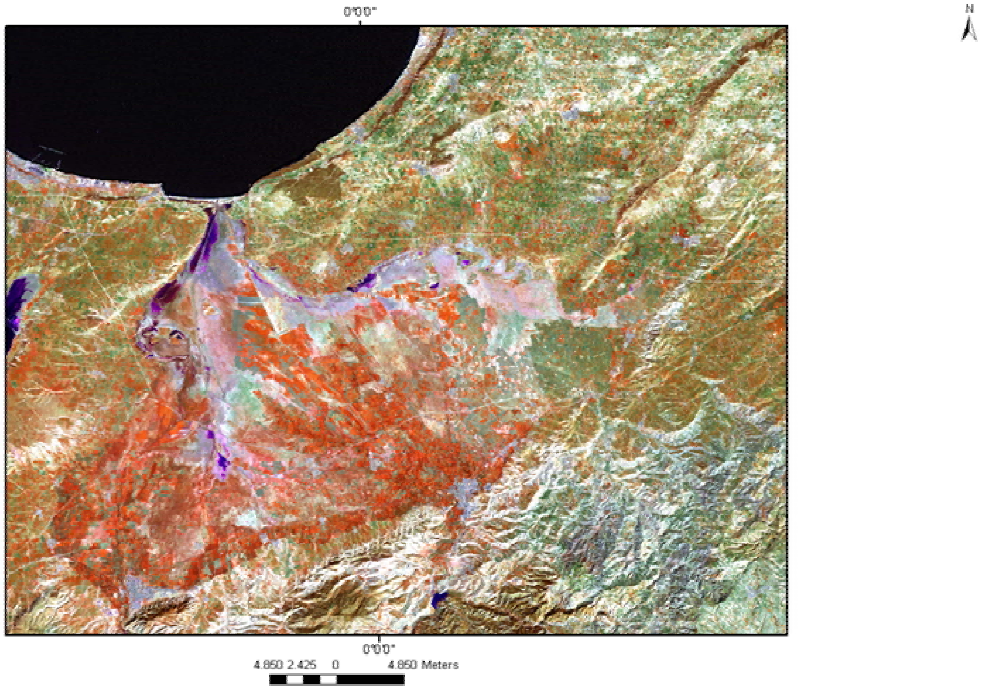

Fig.11 a - c: Overlay of LANDSAT ETM and SRTM data

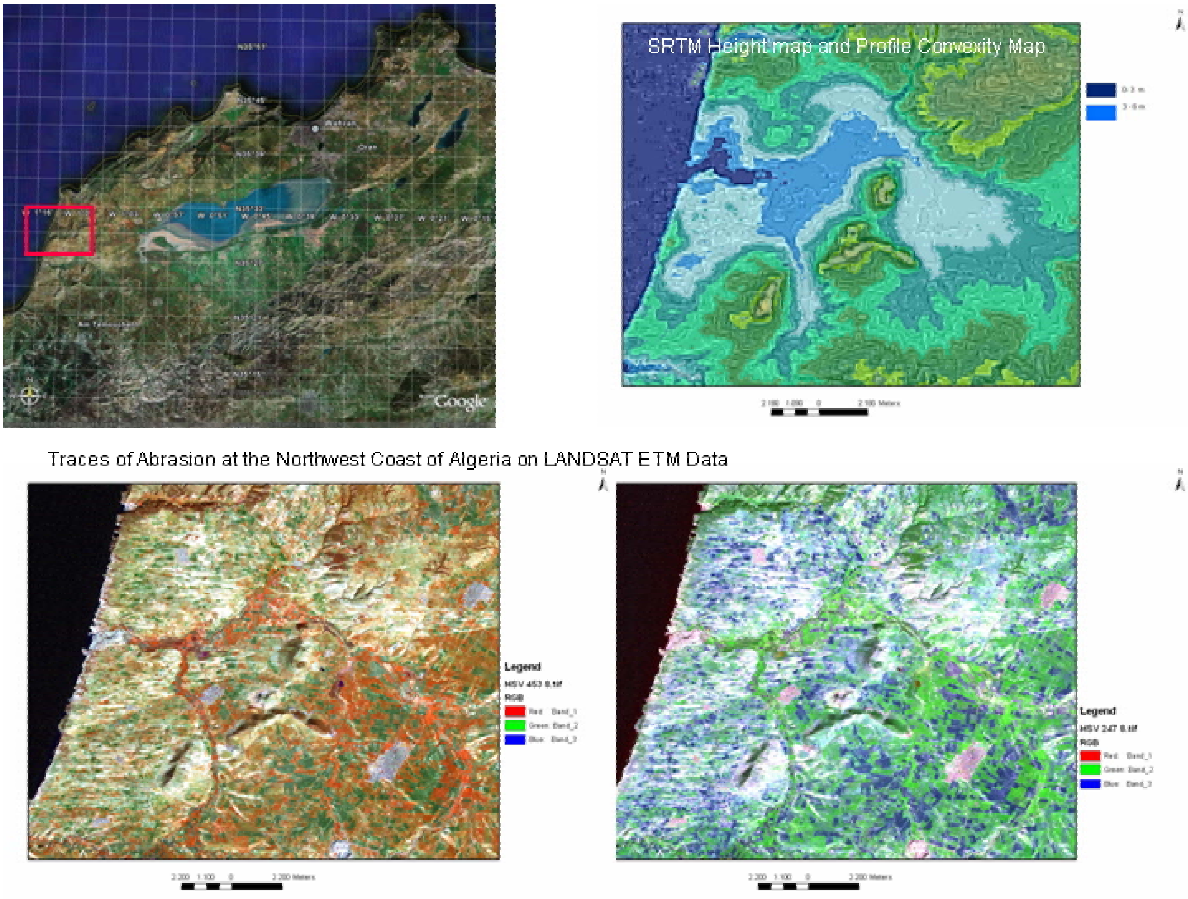

Traces of Abrasion at the Northwest Coast of Algeria on LANDSAT ETM Data

Fig. 12 a: Traces of abrasion visible on LANDSAT ETM imageries

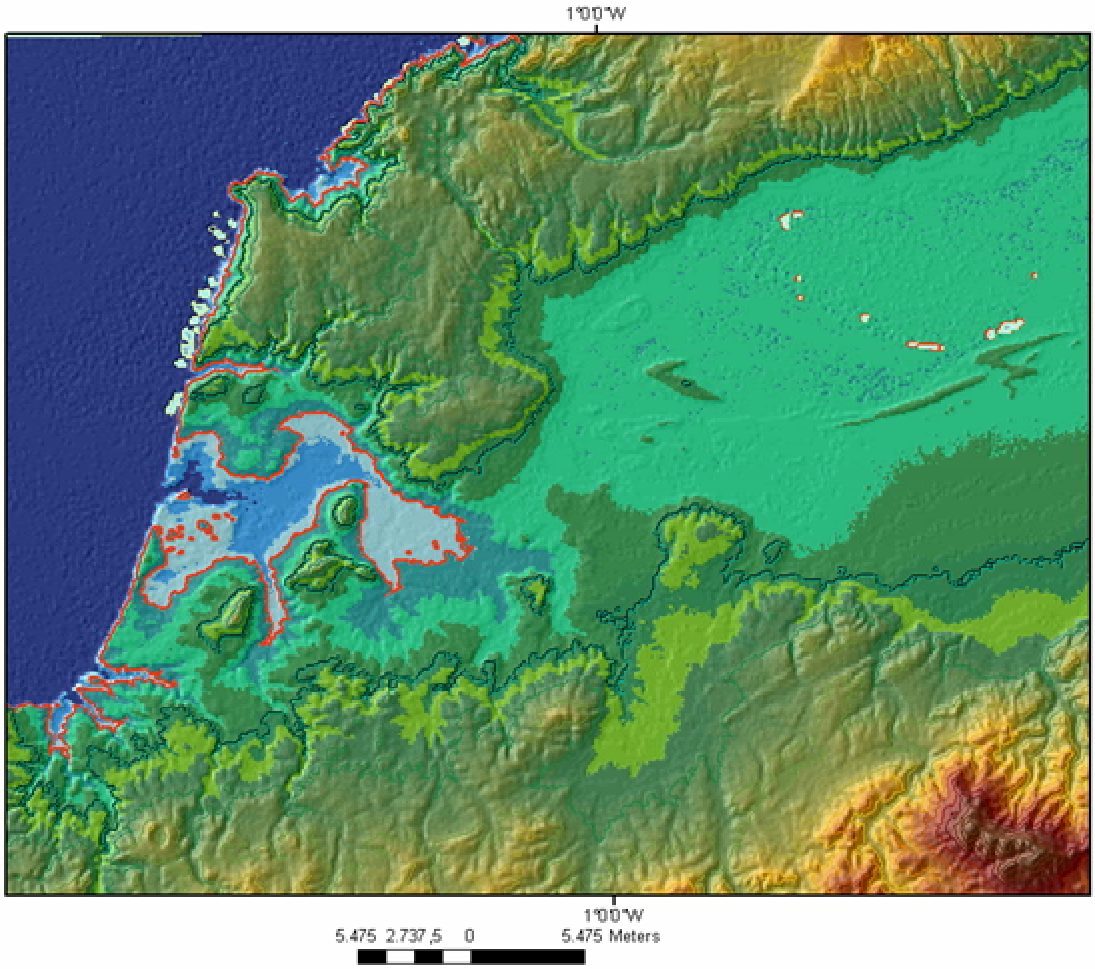

Fig. 12 b: Areas susceptible to flooding as indicated by the red contour line

In the case of catastrophic tsunami events estuary plains and broader riverbeds are very likely prone more to tsunami wave propagation than the environment. River mouths represent a large entrance for tsunami waves.

In Fig.13 such a river mouth is presented from NW Algeria. The morphologic properties of the mouth of the river valley seem as if influenced and formed by flooding.

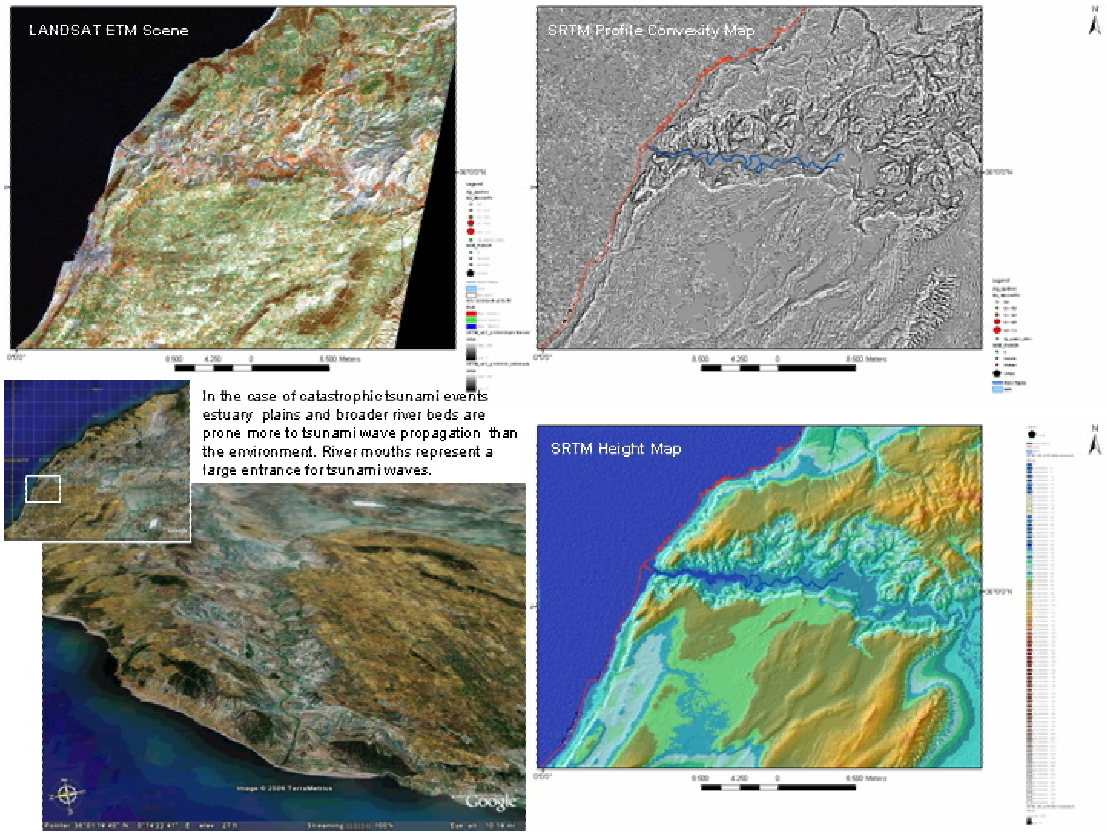

Fig.13: Potential Risk of river mouths

Analyzing the LANDSAT ETM imageries it is obvious that traces of high energy flood waves are not only visible in areas with sedimentary covers. They can be observed in hard rocks as well. Fig.14 demonstrates this.

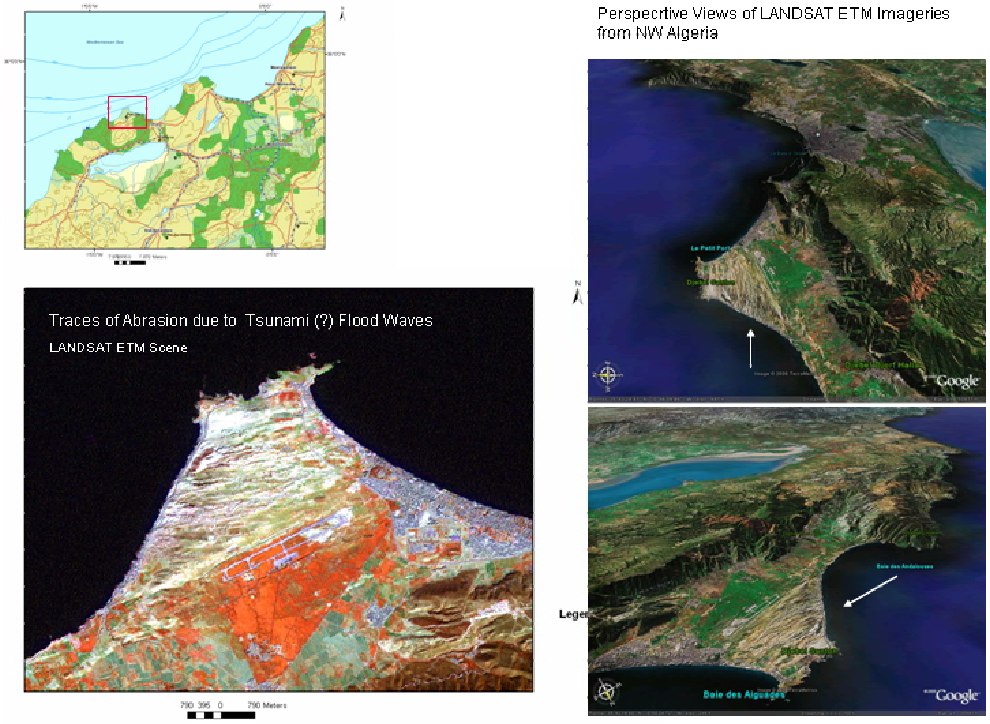

Fig.14: Traces of abrasion and erosion assumed to be related to past tsunami events

The assumed traces of abrasion in the different coastal areas can be used for deriving the main direction of the flood waves creating the run-up. Fig.15 presents the result of the derived wave direction.

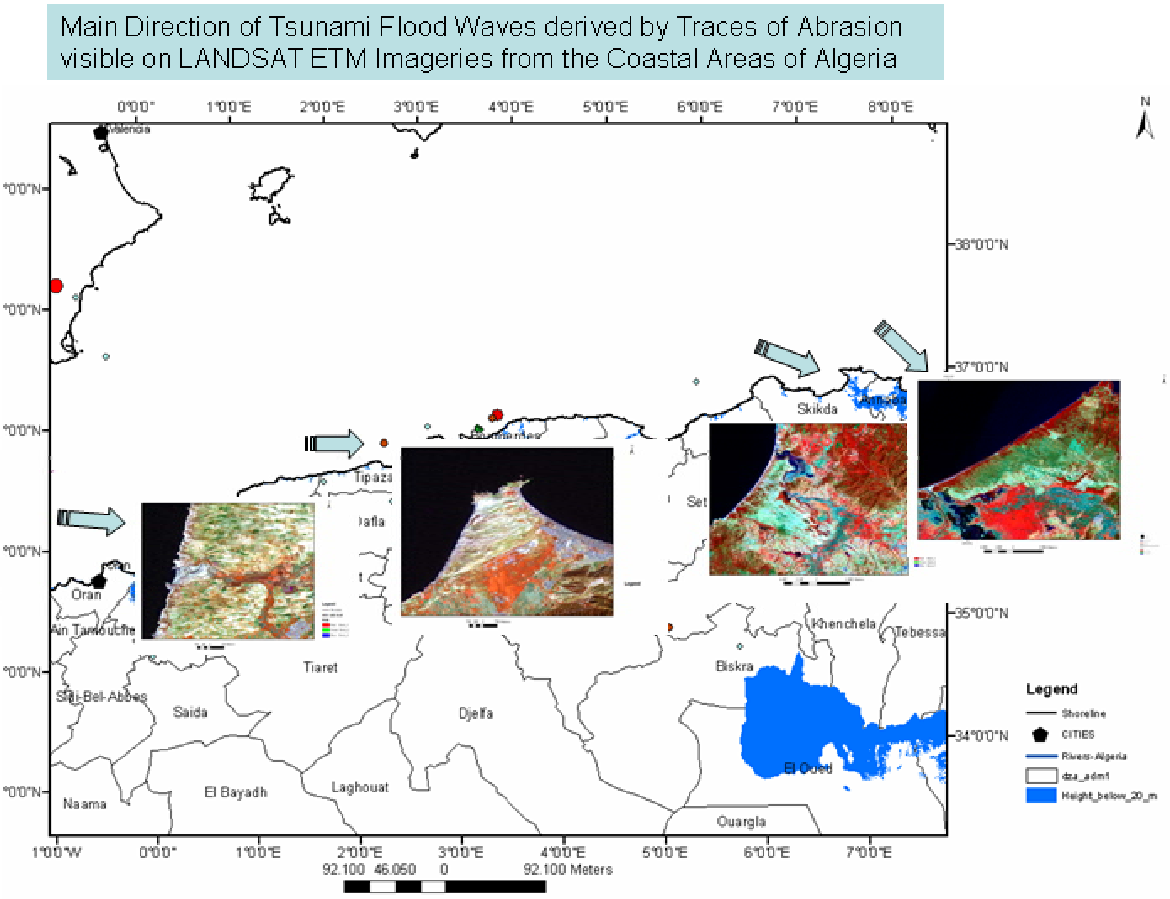

Fig.15: Main direction of flood waves

4. CONCLUSIONS

Evaluations of LANDSAT ETM and SRTM data show clear evidence that catastrophic tsunami events have happened in the past at the coasts of Algeria. This should be considered in the emergency planning and measurements of disaster preparedness.

The design of a common GIS database structure - always open to new data - can greatly contribute to the homogenisation of methodologies and procedures of tsunami risk management.

As one component of such a GIS the following approach is recommended:
- extracting morphometric parameters based on DEM data and
- combining the resulting maps with satellite and other geodata.

Meanwhile, the so-called Free–GIS software fulfilling the basic GIS requirements, as for example DIVA-GIS, Map Window GIS, SAGA GIS, etc., can be used without costs.

Additional Free-GIS software is available also for the spatial analysis of DEM data. Basic LANDSAT ETM and SRTM data are provided free of charge for scientific research purposes for example by the University of Maryland/ USA.

Therefore the use of the remote sensing and GIS technology for tsunami hazard site assessment and for the elaboration of hazard maps according to the presented approach can be

recommended as low cost approach that could be achieved by local communities in Algeria as contribution to a GIS data base.

REFERENCES

Theilen-Willige, B. (2005): Remote Sensing and GIS Contribution to Tsunami Risk Detection. – Vorträge 25. Wissenschaftlich-Technische Jahrestagung der DGPF, 21. – 23. September 2005 in Rostock, GEO-GOVERNMENT - Wirtschaftliche Innovation durch Geodaten, Publikationen der Deutschen Gesellschaft für Photogrammetrie, Fernerkundung und Geoinformation (DGPF) e.V., Band 14, 363-375 Potsdam

Theilen-Willige, B. (2006):Remote Sensing and GIS Contribution to Tsunami Risk Sites Detection in Southern Italy, Zeitschrift PFG der Deutschen Gesellschaft für Photogrammetrie, Fernerkundung und Geoinformation - PFG, Heft 2, 103-114

Theilen-Willige, B. (2006): Tsunami Risk Site Detection in Greece based on Remotes Sensing and GIS Methods. - Science of Tsunami Hazards, Volume 24, No. 1, 35-48, http://www.sthjournal.org/241/willige.pdf

Theilen-Willige, B. and Taymaz, T. (2006): Remote Sensing and GIS Contribution to Tsunami Risk Sites Detection in Turkey, 5th International Symposium "Turkish German Joint Geodetic Days", March 29-31.2006, TU Berlin, Proceedings

Wood, J. (2004): The Geomorphological Characterisation of Digital Elevation Models. - Thesis, http://www.soi.city.ac.uk/~jwo/phd/

Satellite Data:

http://glcfapp.umiacs.umd.edu:8080/esdi/index.jsp

http://worldwind.arc.nasa.gov/download.html

http://earth.google.com/

Shapefiles:

http://map.ngdc.noaa.gov/website/seg/hazards/viewer.htm
http://www.cipotato.org/diva/data/DataServer.asp?AREA=DZA&THEME=_adm

MODELING THE ASIAN TSUNAMI EVOLUTION AND PROPAGATION WITH A NEW GENERATION MECHANISM AND A NON-LINEAR DISPERSIVE WAVE MODEL

Paul C. Rivera
PEERS Coastal Research,
Antipolo City, PHILLIPINES

ABSTRACT

A common approach in modeling the generation and propagation of tsunami is based on the assumption of a kinematic vertical displacement of ocean water that is analogous to the ocean bottom displacement during a submarine earthquake and the use of a non-dispersive long-wave model to simulate its physical transformation as it radiates outward from the source region. In this study, a new generation mechanism and the use of a highly-dispersive wave model to simulate tsunami inception, propagation and transformation are proposed. The new generation model assumes that transient ground motion during the earthquake can accelerate horizontal currents with opposing directions near the fault line whose successive convergence and divergence generate a series of potentially destructive oceanic waves. The new dynamic model incorporates the effects of earthquake moment magnitude, ocean compressibility through the buoyancy frequency, the effects of focal and water depths, and the orientation of ruptured fault line in the tsunami magnitude and directivity.

For tsunami wave simulation, the nonlinear momentum-based wave model includes important wave propagation and transformation mechanisms such as refraction, diffraction, shoaling, partial reflection and transmission, back-scattering, frequency dispersion, and resonant wave-wave interaction. Using this model and a coarse-resolution bathymetry, the new mechanism is tested for the Indian Ocean tsunami of December 26, 2004. A new flooding and drying algorithm that consider waves coming from every direction is also proposed for simulation of inundation of low-lying coastal regions.

It is shown in the present study that with the proposed generation model, the observed features of the Asian tsunami such as the initial drying of areas east of the source region and the initial flooding of western coasts are correctly simulated. The formation of a series of tsunami waves with periods and lengths comparable to observations are also well simulated with the new generation model. Furthermore, the shoaling behavior of the tsunami waves during flooding of dry land was also simulated by the new run-up algorithm. Finally, the new generation and propagation models can explain the combined and independent effects of various factors in tsunami generation and transformation taking into consideration the properties of the ocean and the geologic disturbance.

1.0 INTRODUCTION

Tsunami modeling has always been traditionally undertaken using the shallow water wave equations which are non-frequency dispersive long wave equations. However, recently observed data from the Indian Ocean Tsunami of Dec 26, 2004 using satellite altimetry data that were subject to wavelet analysis by Kulikov (2005) found that the tsunami waves were highly dispersive. It is therefore the aim of this study to develop and implement a dispersive wave model to simulate the propagation and transformation of the tsunami that occurred in the Indian Ocean. In addition, a new generation mechanism that is based on the assumption that currents were induced during the earthquake is also proposed in this study.

The difficulty in correctly simulating tsunamis lies in the fact that they are forced quasi-infra-gravity waves whose characteristic length and period occur in between short gravity wind-waves and long-gravity waves such as tides or storm surges so that they can not be fully described by conventional long wave models. Being a forced wave that depends on the characteristics of the disturbing force, a tsunami wave does not behave exactly as a long wave nor a short wave, but behaves as an intermediate wave that is modified and transformed by the oceanic and seabed properties as it travels away from the generation area.

In testing the present dispersive model and a new generation mechanism, the present study makes use of the coarse-resolution bathymetric information from NOAA-NGDC (ETOPO-5 which was aggregated further to reduce computational time). The study area with bathymetric contours (in meters) is shown in Figure 1.

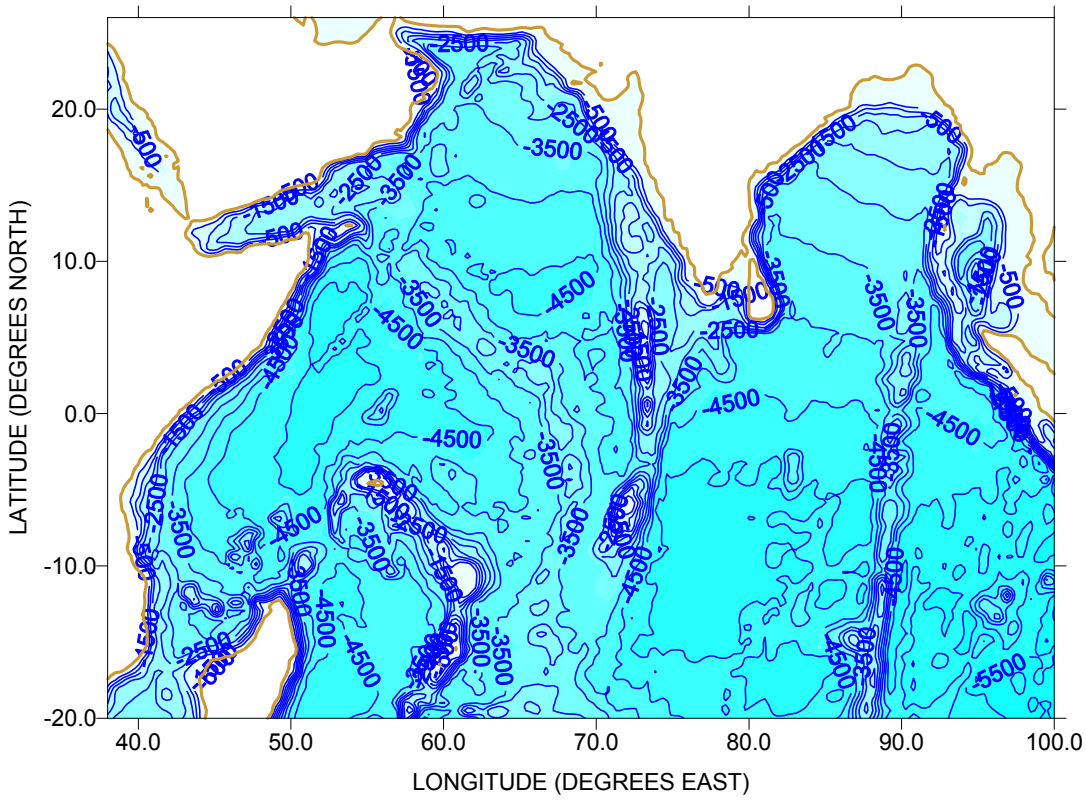

Figure 1. Bathymetric contours (m) within the study area.

2.0 PROPOSED GENERATION MECHANISM

Tsunami occurrence had been documented during submarine earthquakes, volcanic island eruptions, and landslides. Even when an earthquake epicenter is inland or at sea, some tsunami had also been observed. It is therefore appropriate to find a better generation mechanism other

than the conventional approach of determining the ocean surface displacement as a result of seabed motion.

The present generation model can be explained in terms of balance of forces. During a submarine earthquake, an upward force or pressure is exerted in the ocean column by the seabed (Figure 2). Similar to atmospheric pressure effect, this produces a horizontal pressure gradient which should accelerate currents opposite to the direction of the applied pressure gradient force (i.e. $-\rho^{-1}\nabla P_e = a_x$, where ρ is water density, P_e is seabed pressure and a_x is horizontal acceleration). It is postulated that a tsunami may occur if the prevailing downward force or pressure of the ocean column is exceeded by the pressure or force exerted by the seabed. Furthermore, it is also proposed that a seismic-induced pressure gradient force would accelerate currents across the fault. That is, a cross-fault current is generated as shown in Figure 2. The slope of the seabed here may play an important role as it strongly affects the magnitude and direction of the induced currents. In the case of the Asian Tsunami, the increasing water depths towards the west could mean that westerly currents are generated by the quake.

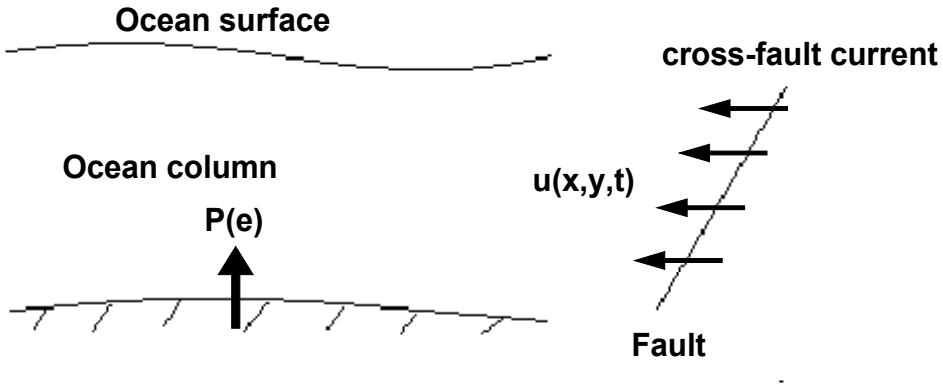

Figure 2. Schematic illustration of the proposed tsunami generation model.

The figure above implies that if the earthquake moment magnitude is high enough, the pressure exerted at the ocean bottom may exceed the pressure exerted by the atmosphere and the water column. This in turn produces an excess pressure whose horizontal gradient (i.e. the pressure gradient force), creates a horizontal acceleration of currents near the fault-line. The impulsive momentum of these horizontal currents and their succeeding convergence and divergence can produce a series of waves that radiates away from the source.

The tsunami generation mechanism that is proposed here may be used to study the waves generated during volcanic eruptions or landslides. During these geologic events, ground accelerations can produce opposing horizontal ocean currents whose successive divergence and convergence can generate potentially destructive tsunami waves. It is assumed that the ocean currents produced by the ground motion oscillates at a frequency that is dependent on the local water depth and the gravitational acceleration. The oceanic currents produced during the submarine earthquake oscillate in time t according to:

$$u(x,y,t) = \kappa\alpha N_z t \frac{\Delta h}{\Delta s}\sin(\omega t) \qquad (1)$$

where $u(x,y,t)$ is the magnitude of the induced horizontal current (m/s), κ is a non-dimensional tuning parameter (= 0.5 in the present study), α is a variable that include factors related to both the seismic disturbance and the ocean column, N_z is the Brunt-Vaisalla frequency (or buoyancy

frequency of the ocean column), $\frac{\Delta h}{\Delta s}$ is the bathymetric slope of the disturbed seabed, and ω is a local current frequency given by $\omega = 2\pi / T_c$. Here, T_c is the period of current oscillation which is given by $\sqrt{h/g}/2$ in which h is the water depth and g is gravitational acceleration. After a long series of numerical experiments and making use of the Buckingham pi-theorem, the dimensional parameter α is found to be;

$$\alpha = \frac{1}{4}\left[\frac{10^{M_w} g}{\rho(D+h)\upsilon}\right]^{1/3} \tag{2}$$

in which M_w is the moment magnitude of the earthquake, ω is the local frequency of current oscillation, D is the focal depth of the earthquake, and v is the kinematic viscosity of seawater. The moment magnitude of the earthquake is an important parameter here as higher M_w values mean higher current accelerations and current velocity generated. The estimated value of α is similar to an induced horizontal motion of water above the disturbed seabed. In Equation 2, the focal depth increases when the earthquake epicenter is not submarine (e.g. when located inland) giving rise to relatively lower value of α as it is inversely proportional to D. In such a case where the epicenter is located inland, the focal depth D becomes $D = \sqrt{D_v^2 + D_h^2}$ where D_v is the actual focal depth directly beneath the epicenter and D_h is the horizontal distance from the epicenter to the ocean water. This case implies relatively lower magnitudes of currents produced by the earthquake and lower tsunami wave heights as well, given all earthquake and ocean parameters constant.

The present model supports the observation that tsunamis can be generated by both submarine and inland shallow-focus earthquakes near deep maritime environments. It is hypothesized however, that when prevailing oceanic currents interfere with the seismic-induced ocean currents in a deep-sea environment where bathymetric slope is large, an abnormally high tsunami can be generated (as supported by the proposed generation model). The Papua New Guinea earthquake of 1998 could be an example of this observation.

The period of current oscillation produced during and after the earthquake is dependent on the square root of the water depth divided by the gravitational acceleration. In the Indian Ocean source region of the December 2004 earthquake, this takes about 10 seconds assuming an ocean depth of about 4000 m. It can be seen from the continuity equation that shallow coastal areas do not favor the generation of strong currents (and consequently high waves) even during strong earthquakes. The difference between the new model from the conventional kinematic model is that the dynamic motion of the ocean column can now be simulated by virtue of the induced currents. When the seabed disturbance sets in, the seawater responds almost immediately as the rupture velocity goes at an enormous speed (= 2 km/s). The proposed tsunami generation model assumes that the ocean currents oscillates in time with a maximum duration equal to the inverse of the buoyancy frequency ($T \sim 2\pi/N_z$). The buoyancy frequency is considered an important hydrodynamic factor in the new generation model. N_z is the frequency of oscillation for a water mass that is displaced vertically upwards during seabed displacement. It is dictated by the vertical stability and compressibility of the ocean column and is given by;

$$N_z = \sqrt{\frac{g^2}{c^2} - \frac{g}{\rho_o}\frac{\partial \rho}{\partial z}} \tag{3}$$

Here, c is the speed of sound in seawater (about 1485 m/s), ρ_o is the reference density (about 1025 kg/m^3). Assuming a -3 kg/m^3 density difference from surface to bottom in a 4 km ocean depth, this gives a buoyancy frequency N_z = 0.00713 s^{-1}. Given all earthquake parameters constant, it can be seen from Equation (1) that the stability of the water column can increase the current acceleration or velocity (and consequently, the wave heights) if the vertical stratification of the water column is stable with negative vertical density gradient giving N_z a higher magnitude. The effect of wave amplification due to ocean compressibility has been suggested by Hunt (1993).

A time-series plot of the induced horizontal currents within the source area is shown in Figure 3. In general, spatially non-uniform current (and wave) patterns would develop due to non-uniformity of ocean bottom and the pressure gradient forces acting in the water column. The spatial variation of current in the present formula is assumed to depend only on the variation of depth within the source region. Due to bathymetric changes, divergence and convergence of currents may also occur giving a turbulent and complex current velocity field in the source region. It is hypothesized that these currents should continue to oscillate even after cessation of the fault line rupture until dissipated by friction.

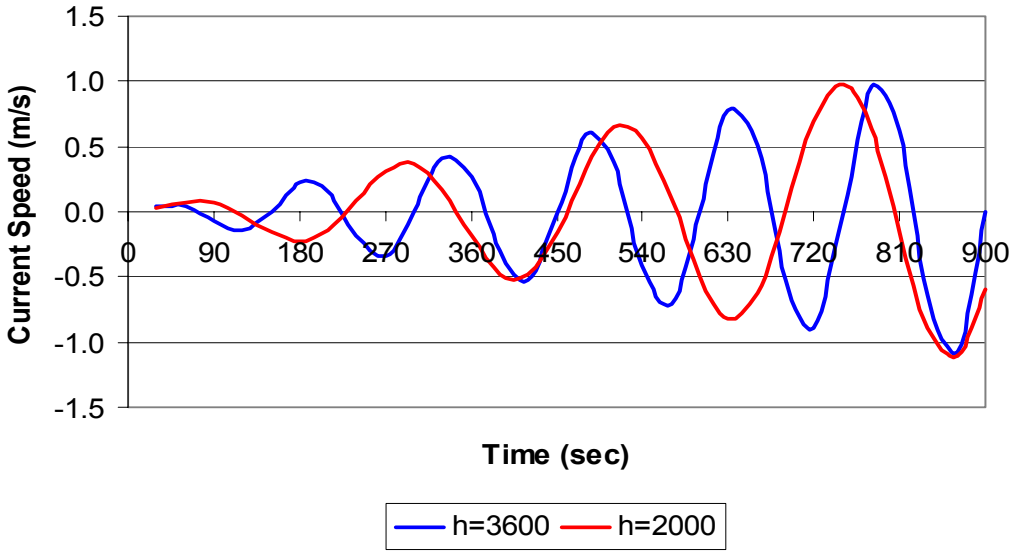

Figure 3. Current oscillations generated in a water depth of 3.6 km and 2 km during a submarine earthquake. The induced ocean currents can produce a series of potentially destructive tsunami waves.

Depending on the magnitudes of the currents generated and the overall physical oceanographic characteristics of the source region and its vicinity, these currents can become transoceanic and can generate a series of destructive waves that can travel long distances away from the source region. The horizontal currents produced by the seismic disturbance should be spatially non-uniform and not constant at the opposite sides of the ruptured fault since the water depth and the seabed pressure vary horizontally. The proposed formula gives an estimate of the spatial and temporal variation of the ocean currents within the source region. Assuming an earthquake moment magnitude M_w = 9.1, the maximum current magnitude estimated by the present model was about 2 m/s. It is assumed that after the time period T, the induced-current will continue to oscillate but decreases in time opposite to the increasing current shown in Figure 3.

It is further hypothesized that the vertical profile of the induced current increases downwards in contrast to normal wind-driven and tide-generated currents which are almost logarithmically increasing upwards. This is because the generating force comes from below

the ocean column opposite to the atmospheric (and hydrostatic) pressure gradient force. The recently observed 'dead zone' along the tsunami source region west of Sumatra is most likely caused by the induced strong oceanic currents near the seabed and not directly by the oceanic waves. This is because the water is just too deep in the area for even an abnormally high offshore tsunami to impart a considerable wave action at the seabed.

3.0 TSUNAMI MODELING WITH A NON-LINEAR DISPERSIVE LONG WAVE MODEL

As altimeter data from satellites showed that the Indian Ocean tsunami was highly dispersive, it is therefore appropriate to use a dispersive long-wave model. This study differs from previous modeling studies conducted by various authors in that a dispersive wave model was used in the open ocean instead of the conventional non-dispersive long-wave model.

Assuming that water density does not change with time, the partial differential equation describing the time-dependent variation of the surface wave heights in the ocean area of interest is given by the modified mass continuity equation:

$$p\frac{\partial \zeta}{\partial t} + \frac{\partial\left[u\ \left(h + \zeta\right)\right]}{\partial x} + \frac{\partial\left[u\ \left(h + \zeta\right)\right]}{\partial y} = 0 \tag{4}$$

where p is the porosity, ζ is the wave height, t is time, and x and y are coordinate axes in the Cartesian system, u and v are the mean components of the wave-induced flow in the x and y-axes respectively, τ_s is the wind stress acting over the sea surface, ρ is the sea water density, h is the total water depth, and h_o is the still water level. Similar to the dispersive wave model of Madsen and Sorensen (1992), the porosity factor p is included for the simulation of partial wave reflection and transmission. This time-dependent equation allows for the determination of the temporal as well as spatial variation and evolution of the wave height due to the divergence (and convergence) of the horizontal currents produced by an applied disturbance of various origins (e.g. seismic, atmospheric, landslides etc).

The difficulty in modeling tsunami can be due to the fact that they are intermediate, quasi-infra-gravity waves, having the combined characteristics of long and short ocean waves. As initiated by previous authors (e.g. Koutitas and Laskaratos 1988, Pedersen *et al*. 2005), the initial idea in the present study was to seek a combination between a dispersive and non-dispersive model. The non-dispersive model may be applied in the open ocean while the dispersive model could be applied in shallow coastal areas to determine the transformation of the waves as they travel from deep to shallow waters. Incidentally, the non-linear dispersive momentum equations originally proposed by Peregrine (1967) and Wu (1981) for the study of long waves in oceans and beaches were modified and applied in this study. In combination with a simple periodic current induced by a seismic disturbance, the simple dispersive model worked. Various combinations of momentum terms such as those proposed by Madsen and Sorensen (1992) were tried. Eventually, the momentum equations were simplified due to negligible effect of some higher-order terms. The effect of ocean baroclinicity and compressibility is included by using a modified pressure gradient force. The modified momentum conservation equations for dispersive long gravity waves take the non-linear form:

$$\begin{aligned} &p\frac{\partial u}{\partial t} + u\frac{\partial u}{\partial x} + v\frac{\partial u}{\partial y} = pfv - p^2 g\frac{\partial \zeta}{\partial x} - p^2 N_z^2\frac{\partial\left(\zeta h\right)}{\partial x} + \frac{\tau^{sx}}{\rho h} - k\frac{u\sqrt{u^2+v^2}}{h} + p\upsilon_h\left(\frac{\partial^2 u}{\partial x^2} + \frac{\partial^2 u}{\partial y^2}\right) \\ &+ p\frac{h_o^2}{3}\left(\frac{\partial^3 u}{\partial x^2 \partial t} + \frac{\partial^3 v}{\partial x \partial y \partial t}\right) + p\frac{h_o}{2}\frac{\partial^2 h_o}{\partial x^2}\frac{\partial u}{\partial t} + ph_o\frac{\partial h_o}{\partial x}\left[\frac{\partial^2 u}{\partial x \partial t} + \frac{\partial^2 v}{\partial y \partial t}\right] + ph_o\frac{\partial h_o}{\partial y}\left(\frac{\partial^2 v}{\partial x \partial t}\right) \end{aligned} \tag{5}$$

$$p\frac{\partial v}{\partial t}+u\frac{\partial v}{\partial x}+v\frac{\partial v}{\partial y}=-pfu-p^2g\frac{\partial \zeta}{\partial y}-p^2N_z^2\frac{\partial(\zeta h)}{\partial y}+\frac{\tau^{sy}}{\rho h}-k\frac{v\sqrt{u^2+v^2}}{h}+\upsilon_h\left(\frac{\partial^2 v}{\partial x^2}+\frac{\partial^2 v}{\partial y^2}\right)$$
$$+p\frac{h_o^2}{3}\left(\frac{\partial^3 v}{\partial y^2\partial t}+\frac{\partial^3 u}{\partial x\partial y\partial t}\right)+p\frac{h_o}{2}\frac{\partial^2 h_o}{\partial y^2}\frac{\partial v}{\partial t}+ph_o\frac{\partial h_o}{\partial y}\left[\frac{\partial^2 v}{\partial y\partial t}+\frac{\partial^2 u}{\partial x\partial t}\right]+ph_o\frac{\partial h_o}{\partial x}\left(\frac{\partial^2 u}{\partial y\partial t}\right) \quad (6)$$

where u and v are the depth-averaged wave-induced flow components in the x and y-axes respectively, p is a porosity factor that allows for partial reflection and transmission of waves, f is the latitude-dependent Coriolis parameter, g is the gravitational acceleration, N_z is the buoyancy (or Brunt-Vaisalla) frequency, k is a frictional resistance coefficient, and υ_h is the horizontal eddy viscosity coefficient. The total water depth h is the sum of the still water depth h_o and the surface wave height ζ. As these equations represent a balance of forces in the ocean, they are useful in dealing with non-linear dispersive long and intermediate waves in both deep and shallow coastal waters. In the present study, these dispersive wave equations are applied in both deep oceanic waters and shallow coastal waters. With the addition of dynamic pressure, wind effect, and horizontal viscosity, they represent the modified two-dimensional dispersive long-wave equations in oceans and coastal waters. The eight terms to the right of the momentum equations are considered important as they describe the diffusive effect of sloping ocean bottom. They also allow lower frictional effect where high friction often obliterates the real numerical solution by unnecessary damping of the resulting current velocity field. The last two terms are deep water terms and their effects are also small but considered here to represent the propagation of the tsunami waves from deep to shallow waters. Villenueve and Savage (1993) derived a more sophisticated momentum equation taking into consideration the bed motion. The present model assumes that the sea bed is stationary and it is the ocean column that moves in a dynamic fashion during and after the seismic disturbance.

The wind stress effect can be necessary to include the contribution of the wind energy in the horizontal momentum dispersion and hence in the long-distance propagation of the tsunami waves. The presence of the wind can be seen in an increased horizontal currents and the interaction between the wind-driven currents and the waves may be important during a tsunami occurrence. The wind stress terms can be estimated from quadratic stress formulas.

It can be seen that the pressure terms in the momentum equations consist of the sum of the hydrostatic and dynamic pressures due to a barotropic and a baroclinic ocean. This is considered important in geophysical flows with a considerable influence of vertical stability and vertical acceleration as could be the case during a tsunami.

The present wave model considers the effect of the tide by assuming that the water level periodically increase and decrease during high and low tide episodes. In coastal seas, the tide modifies the initial depth distribution and it could be a substantial fraction of the water depth in shallow areas. Waves propagating in shallow near-shore regions are thus affected by the temporal variation of the water depth introduced by the tide. The tidal current can therefore have a substantial effect on the tsunami wave propagation.

The non-dimensional bottom frictional resistance k is normally taken as constant with values ranging from 0.001-0.01. The lower limit was used in the present modeling study. The use of a Chezy or Manning formula for the bottom friction coefficient is also possible but the use of a constant coefficient is recommended in the present study as the wave run-up appears to be slightly attenuated with the former formulas.

The horizontal eddy viscosity is also included in this study and is parameterized using the Smagorinsky turbulence scale approach and the use of a constant eddy viscosity has been avoided. Here, horizontal viscosity is dependent on the gradient of the horizontal velocity components as in:

$$\nu_h = \upsilon A\left[\left(\frac{\partial u}{\partial x}\right)^2 + \left(\frac{\partial v}{\partial y}\right)^2 + \frac{1}{2}\left(\frac{\partial u}{\partial x}+\frac{\partial v}{\partial y}\right)^2\right]^{1/2} \tag{7}$$

where υ is constant (0.01-0.5) and A is the area of a grid element. The present model uses a value of 0.05.

The effect of the earth's rotation (e.g. Coriolis force) on the waves is also considered in the present study by including it in the momentum equations. In higher latitudes, the Coriolis force may have a significant effect especially when horizontal currents are strong and may therefore affect the tsunami waves as they travel away from the source region.

3.1 NUMERICAL SOLUTION AND MODEL IMPLEMENTATION

As the high-order dispersive terms in the momentum equations require a lot of transformation and complexity in the numerical solution, a rectangular coordinate system with square grid cells was used to simplify the solution of the coupled partial differential equations. The effect of the deep water terms (e.g. last 2 terms to the right of the momentum equations) may be negligible in deep ocean calculations but could be important in shallow waters. Therefore, it is recommended to retain the same number of terms in the momentum equations as they represent a balance of forces which should be applicable in both deep and shallow water domains.

For the simulation of the wave and tide processes, a Fourier series describing the tide variation in the computational area of interest has been implemented. The tide contributes much to the total water level especially in shallow areas. The contribution of the tide in the tsunami run-up can be very significant especially during high tidal phase. To include the tidal effect to the water depth, the Fourier series below was used.

$$\zeta_t = a_o + \sum_{i=1}^{n} a_i \cos(\omega_i t - \phi_i) \tag{8}$$

where a_o is the mean amplitude of the tide level, a_i is the amplitude, ω_i *is* the frequency and Φ_i is the phase of the i^{th} tidal constituent. This tidal height ζ_t, is just added in the present study to the total water depth h during the period of simulation. The four major tidal constituents namely O_1, K_1, M_2 and S_2 tides are included in the second term in the right-hand side of this equation.

The numerical solution of the dispersive wave equations is based on an explicit finite difference scheme with the unknown variables staggered in space using the Arakawa C-Grid. The variables are solved with the wave height and water depth at the center of a grid cell. The depth-averaged current component in the x-axis is located at the center of a y-directed side (left and right of the grid mesh) and the current component in the y-axis is located at the center of an x-directed side. To simplify the finite differentiation of the momentum and continuity equations, the grid distance was assumed equal in the x and y-directions ($\Delta x = \Delta y = 30\ min$). In this space-staggered grid, the first order space derivatives are solved using high-order finite differences as in Kowalik (2003) given by

$$\frac{\partial \eta}{\partial x} = \left(\eta_{i-2} - 27\eta_{i-1} + 27\eta_i - \eta_{i+1}\right)/24\Delta x \qquad (9)$$

where η is the unknown variable (e.g. currents or waves).

The numerical integration proceeds from the calculation of the continuity equation and the specification of the open boundary condition. Here, the first-order spatial derivatives are solved using Equation 9. Using the newly computed wave height, the momentum equations are solved. Here, the *u*-component of the flow is solved throughout the computational domain using a second order upstream numerical scheme for the advective terms as proposed by Stelling (1984) and Kowalik (2003). The calculation of the earthquake-induced currents from Equation 1 is done after the *u*-component of currents is computed. After this, the calculation of the *v*-component of the current using the same second order upstream scheme for the advective terms follows. The pressure gradient terms (i.e. sum of barotropic and baroclinic pressures) and the horizontal bathymetric gradient of the deep-water terms in the momentum equations are also solved using high-order finite differences as in Equation 9. Filtering of computed velocity fields as in Kowalik (2003) was also carried out with a smoothing coefficient of 0.005. For boundary conditions, only wave height is prescribed. Here, wave heights in all the open ocean boundaries of the computational domain were treated with a pseudo-implicit form of the Orlanski Radiation condition described in literature (Rivera 1997). No special control mechanism is implemented near land and water boundaries as the proposed flooding and drying algorithm (described below) automatically computes waves and currents as long as there is water in grid cells of interest.

3.2 FLOODING ALGORITHM AND RUN-UP MODEL

The flooding and drying of low-lying areas is considered a difficult modeling problem. Together with the tsunami propagation from offshore to near-shore areas, inundation of dry land makes tsunami modeling an exceedingly difficult hydrodynamic problem (Beikae 2001). The succeeding run-down and periodic exposure of low-lying areas is less complicated to model numerically.

To handle the run-up and run-down problem, a simple computational algorithm of flooding and drying was developed and implemented in this study. Whenever the water depth is positive (i.e. greater than zero), the continuity and momentum equations area solved. The inclusion of the eight terms to the right of the momentum equations is shown to be very important in the numerical solution of the model equations. In the solution of the non-dispersive long-wave equations, the bottom frictional terms may lead to overflow of numerical solutions if the water depth is too low. However, with the inclusion of this slope-term, there is no associated over-flow problem in the momentum equations as long as the water depth is greater than zero. After successively computing for the wave heights and current components, the new water depth is updated (i.e. $h = h_o + \zeta$). Initially, grid cells which are dry (e.g. land areas) have negative values determined by the height of the land above sea level. On the other hand, wet areas (e.g. ocean areas) have positive depths. For all grid points with non-zero wave height and positive depth, a counting index equal to 1.0 is assigned. On the other hand, all dry points (e.g. grid cells without water) are assigned a counting index of 0. During wave run-up onto dry land, the water depth is calculated using $h = h_o + \zeta_{bar}$ where ζ_{bar} is the sum of all surrounding non-zero wave heights divided by the sum of the counting indices. Here, when all surrounding grid cells have non-zero wave heights (i.e. all wet), ζ_{bar} is the average of 8 (and not 4) surrounding values. Otherwise, it will use less than 8 points depending on the number of wet grid points around the grid point of interest. As the inundating wave may come from any direction (such as from the back of an island during wave refraction or wrap-up and reflection near-shore), the new flooding scheme should be applicable as it considers the 8-surrounding grid-points. The total water depth in a flood-prone cell depends on the total number of

surrounding cells with non-zero wave heights. When the new depth is positive, it will be considered in the next series of computations of the continuity equation. For the momentum equations, calculation of the *u*-component will proceed if $h_{i,j}$ and $h_{i+1,j}$ are greater than zero (e.g. both adjacent grid points along *x*-direction are wet). In the same manner, calculation of the *v*-component will proceed if $h_{i,j}$ and $h_{i,\,j+1}$ are greater than zero (e.g. both adjacent grid points along *y*-direction are wet).

If the next grid cell is still dry during inundation (i.e. *h* is still negative), it will assume that new negative value and will not be considered in the next series of computation until it becomes wet or positive. However, it should be noted here that in these areas where the water flow is impeded by high grounds, the wave height can grow tremendously due to the associated strong spatial gradient in the horizontal currents during a tsunami approach to the shore. This shoaling behavior of the wave is reproduced by the present run-up algorithm by using a fine resolution small-scale model with a grid-distance of 150 m. The new flooding and run-up algorithm therefore requires accurate information about the topographic and bathymetric characteristics of flood-prone areas. Where inundation is expected to be far inland, the model grid should encompass all vulnerable low-lying areas with a very high resolution in space. With the present algorithm, the whole water-land area is part of the computational domain and does not require a moving boundary condition. Setting of a zero-normal velocity at high grounds is set automatically only from knowledge of the total water depth.

4.0 RESULTS AND DISCUSSION

In its numerical implementation, Equation 1 is applied from longitude 91.5 º E – 93 º E and latitude 2 º N -11 º N approximating water motion within the source region throughout the assumed period of oscillation *T* (14.68 min). It should be noted that in the present modeling study, a north-south orientation of the affected oceanic column was chosen to simplify the source specification. A curved source region similar in orientation to the ruptured fault can be assumed in future studies. After the quake, the currents are assumed to increase periodically. After the time duration *T*, the already accelerated currents from the source area and the resulting turbulent sea surface continue to oscillate and extend spatially until dissipated by gravity, turbulent energy, and friction. Nosov and Skachko (2001) initially suggested that current oscillation during ground motion is an important non-linear mechanism for tsunami generation.

In a series of numerical tests with the dispersive wave model, a 'numerical gravity' error is observed. This kind of damping error had been documented in a series of numerical tests by Abbott *et al.* (1984). This was corrected in the present modeling work by applying a gravity correction term to the *x* and *y*-momentum equations respectively in the form;

$$F g \frac{\Delta t}{8}\left(\frac{\partial^2 uh}{\partial x}\right);\; F g \frac{\Delta t}{8}\left(\frac{\partial^2 vh}{\partial y}\right) \tag{10}$$

The value of *F* may range from 1-20 for the present space and time-discretization. This was adjusted to a value (= 10.0 in the present study) until the gravity error was removed. This error is seen as a progressive damping of wave height after several hours or days of numerical integration.

The bathymetric slope $\frac{\Delta h}{\Delta s}$ was assumed to be the absolute value of the difference between the water depths at 93 º E minus the water depths at 91.5 º E divided by $3\,\Delta s$, where Δs is the model grid distance. As depth changes horizontally, the slope changes along the source latitude, e.g. 2-11ºN. The source parameters for the present tsunami model are summarized in

Table 1. The time interval for numerical integration was 30 seconds to maintain numerical stability with the explicit solution. The porosity factor p was initially assigned a value of 1.0. The wind speed factor was assigned a very weak uniform magnitude of 1 m/s (from 80º). Numerical integration was done up to 48 hours only. With the 122 x 92 grid points of the present computational domain (38º-100ºE, 20ºS-25.5ºN), this took about 2 minutes run time in a Pentium 4 (2.8 GHz) computer.

Parameter	Description	Value
M_w	Moment Magnitude	9.1 (7.1 after 3 hours)
D	Focal Depth	10 km
ρ	Water Density	1025 kg/m^3
Δs	Distance in the slope term (width of disturbed area)	165 km
ν	Kinematic viscosity of seawater	0.0000122 m^2/s
N_z	Buoyancy (Brunt-Vaisalla) Frequency	0.00713 /s
κ	Tuning parameter	0.5 -

Table 1. Source parameters for the proposed tsunami generation model.

The results of the present modeling work are shown in a series of maps in Figures 4-8. Comparison of observed wave heights with the satellite altimeter data is shown in the time series graph of Figure 9. It can be seen in Figure 4 that the proposed generation model would produce a complex wave pattern of positive and negative values in the source region located near the ruptured fault line. The disturbed ocean water may not lie exactly above the ruptured fault. The assumption of a straight fault still showed a complex wave pattern due to the induced current oscillations from varying depths within the area. The computed wave heights after 1 hour showed a combination of positive and negative waves radiating away from the source region (Figure 5). Two hours after the quake, a distinct positive wave front shown by the red contours (flooding) has reached the eastern Sri Lankan coast (Figure 6). On the other hand, negative waves (drying) shown by the blue contours are predominant east of the source region. The formation of a series of waves can also be seen. Three hours later, the tsunami waves are shown by the model to suffer from refraction and diffraction in southern India (Figure 7). This is more pronounced 4 hours later as shown in Figure 8. The western side of Southern India is shown to be affected by the diffracted waves.

A comparison between observed and simulated tsunami wave height is shown in Figure 9. Due to the absence of numerical data, the altimeter data from the Satellite Jason-1 is shown along with the earlier computations of Pedersen et al. (2005). It is shown in the figure that a relatively good agreement between observed and modeled wave height occurs between 10ºS-10ºN. Using the proposed non-linear dispersive long wave model and the new generation mechanism, an improvement in model simulation can be seen between the Equator to about 5 ºN. The slight difference between observed and calculated wave heights after 10ºN could be the result of a combination of factors, both numerical and physical, such as the actual location of disturbed oceanic region, numerical dispersion due to large grid distance used, and early shoaling of the tsunami wave due to low spatial resolution. However, as the main energy lobe of the tsunami is concentrated at about 10ºS-10ºN, it is therefore important to have an accurate numerical simulation within this region which was demonstrated by the present model. Accurate model prediction especially with regards to wave amplitudes and phases can imply an improved warning system in terms of tsunami magnitude and arrival time.

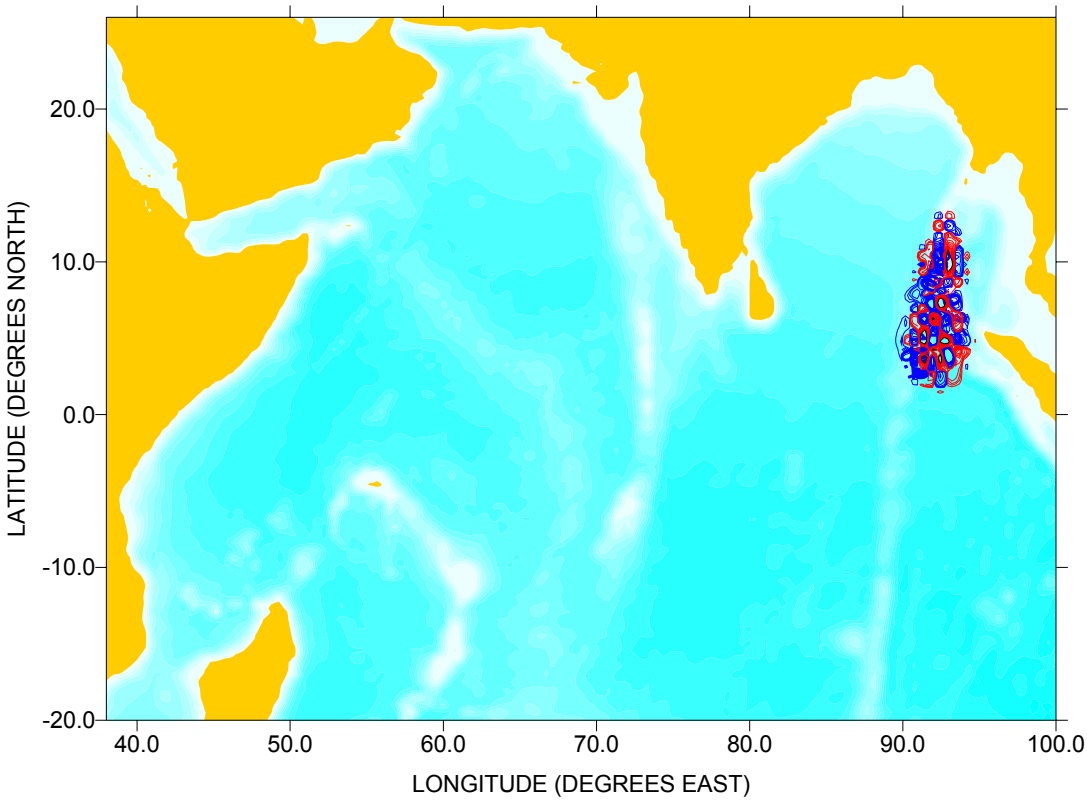

Figure 4. Simulated wave height (m) 15 minutes after the earthquake. Red contour denotes positive wave and blue contour denotes negative wave.

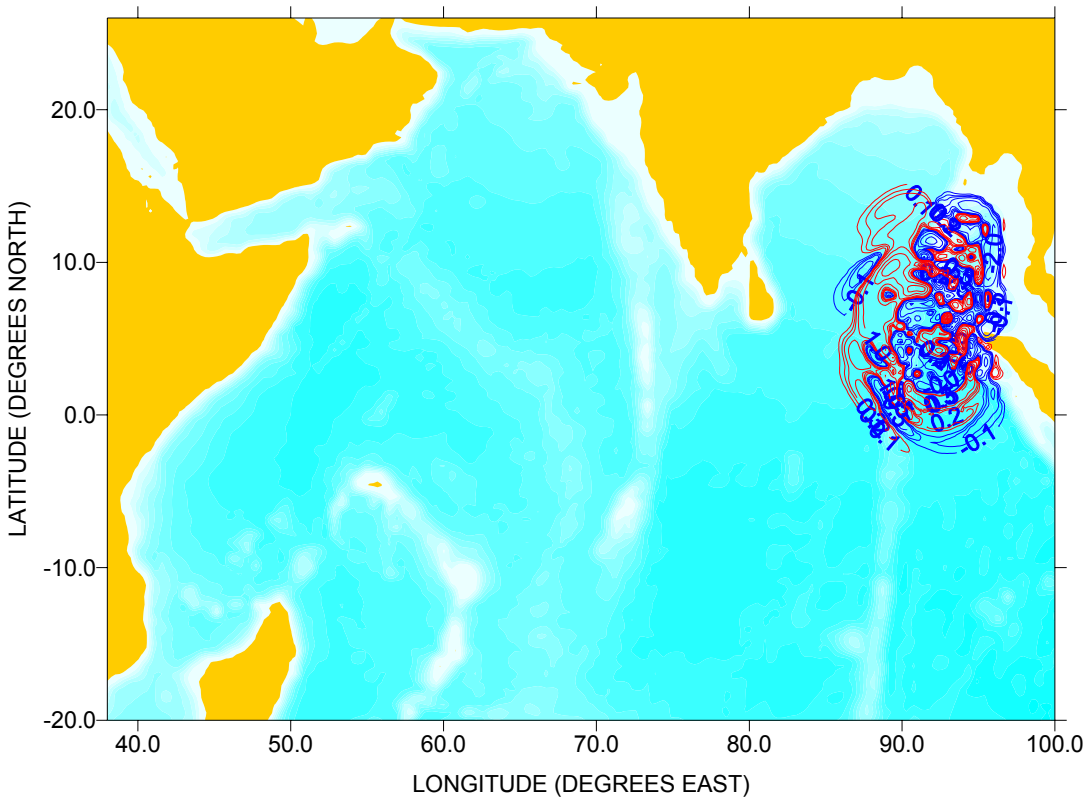

Figure 5. Simulated wave height (m) 1 hour after the earthquake. Red contour denotes positive wave and blue contour denotes negative wave.

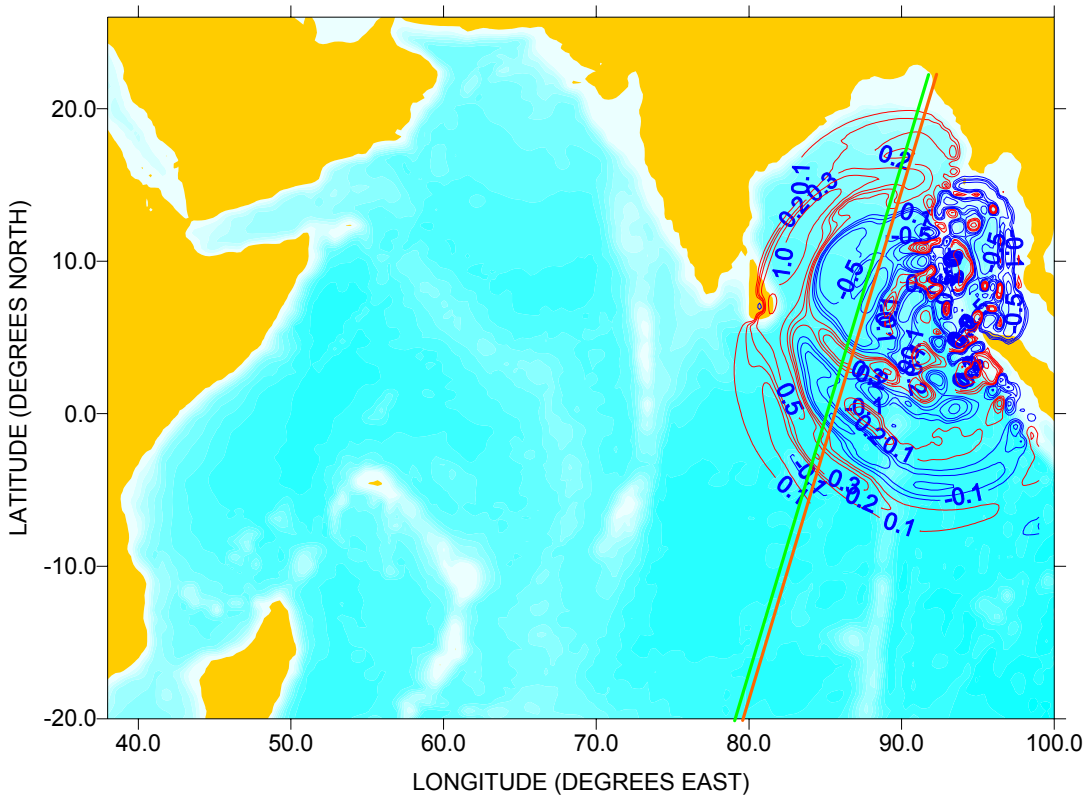

Figure 6. Simulated wave height (m) 2 hours after the earthquake. Red contour denotes positive wave and blue contour denotes negative wave.

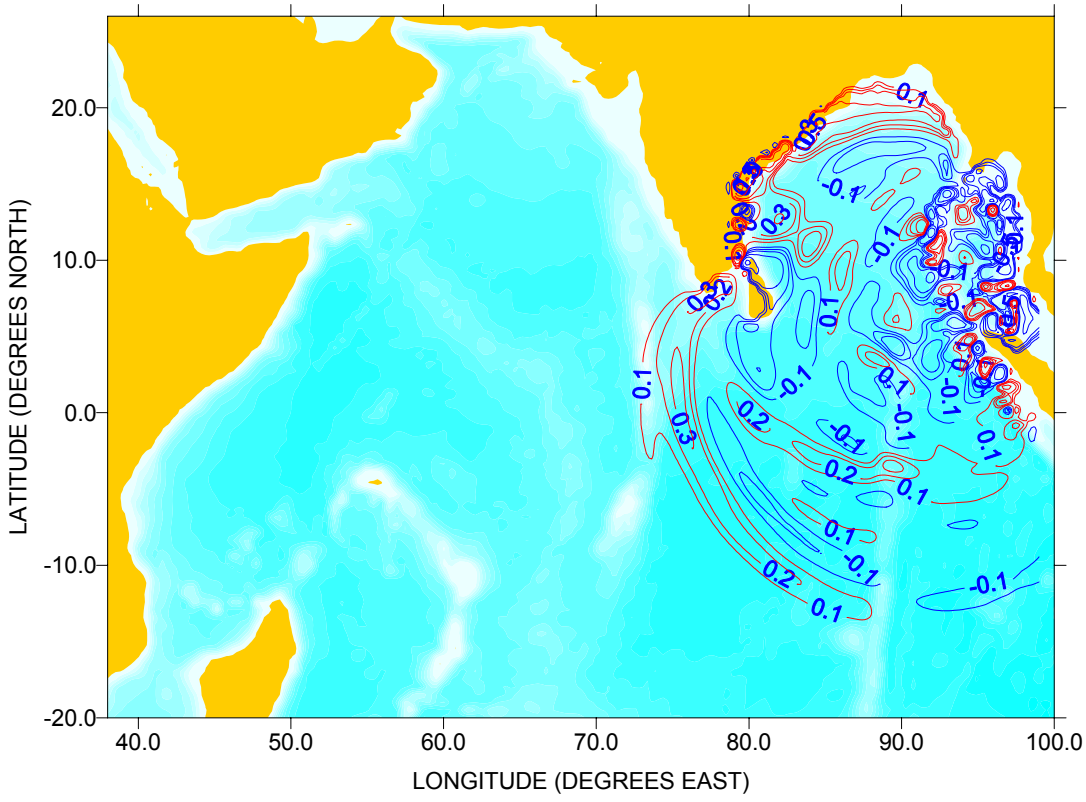

Figure 7. Simulated wave height (m) 3 hours after the earthquake. Red contour denotes positive wave and blue contour denotes negative wave.

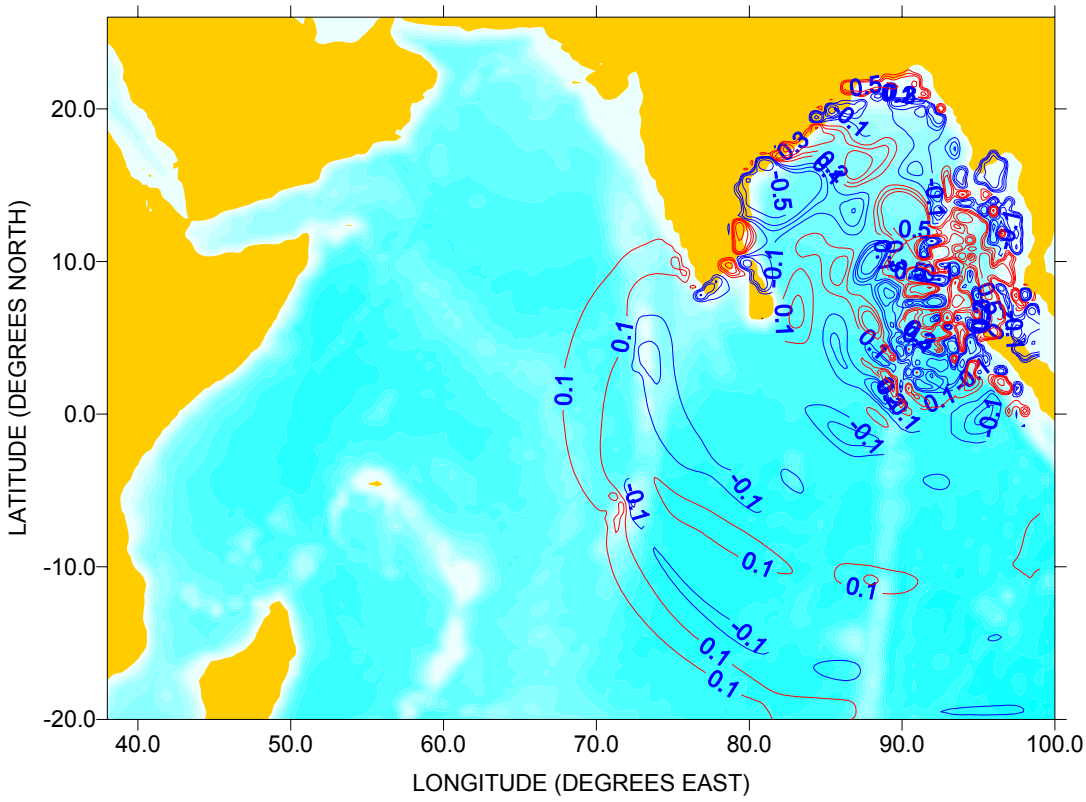

Figure 8. Simulated wave height (m) 4 hours after the earthquake. Red contour denotes positive wave and blue contour denotes negative wave.

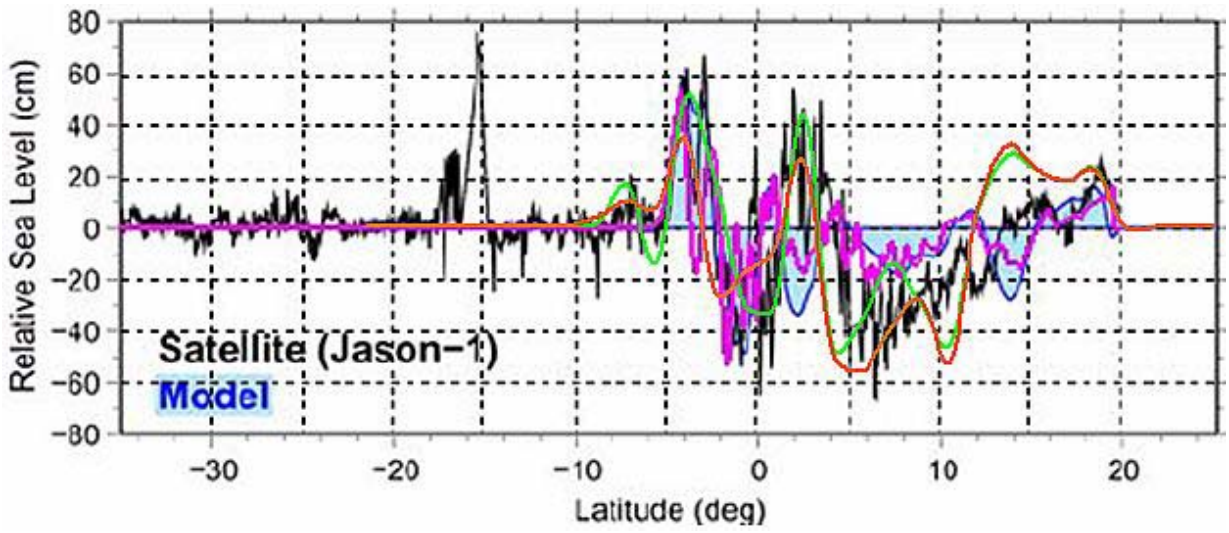

Figure 9. Comparison of computed and observed wave heights. The satellite data (Jason-1) were taken about 2 hours after the quake. The results of the present study are shown in green and orange lines along tracks shown in Figure 6. The blue line is from Pedersen et al (2005).

5.0 CONCLUSIONS AND RECOMMENDATIONS

It is shown in the present study that with the proposed generation model and dispersive wave model, the observed features of the Asian tsunami such as the initial drying of areas east of the source region, the initial flooding of western coasts, and the formation of a series of waves are correctly simulated. The new dynamic model for tsunami generation can be used to analyze the effects of various factors in the tsunami inception such as earthquake moment magnitude, fault-line orientation, focal depth of the earthquake, and various ocean properties

such as vertical stability and variable depths (e.g. bathymetric slope). The proposed tsunami propagation and transformation model can account for most of the observed wave characteristics as they travel through variable ocean bathymetry and coastal geometry. With adjusted parameter values, the tsunami model can explain the independent and combined effects of various factors related to the seismic disturbance and ocean properties where tsunamis occur. The new generation model may also be used to explain the occurrence of a series of large waves induced by landslides, volcanic eruption, or avalanches plunging in deep lakes or seas via the horizontal current acceleration that is produced. As long as there is a sufficiently strong horizontal current induced by such geological disturbances in a deep water basin, a series of waves can be created and modeled using the present model.

Model calibration requires accurate information about the earthquake magnitude, orientation of ruptured fault line, current amplitudes generated during the earthquake, accurate wave height observations and realistic frictional resistance coefficient. As observations of currents in deep waters during a tsunami are virtually absent, the present tsunami generation model has a major technological consequence as current meters are normally intended for deployment in shallow waters. Instead of measuring only the pressure at the seabed, deep-sea currents should be measured as well.

Another remarkable observation of the present study that merits careful experimentation is that tsunami inundation defies a classical oceanographic and hydrodynamic principle where wave breaking normally occurs whenever the wave height attains a certain fraction of the water depth. Due to its very long wave length, the wave breaking limit (i.e. maximum ratio of wave height to water depth previously believed to be about 1.2) may be far exceeded and tsunami waves do not readily break during propagation to shallow coastal waters. The hypothesis of a much higher breaking index awaits careful experimental study. In addition, the new generation mechanism may also be tested experimentally in a hydraulic laboratory. This requires accurate measurements of currents and waves which should be compared to the strength of the disturbing force.

Finally, the inherent complexity of tsunami generation and propagation in a complex ocean environment can always hamper a sensible tsunami warning system. But as new knowledge and understanding from accurately collected data and interpretation becomes available, these should be used so that a better warning system may be put in place. Accurate model prediction especially with regards to wave amplitudes and phases can imply an improved warning system in terms of tsunami magnitude and arrival time. To have a better simulation result, higher spatial resolution is needed and it is therefore recommended to have a grid distance as low as 1 min (as in Kowalik et al. 2005). The inundation of low-lying areas can be handled by using the wave output of such high-resolution model as input into a very fine mesh (50-250 m) within the devastated areas. Hazard mapping in populated coastal areas prone to floods from tsunami (or storm surges) definitely needs an ultra-high resolution in space.

REFERENCES

Abbott MB, McCowan AD & Warren IR (1984). Accuracy of short-wave numerical models. J. Hydr. Eng. Vol. 100, No. 10. pp. 1287-1301.

Dotsenko SF & Soloviev SL (1988). Mathematical simulation of tsunami excitation by dislocations of ocean bottom. Sci. Tsunami Hazards. Vol. 6, No. 1. pp. 31-36.

Kofoed-Hansen H, *et al.* (2005). Simulation of long wave agitation in ports and harbors using a time-domain Boussinesq model. Proc. 5th Intl Symposium on Ocean Wave Measurement and Analysis – WAVES. Madrid, Spain.

Koutitas C & Laskaratos A (1988). Tsunami-induced oscillations in Corinthos Bay: Measurements and 1-D vs 2-D Mathematical Models. Sci. Tsunami Hazards. Vol. 6, No. 1.pp 51-56.

Kowalik Z, Knight W, Logan T, & Whitmore, P (2005). Numerical modeling of the global tsunami: Indonesian Tsunami of 26 December 2004. Sci Tsunami. Hazards, Vol. 23, No. 1 p. 40.

Kowalik, Z (2003). Basic relations between tsunami calculation and their physics – II, Sci. Tsunami Hazards, Vol. 21, No. 3, 154-173.

Kulikov (2005). The highly dispersive waves of the Indian Ocean Tsunami. Russian Academy of Sciences.

Hunt, B. (1993). A mechanism for tsunami generation. J. of Hydraulic Research. IAHR. Vol. 31. pp. 111-120

Madsen, PA & Sorensen, OR (1992). A new form of the Boussinesq Equations with improved linear dispersion characteristics, Part 2: A slowly-varying bathymetry. Coastal Engineering. Vol. 18, No. 1, pp 183-204.

Merrifield M, *et al.* (2005). Tide gauge observations of the Indian Ocean Tsunami, December 26, 2004.

Nosov MA & Skachko N (2001). Non-linear mechanism of tsunami generation by bottom oscillations. ITS 2001. PMEL-NOAA.

Ortiz M, Gomez-Reyes E & Velez-Munoz HS (1999). A fast preliminary estimation model for transoceanic tsunami propagation. International Tsunami Symposium. 2001.

Pedersen, NH, Rasch PS, & Sato, T (2005). Modelling of the Asian Tsunami off the Coast of Northern Sumatra. Danish Hydraulic Institute Technical Paper. March 2005.

Peregrine DH (1967). Long waves on a beach. J. Fluid. Mech. 27, pp. 815-827.

Rivera PC (1997). Hydrodynamics, sediment transport and light extinction off Cape Bolinao, Philippines. 244 p. Balkema Press, The Netherlands.

Stelling GS (1984). On the construction of computational methods for shallow water flow problems. Rijkwaterstaat comms. No. 35, The Hague, The Netherlands.

Titov V, Gonzalez F, Mofjeld H & Venturato A (2003). NOAA TIME Seattle Tsunami Mapping Project: Procedures, Data Sources and Products. PMEL/NOAA. NOAA Technical Memorandum. OAR/PMEL -124.

Todorovska M & Trifunac M (2000). Generation of tsunamis by a slowly spreading uplift of the sea floor. Soil Dyn. Earth. Eng. Vol. 21, pp 151-167.

Villenueve, M & Savage, S. (1993). Nonlinear, dispersive, shallow-water waves developed by a moving bed. J. Hydr. Res. J. Hydr. Res. Vol. 31, pp. 249-265.

Wu, T Y. (1981). Long waves in ocean and coastal waters. J Eng. Mech. Div. ASCE. 107, No. EM3, pp.501-522.

TWO-DIMENSIONAL SIMULATIONS OF EXPLOSIVE ERUPTIONS OF KICK-EM JENNY AND OTHER SUBMARINE VOLCANOS

Galen Gisler
Los Alamos National Laboratory and University of Oslo
Robert Weaver
Los Alamos National Laboratory,
Michael L. Gittings
Science Applications International
Los Alamos, NM, USA

ABSTRACT

Kick-em Jenny, in the Eastern Caribbean, is a submerged volcanic cone that has erupted a dozen or more times since its discovery in 1939. The most likely hazard posed by this volcano is to shipping in the immediate vicinity (through volcanic missiles or loss-of-buoyancy), but it is of interest to estimate upper limits on tsunamis that might be produced by a catastrophic explosive eruption. To this end, we have performed two-dimensional simulations of such an event in a geometry resembling that of Kick-em Jenny with our SAGE adaptive mesh Eulerian multifluid compressible hydrocode. We use realistic equations of state for air, water, and basalt, and follow the event from the initial explosive eruption, through the generation of a transient water cavity and the propagation of waves away from the site. We find that even for extremely catastrophic *explosive* eruptions, tsunamis from Kick-em Jenny are unlikely to pose significant danger to nearby islands. For comparison, we have also performed simulations of explosive eruptions at the much larger shield volcano Vailulu'u in the Samoan chain, where the greater energy available can produce a more impressive wave. In general, however, we conclude that explosive eruptions do not couple well to water waves. The waves that are produced from such events are turbulent and highly dissipative, and don't propagate well. This is consistent with what we have found previously in simulations of asteroid-impact generated tsunamis. Non-explosive events, however, such as landslides or gas hydrate releases, do couple well to waves, and our simulations of tsunamis generated by sub-aerial and sub-aqueous landslides demonstrate this.

INTRODUCTION

Water and magma make a highly explosive combination, particularly at water depths less than about 130 meters. The explosive vaporization of water, heated by contact with magma at 1200 C or hotter, produces an instantaneous pressure of ~50 kBar, that can have extremely dangerous consequences. The August 1883 explosion of Krakatau is thought to have been caused by this hydromagmatic mechanism. This event produced tsunami that killed many thousands of people in the near vicinity, and propagated (though much more weakly) around the world.

It is of interest to discuss whether there is a significant danger of tsunami from the submarine volcano Kick-em Jenny in the eastern Caribbean. We conclude here that there is not. The simulations that we have performed, in an axisymmetric geometry resembling Kick-em Jenny, suggest that only for very much more energetic events are significant waves generated, and that even these waves do not propagate as classical tsunami. These results are consistent with conclusions we have drawn from simulations of other explosively-generated waves.

Kick-em Jenny, located 8 km north of the island of Grenada in the volcanic arc of the Lesser Antilles, is one of the most active volcanos in the region. It has erupted a dozen times since 1939, and is a known hazard to shipping, marked on navigation charts. The principal dangers caused by Kick-em Jenny are from volcanic missiles projected to altitudes of a few hundred meters, and from gases emitted into the seawater from the volcano, reducing the density of the water and thereby causing ships to lose buoyancy. No significant tsunami have been observed to arise from these eruptions, which have generally been of magnitude between 0 and 1 on the Volcanic Explosivity Index (VEI) scale (Simkin et al 1981), though there were early reports of minor waves.

Smith and Shepherd (1993, 1995, 1996) investigated the tsunami hazard posed by the Kick-em Jenny volcano. While the top of the volcanic cone is at a depth such that the hydrostatic water pressure confines the explosive effects of the eruption, bathymetric surveys conducted during the 1960s and 1970s led to the impression that the cone was building towards the surface, and therefore might eventually pose a tsunamigenic hazard from the explosive vaporization of sea water in a major eruption. Smith and Shepherd therefore studied this potential hazard by using linear theory to calculate initial amplitudes, dispersion, and propagation, and shoaling, given a spectrum of potential events and their probability. Their worse case scenario included run-ups as high as 46 meters on the northern shore of Grenada for a VEI=6, or Krakatau-like event, considered as potentially likely on a 1000-year scale, or as high as 8 meters for a more realistic, 100-year, VEI=3 event.

This potential threat has recently been downplayed, owing mostly to bathymetry obtained in a March 2002 multi-beam survey (Lindsay, Shepherd, and Wilson, 2005), which was conducted after the publication of the Smith and Shepherd papers. This recent bathymetry suggests that the depth of the Kick-em Jenny summit, now at 185 m, has not significantly diminished since the first report in 1966 of 192 m. The immediate danger from tsunami that might potentially be caused by this volcano is therefore now thought to be insignificant. Nevertheless, it is of interest to study the role of underwater volcanic explosive eruptions in producing tsunami in the general case with particular application to this very interesting case.

Accordingly, we have conducted a series of two-dimensional axisymmetric simulations of explosive underwater volcanic eruptions to study the coupling of these events to the production of water waves.

THE SAGE HYDROCODE

The SAGE hydrocode is a multi-material adaptive-grid Eulerian code with a high-resolution Godunov scheme originally developed by Michael Gittings for Science Applications International (SAIC) and Los Alamos National Laboratory (LANL). It uses continuous adaptive mesh refinement (CAMR), by which we mean that the decision to refine the grid is made cell-by-cell and cycle-by-cycle continuously throughout the problem run. Refinement occurs when gradients in physical properties (density, pressure, temperature, material constitution) exceed user-defined limits, down to a minimum cell-size specified by the user for each material in the problem. With the computing power concentrated on the regions of the problem which require higher resolution, very large computational volumes, and substantial differences in scale, can be simulated at low cost.

SAGE can be run in several modes of geometry and dimensionality, explicitly 1-D Cartesian and spherical, 2-D Cartesian & cylindrical, and 3-D Cartesian. The RAGE code is similar to SAGE but incorporates a separate module for implicit, gray, non-equilibrium radiation diffusion. Both these codes are part of LANL's Crestone project, in turn part of the Department of Energy's program in Advanced Simulation and Computing, or ASC.

Because modern supercomputing is commonly done on machines or machine clusters containing many identical processors, the parallel implementation of the code is supremely important. For portability and scalability, SAGE uses the widely available Message Passing Interface (MPI). Load leveling is accomplished through the use of an adaptive cell pointer list, in which newly created daughter cells are placed immediately after the mother cells. Cells are redistributed among processors at every time step, while keeping mothers and daughters together. If there are a total of M cells and N processors, this techniques gives very nearly M/N cells per processor. As neighbor-cell variables are needed, the MPI gather/scatter routines copy those neighbor variables into local scratch.

In a multi-material code like SAGE, every cell in the computational volume can contain all the materials defined in the problem, each with its own equation of state (and strength model, as appropriate). There are a number of equations of state available, analytical and tabular. In the calculations reported here, we use the LANL SESAME tables for air and basalt, and for water we used a somewhat more sophisticated table (including a good treatment of the vapor dome) from SAIC. For the strength of basalt, we used a simple elastic-plastic model with pressure hardening (with depth) for the basalt.

The boundary conditions we use in these calculations are designed to allow unhindered outflow of waves and material. This is accomplished by the use of "freeze regions" around the edges of the computational box, which are updated normally during the hydrodynamic step, then quietly restored to their initial values of pressure, density, internal energy, and material properties before the next step. This technique has proven to be extremely effective at minimizing the deleterious effect of artificial reflections. But by far the best technique for dealing with unwanted boundary effects is to put the boundaries very far away from the regions of interest or to place the boundary beyond a material interface that truly exists in the problem and might be expected to interact

with waves in an appropriate way (i.e. through reflection, transmission, and absorption).

SIMULATIONS OF KICK-EM JENNY

For the sake of simplicity, we perform our simulations in two-dimensions only, ignoring the very real three-dimensional character of the Kick-em Jenny volcano. Its cinder cone is embedded in a horseshoe-shaped slump caused by slope failure from a larger mound to its east. The event that caused this slump must have produced significant tsunami, and we shall argue that the danger from future such slumps is greater than from eruptive events on the cinder cone. The geometry of the slump and other three-dimensional features would provide collimation and amplification of eruptively produced waves that propagate in certain directions while attenuating waves that propagate in other directions. We ignore these effects in order to focus solely on the generative mechanism.

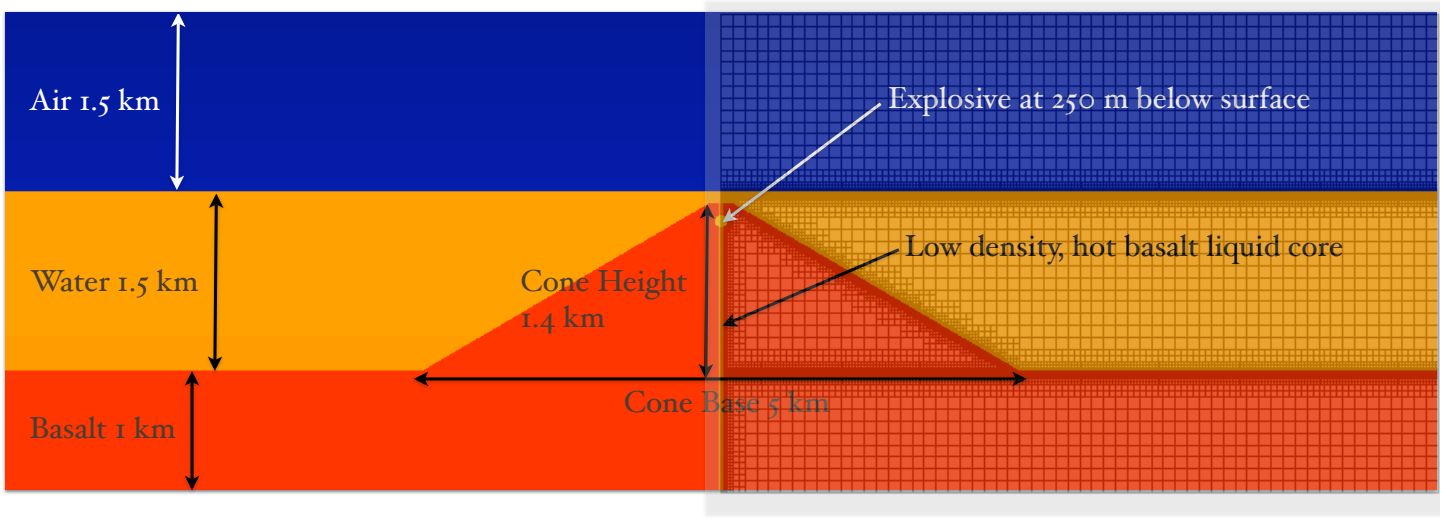

Figure 1. Geometry of SAGE set-up for Kick-em Jenny simulations. Colors indicate density, with red representing the basalt of the crust and cone, orange the water, and blue the air. Dimensions are as indicated, and the diagram is in proportionate scale. On the right we show the initial gridding of the problem as set up by the SAGE code. Before any dynamics have occurred, the grid is refined only at the material interfaces.

Accordingly, we model the volcano as a simple geometrical frustum, with a base of 5 km diameter, a top of 100 m diameter, and a height of 1.4 km (see Fig. 1). The cone has a hot magma core of 20 m diameter. We take the water depth to be 1.5 km, so that the submerged top of the frustum is only 100 m below the water surface, thus significantly shallower than the true cone summit, and above the threshold depth for pressure confinement of a hydromagmatic eruption. We use three materials in the problem, air for the atmosphere, water for the ocean, and basalt for the seafloor, the volcanic cinder cone, and the hot magma core. We use tabular equations of state for these from the LANL Sesame Library except for water, which we take from a high-quality SAIC table. We use a simple elastic-plastic strength model for the solid basalt, and no strength for the magma, water, or air.

To model an explosive eruption, we take the extreme (and admittedly unlikely) case of an instantaneous

explosion near the top of the cone. Because we anticipate that the strongest coupling to the water motion will be through the motion of rock, we do not place the explosion at the summit, but some depth (usually 150 m) below the summit.

We present here three sample runs that span the range of interest. The parameters of these runs, and the resulting maximum wave heights are presented in Table I.

We chose these parameters to span a major portion of the range of interest, as an exploration of what waves might possibly be generated by significant explosive eruptions at Kick-em Jenny. Our extrapolated wave heights at 10 km distance are significantly less than reported by Smith and Shepherd (1993).

Table I. Summary of important runs.

run name	VEI	initial source energy (megatons)	wave energy at 60 seconds (megatons)	wave height at 3 km (meters)	extrapolated wave height at 10 km (meters)
kej11	5.5	233	2.11	300	37
kej12	4.5	21.2	0.0254	130	21
kej13	3.7	3.71	0.0078	20	2.7

We illustrate these three runs by showing the final density configuration in Figure 2. The explosive energy is sourced in instantaneously at the beginning of the calculation. A hot crater quickly opens in the basalt, and the explosive vaporization of the water in contact with this crater produces a large transient water cavity. A “debris curtain” or rim wave makes a precursor tsunami that dies off very quickly. The main wave is produced by the collapse of the transient water cavity, and the strong water currents modify the shape of the basalt crater produced in the explosion. The wave that is produced by the cavity collapse is very turbulent and dissipative, and it propagates slowly. When the main wave leaves the computational domain (6 km from the center), we terminate the simulation, though the center is still hot and turbulent.

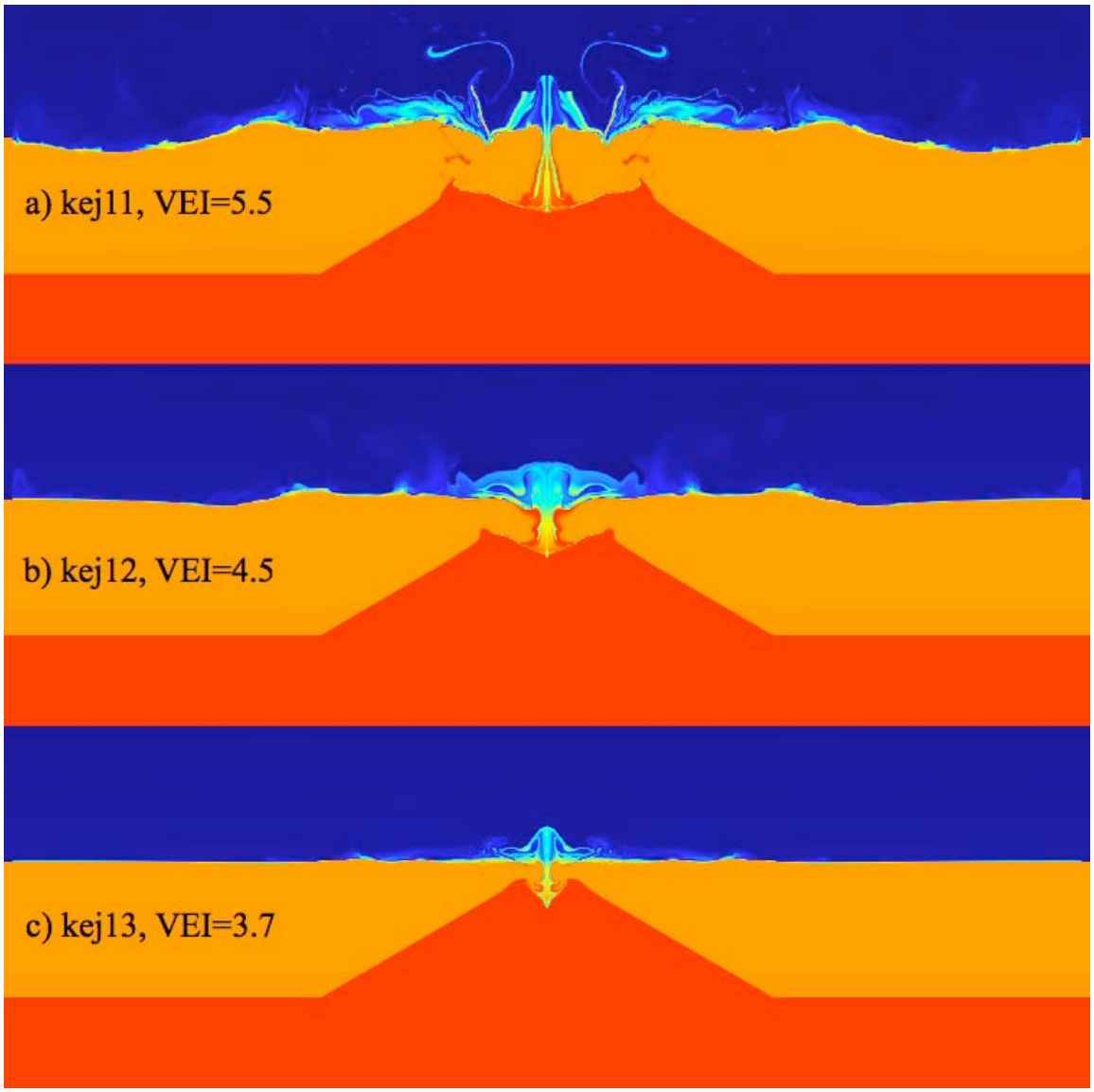

Figure 2. Final wave profiles for the three representative runs.

This relative inefficiency of coupling for explosive energy deposition is similar to the inefficiency we have previously found for coupling of asteroid impacts to tsunami wave energy. In the latter case we have found that impact-generated waves decline rather more steeply with distance than waves from seismic or landslide events, and their speeds and wavelengths are correspondingly lower (Gisler et al. 2002).

The coupling of source energy to eventual wave energy is much less efficient in the explosive release case that we are considering here than it is for slower mechanisms of energy release. As seen in Table I, only 2% of the source energy for run kej13 goes into the wave, reducing to < 1% for the most energetic run, kej11. The kinetic energy histories for the principal components of the simulation are shown in Figure 3 for the middle run of Table 1. Much more of the initial source energy is transformed directly into the internal energies of the various components, and mainly goes into the vaporization of water and the melting of basalt.

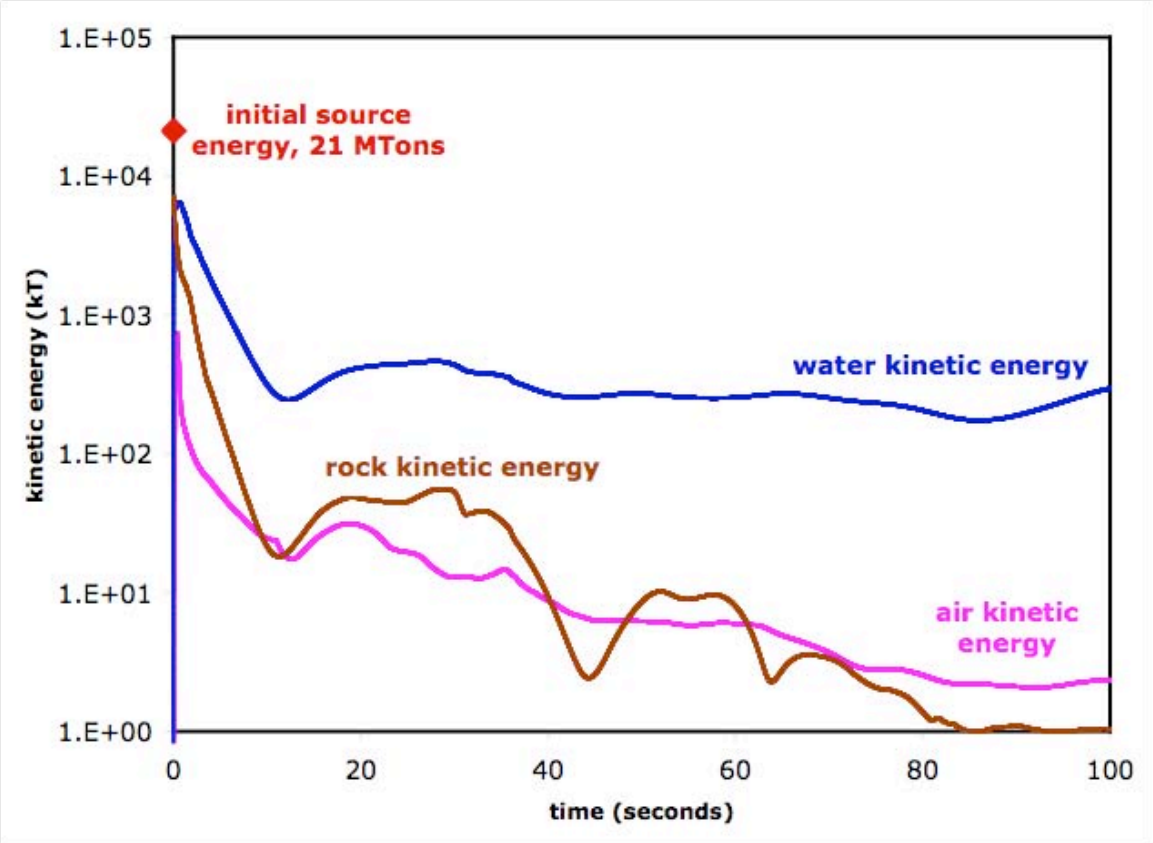

Figure 3. History of material kinetic energies for our run kej11, with an initial explosive energy of 21 MTons.

For comparison, we have performed simulations of underwater and subaerial granular basalt landslide events with free energy ~20 MTons, comparable to our kej12 explosive eruption simulation, and find in these cases coupling efficiencies (source potential energy to water kinetic energy) of 15% to 25% depending on the circumstances.

We also performed simulations of explosive eruptions on the massive shield volcano Vailulu'u, at the end of the Samoan chain. While such eruptions are even less likely in that case than in the case of Kick-em Jenny, we thought it useful to examine a case that was larger in dimension and energy availability. In that case also we find that the coupling to water waves is in general of very poor efficiency. However, if we artificially weaken the strength parameters for basalt so that the rock deformation is substantially greater than in the nominal case, the coupling efficiency, wave heights, and consequently the wave kinetic energy are considerably enhanced. In the extreme we get a coupling efficiency of 25%.

We conclude that the efficient production of a tsunami requires a disturbance that covers a substantial distance or lasts a considerable time. Earthquakes or long-runout landslides, or more generally a movement of the seafloor or a pressure pulse communicated by the seafloor, produce tsunamis efficiently. Explosions or impacts do not couple to water motion as efficiently as do slower motions of rock.

Specifically, the tsunami danger from explosive eruptions of Kick-em Jenny is much less important than the

danger that might result from a slope failure at that volcano, similar to that which caused the horseshoe-shape cleft in which the volcano currently nestles.

References

Galen Gisler, Robert Weaver, Charles Mader, Michael L. Gittings, “Two and three-dimensional simulations of asteroid ocean impacts”, *Science of Tsunami Hazards*, **21**:119-134 , 2003.

Jan M. Lindsay, John B. Shepherd and Doug Wilson, “Volcanic and scientific activity at Kick ’em Jenny submarine volcano 2001-2002: implications for volcanic hazard in the Southern Grenadines, Lesser Antilles”, *Natural Hazards,* **34**:1-24, 2005.

T. Simkin, L. Siebert, L. McClelland, D. Bridge, C. Newhall, and J. H. Latter, *Volcanoes of the World*, Smithsonian Institution, Hutchinson Ross, Stroudsburg , 1981.

Martin S. Smith and John B. Shepherd, “Preliminary investigations of the tsunami hazard of Kick ’em Jenny submarine volcano,” *Natural Hazards*, **7**:257-277 , 1993.

Martin S. Smith and John B. Shepherd, “Potential Cauchy-Poisson waves generated by submarine eruptions of Kick 'em Jenny volcano,” *Natural Hazards*, **11**:75-94 , 1995.

Martin S. Smith and John B. Shepherd, “Tsunami waves generated by volcanic landslides: an assessment of the hazard associated with Kick ’em Jenny”, In: W. J. McGuire, A. P. Jones, and J. Neuberg, (eds), *Volcano Instability on the Earth and Other Planets, Geol. Soc. Spec. Pub.* No. 110, pp. 115–123, 1996.

WAVE DISPERSION STUDY IN THE INDIAN OCEAN TSUNAMI OF DECEMBER 26, 2004

Juan Horrillo and Zygmunt Kowalik
Institute of Marine Science
University of Alaska Fairbanks
Fairbanks, Alaska

Yoshinori Shigihara
National Defense Academy of Japan.

ABSTRACT

A numerical study which takes into account wave dispersion effects has been carried out in the Indian Ocean to reproduce the initial stage of wave propagation of the tsunami event occurred on December 26, 2004. Three different numerical models have been used: the nonlinear shallow water (nondispersive), the nonlinear Boussinesq and the full Navier-Stokes aided by the volume of fluid method to track the free surface. Numerical model results are compared against each other. General features of the wave propagation agreed very well in all numerical studies. However some important differences are observed in the wave patterns, i.e., the development in time of the wave front is shown to be strongly connected to the dispersion effects. Discussions and conclusions are made about the spatial and temporal distribution of the free surface reaffirming that the dispersion mechanism is important for tsunami hazard mitigation.

INTRODUCTION

The recorded and observed tsunami waves originated by earthquake of 26 December, 2004 showed complicated temporal and spatial structure, since the initial wave generated by the bottom uplift had multiple amplitude and frequency components.

Analysis of the recorded data demonstrated that the tsunami waves propagating southwestward across the Indian Ocean two hours after the main shock were noticeably dispersive (Kulikov, 2005). Dispersion effects can be significant for amplitude estimation in transoceanic tsunami propagation. This brings into question the accuracy of the model used for numerical simulations of tsunamis. Usually, tsunami models are based on the shallow water approximation which ignores the effect of linear wave dispersion.

As the initial wave propagates, separation of the wave into spectral components with different frequencies and amplitudes occurs. Thus, the leading wave is followed by a train of waves formed in its tail. In coastal regions this train of waves interacts with the leading wave's runup, drawdown and reflection from shelf or land, introducing strong modification to leading wave effects. We aim, therefore, to infer the role of the dispersion effects in tsunami wave modification.

Often populated areas along coasts are located in low-lying and flat regions that together with natural and man made obstacles make the retreat of the flood caused by the first tsunami wave very slow. Under this situation, subsequent waves as they shallow often ride over a region already flooded by the first wave allowing these waves to impinge on structures, often with higher sea level and speed.

The multiple wave phenomenon was observed throughout the Sri Lanka coast, as described in John Headland's report at the ASCE web page (http://www.asce.org/page/?id=53.). The first few rows of houses were destroyed by the tsunami wave, and acted to dissipate it. Interior houses, as a result, were not as extensively damaged. In another location along the coast; one witness said. 'It wasn't one wave, it came in great surges, each one deeper than the last and pushing the water that had come in before in front of it'. In fact, most witnesses talked of three main waves. The first knocked them off their feet, the second picked them up and carried them, often at up to 50 km/h, and the third, the most powerful, bore them high, up to 15 m in some places or sucked them under. To explain these phenomena is not a simple task, since a train of waves approaching a particular coastal region, in addition to the transformation it may have experienced by dispersion effects, could be composed of a combination of waves coming from different parts of the source or it may be that these waves have been diverted by the ocean bathymetry or transformed by a submerged bar. Since this study intends to investigate the role of dispersion effects in tsunami calculations and its possible implication in propagation and runup, simplified model setups are used (one/two-dimensional) so that tsunami physics and behavior can be better explained.

Several studies have highlighted the importance of dispersion effect in tsunami propagation. Sato (1996), in the numerical calculation of the 1993 Okushiri Island tsunami, found that local tsunami enhancement can be explained by a series of dispersive waves which ride on the main tsunami front. Ortiz *et al.* (2001) suggested that the frequency dispersion mechanism, as prescribed by dispersive theory plays the main role in propagation of large and medium-size tsunamis. Heinrich *et al.* (1998) using the Boussinesq approach, found that the effect of dispersion can be significant. Imamura *et*

al. (1988, 1990) and Liu *et al.* (1995) also considered the effect to be important.

In tsunami calculations the dispersive effects are usually considered through the Boussinesq equation, Dunbar *et al.* (1991); Madsen *et al.* (1999). Their numerical solutions require small space steps and often implicit schemes are used due to stringent numerical stability requirement (Shigihara, 2004). As the second order approximation to the numerical schemes leads to an error of approximation proportional to the third derivative, and since the dispersion terms in the Boussinesq equation also depend on the third derivative, Imamura and Shuto (1989) constructed a numerical scheme which uses numerical dispersion to simulate physical dispersion. This scheme was improved and applied to the propagation of tsunamis over slowly varying topography by Yoon (2002), thus opening the possibility to account for the dispersion of distant tsunamis. In the runup region, at the steep wave front where the tsunami wave starts to break, the dispersive effects due to physical processes tend to interact with the short wave numerical instability generating turbulent motion. To suppress such oscillations, Goto and Shuto (1983) and Sato (1996) suggested introduction of the eddy diffusivity term. The nonlinear shallow water (NLSW, nondispersive), the nonlinear Boussinesq (NLB) and the full Navier-Stokes equations aided by the volume of fluid method to track the water surface (FNS-VOF) are important tools for the tsunami investigations. Using these tools and hydraulic experiments Fujima (2001) examined the wave transformation on large bottom obstacles. He pointed out that NLB approach when compared with experiments and FNS-VOF approach, reproduces the wave dispersion effects well.

This study aims to reproduce the Indian Ocean Tsunami (IOT) of Dec. 26, 2004 in its initial stage (two hours of tsunami wave propagation). With the help of three different numerical tools for tsunami calculation we intend to uncover some of the implications of dispersion effects in tsunami propagation and runup. The study is organized as follows: first, a brief description of the models formulation and their numerical schemes is presented. Afterwards, several numerical experiments are described based on initial conditions for free surface deformations. Then, model results are compared against each other. Finally, observations and model results are analyzed to draw conclusion on the spatial and temporal distributions of the free surface.

NUMERICAL METHODS

For the numerical computation three case studies have been carried out a) one-dimension: the channel case; b) two-dimension: the Bay of Bengal case; c) one-dimension Yala/Banda-Aceh cases. In case a) an imaginary channel along a given transect is chosen. A study is made for validation and comparison of the models (NLB and FNS-VOF) to show dispersive properties of tsunami and limitations of the NLSW approach. In case b) a small domain which encompasses the south part of the Bay of Bengal is used for the numerical simulations. Comparisons are made between NLB and NLSW models to uncover dispersive effects. In case c) simplified studies in which one-dimensional channels are used again to reveal wave runup of dispersive waves. The NLSW and NLB models are used in these cases, and initial conditions at the open side of the channels are taken from the two-dimensional models results.

In all numerical simulation, the bathymetry is taken From GEBCO data bank using 1 min resolution. The bathymetric profile along transects (one-dimensional cases) are obtained by linear interpolation from the GEBCO data bank. Initial condition for the free

surface deformation is detailed in Kowalik *et al.* (2005) according to the static dislocation formulae from Okada (1985).

Description of NLSW Model

The nonlinear shallow water equations of motion and continuity are taken in the following form (Kowalik and Murty 1993a)

$$\frac{\partial u}{\partial t} + u\frac{\partial u}{\partial x} + v\frac{\partial u}{\partial y} + g\frac{\partial \zeta}{\partial x} + \frac{1}{\rho D} ru\sqrt{u^2 + v^2} = 0, \tag{1}$$

$$\frac{\partial v}{\partial t} + u\frac{\partial v}{\partial x} + v\frac{\partial v}{\partial y} + g\frac{\partial \zeta}{\partial y} + \frac{1}{\rho D} rv\sqrt{u^2 + v^2} = 0, \tag{2}$$

$$\frac{\partial \zeta}{\partial t} + \frac{\partial uD}{\partial x} + \frac{\partial vD}{\partial y} = 0, \tag{3}$$

where ρ is the water density, u and v are vertically averaged velocity components along x and y directions respectively, H is the mean water depth, ζ is the sea level, $D = (\zeta + H)$ is the total depth, r is the friction coefficient, and g is the gravitational acceleration.

Above equations are solved numerically by using a staggered grid (C grid) in space as shown in Fig. 1. Velocity locations for u and v are denoted by horizontal and vertical bars respectively. The u velocity grid points are offset from the v velocity grid points. Sea level locations are denoted by crosses. Velocity components and sea level (u, v and ζ) are organized into triplets as shown by the triangles. The depth is defined at the sea level location. To resolve the nonlinear terms in the equations of motion the v velocity is needed at the u locations and vice versa. To visualize how the averaged values are constructed, dark-gray and plain-gray circles are introduced at the velocity locations. The values of velocity marked by dark-gray circles, when they are averaged, will define the average of v velocity at the u location. The average of v velocity at this location is

$$\overline{v} = 0.25(v_{j,k-1} + v_{j,k} + v_{j-1,k} + v_{j-1,k-1}).$$

In a similar way the average of u velocities (plain-gray circles) at the v point is

$$\overline{u} = 0.25(u_{j+1,k} + u_{j+1,k+1} + u_{j,k+1} + u_{j,k}).$$

The grid size (space step) along the E-W direction is h_x, and the distance is jh_x, index $j = 1,\ldots$. The space step along the N-S direction is h_y and the distance is kh_y, index $k = 1,\ldots$.

The solution of Eqs. (1-3) is usually advanced in time by the two-time-level numerical scheme (Kowalik and Murty, 1993a). For the spatial derivatives a second order approximation is constructed, thus

$$u_{j,k}^{m+1} = u_{j,k}^{m} - \frac{gT}{h_x}(\zeta_{j,k}^{m} - \zeta_{j-1,k}^{m}) - \frac{2T}{\rho(D_{j-1,k}^{m} + D_{j,k}^{m})} ru_{j,k}^{m}\sqrt{(u_{j,k}^{m})^2 + (\overline{v}^{m})^2}$$

$$- \frac{u_p^m T}{h_x}(u_{j,k}^{m} - u_{j-1,k}^{m}) - \frac{u_n^m T}{h_x}(u_{j+1,k}^{m} - u_{j,k}^{m})$$

$$-\frac{\overline{v}_p^m T}{h_y}(u_{j,k}^m - u_{j,k-1}^m) - \frac{\overline{v}_n^m T}{h_y}(u_{j,k+1}^m - u_{j,k}^m), \tag{4}$$

$$\begin{aligned} v_{j,k}^{m+1} = v_{j,k}^m &- \frac{gT}{h_y}(\zeta_{j,k+1}^m - \zeta_{j,k}^m) - \frac{2T}{\rho(D_{j,k}^m + D_{j,k+1}^m)} r v_{j,k}^m \sqrt{(\overline{u}^m)^2 + (v_{j,k}^m)^2} \\ &- \frac{\overline{u}_p^m T}{h_x}(v_{j,k}^m - v_{j-1,k}^m) - \frac{\overline{u}_n^m T}{h_x}(v_{j+1,k}^m - v_{j,k}^m) \\ &- \frac{v_p^m T}{h_y}(v_{j,k}^m - v_{j,k-1}^m) - \frac{v_n^m T}{h_y}(v_{j,k+1}^m - v_{j,k}^m), \end{aligned} \tag{5}$$

where index m stands for the time stepping, T is the time step. $u_p = 0.5(u_{j,k} + |u_{j,k}|)$, $u_n = 0.5(u_{j,k} - |u_{j,k}|)$, $v_p = 0.5(v_{j,k} + |v_{j,k}|)$ and $v_n = 0.5(v_{j,k} - |v_{j,k}|)$ are velocity switches used in the upwind/downwind method to turn on/off the upstream/downstream advective term derivatives, i.e., if $u_{j,k} > 0$ then $u_p = u_{i,j}$ and $u_n = 0$; conversely, if $u_{j,k} < 0$ then $u_p = 0$ and $u_n = u_{j,k}$.

For the large scale computations the upwind/downwind method is essential as it displays strong stability. In order to obtain a higher order approximation in space for the continuity equation the upwind/downwind numerical scheme proposed by Mader (2004) is expanded. The numerical scheme has been improved by an additional interpolation between grid points based on the method of characteristic. Then, the continuity equation becomes

$$\begin{aligned} \zeta_{j,k}^{m+1} = \zeta_{j,k}^m &- \frac{T}{h_x}(flux_{x,j+1,k} - flux_{x,j,k}) \\ &- \frac{T}{h_y}(flux_{y,j,k} - flux_{y,j,k-1}), \end{aligned} \tag{6}$$

where

$$flux_{x,j,k} = u_p^{m+1}\zeta_{p,x} + u_n^{m+1}\zeta_{n,x} + u_{j,k}^{m+1}\frac{(H_{j,k} + H_{j-1,k})}{2}, \tag{7}$$

$$\zeta_{p,x} = (0.5 + u_p^{m+1}\frac{T}{h_x})\zeta_{j-1,k}^m + (0.5 - u_p^{m+1}\frac{T}{h_x})\zeta_{j,k}^m, \tag{8}$$

$$\zeta_{n,x} = (0.5 + u_n^{m+1}\frac{T}{h_x})\zeta_{j-1,k}^m + (0.5 - u_n^{m+1}\frac{T}{h_x})\zeta_{j,k}^m, \tag{9}$$

$$flux_{y,j,k} = v_p^{m+1}\zeta_{p,y} + v_n^{m+1}\zeta_{n,y} + v_{j,k}^{m+1}\frac{(H_{j,k} + H_{j,k+1})}{2}, \tag{10}$$

$$\zeta_{p,y} = (0.5 + v_p^{m+1}\frac{T}{h_y})\zeta_{j,k}^m + (0.5 - v_p^{m+1}\frac{T}{h_y})\zeta_{j,k+1}^m \qquad (11)$$

$$\zeta_{n,y} = (0.5 + v_n^{m+1}\frac{T}{h_y})\zeta_{j,k}^m + (0.5 - v_n^{m+1}\frac{T}{h_y})\zeta_{j,k+1}^m . \qquad (12)$$

The numerical scheme given by Eqs. (7-12) is close to the second order of approximation in space.

For the runup condition the following step is taken, i.e., when the dry point $(j_{wet} - 1)$ is located to the left of the wet point j_{wet},

$$\text{If } (\zeta_{j_{wet}} > -H_{j_{wet}-1}) \text{ then } u_{j_{wet}} = u_{j_{wet}+1},$$

(Kowalik and Murty, 1993b).

Description of NLB Model

Equations of motion of the nonlinear Boussinesq model are taken from Shigihara et al. (2005),

$$\frac{\partial u}{\partial t} + u\frac{\partial u}{\partial x} + v\frac{\partial u}{\partial y} + g\frac{\partial \zeta}{\partial x} + \frac{1}{\rho D} ru\sqrt{u^2 + v^2} = \frac{\partial \psi}{\partial x}, \qquad (13)$$

$$\frac{\partial v}{\partial t} + u\frac{\partial v}{\partial x} + v\frac{\partial v}{\partial y} + g\frac{\partial \zeta}{\partial y} + \frac{1}{\rho D} rv\sqrt{u^2 + v^2} = \frac{\partial \psi}{\partial y}, \qquad (14)$$

where the potential function ψ is defined as

$$\psi = \frac{H^2}{3}(\frac{\partial^2 u}{\partial x \partial t} + \frac{\partial^2 v}{\partial y \partial t}). \qquad (15)$$

By substituting Eqs. (13) and (14) into Eq. (15) and neglecting both, nonlinear and bottom friction terms from the equations of motion, yields the Poisson equation for the solution of ψ as

$$\frac{H^2}{3}(\frac{\partial^2 \psi}{\partial x^2} + \frac{\partial^2 \psi}{\partial y^2}) - \psi = \frac{gH^2}{3}(\frac{\partial^2 \zeta}{\partial x^2} + \frac{\partial^2 \zeta}{\partial y^2}). \qquad (16)$$

Thus, the dispersive wave propagation results in an elliptical problem, where the potential function ψ plays the role of pressure corrector. Applying the same notation used in the previous numerical model, the finite difference forms of the equations of motion are

$$u_{j,k}^{m+1} = u_{j,k}^m - \frac{gT}{h_x}(\zeta_{j,k}^m - \zeta_{j-1,k}^m) - \frac{u_p^m T}{h_x}(u_{j,k}^m - u_{j-1,k}^m) - \frac{u_n^m T}{h_x}(u_{j+1,k}^m - u_{j,k}^m)$$
$$- \frac{\overline{v}_p^{u,m} T}{h_y}(u_{j,k}^m - u_{j,k-1}^m) - \frac{\overline{v}_n^{u,m} T}{h_y}(u_{j,k+1}^m - u_{j,k}^m)$$

$$-\frac{2T}{\rho(D^m_{j-1,k}+D^m_{j,k})}ru^m_{j,k}\sqrt{(u^m_{j,k})^2+(\overline{v}^m)^2}+\frac{T}{h_x}(\psi^m_{j,k}-\psi^m_{j-1,k}), \quad (17)$$

$$v^{m+1}_{j,k}=v^m_{j,k}-\frac{gT}{h_y}(\zeta^m_{j,k+1}-\zeta^m_{j,k})-\frac{\overline{u}^{v,m}_p T}{h_x}(v^m_{j,k}-v^m_{j-1,k})-\frac{\overline{u}^{v,m}_n T}{h_x}(v^m_{j+1,k}-v^m_{j,k})$$
$$-\frac{v^m_p T}{h_y}(v^m_{j,k}-v^m_{j,k-1})-\frac{v^m_n T}{h_y}(v^m_{j,k+1}-v^m_{j,k})$$
$$-\frac{2T}{\rho(D^m_{j,k}+D^m_{j,k+1})}rv^m_{j,k}\sqrt{(\overline{u}^m)^2+(v^m_{j,k})^2}+\frac{T}{h_y}(\psi^m_{j,k+1}-\psi^m_{j,k}). \quad (18)$$

Numerical form of the continuity equation (Eq. 3) is,

$$\zeta^{m+1}_{j,k}=\zeta^m_{j,k}-\frac{T}{h_x}(u^{m+1}_{j+1,k}D^{u,m}_{j+1,k}-u^{m+1}_{j,k}D^{u,m}_{j,k})-\frac{T}{h_y}(v^{m+1}_{j,k}D^{v,m}_{j,k}-v^{m+1}_{j,k-1}D^{v,m}_{j,k-1}). \quad (19)$$

The above explicit numerical scheme uses Eqs. (17-19) to compute velocity and sea level, where Eq. (15) serves to compute the potential function. This computational process is unstable since a new stability condition arises due to dispersive terms. It requires that the space step used for the numerical computation, h_x (assuming $h_x = h_y$), must be $h_x > 1.5H$ (Shigihara, 2004). As the average depth of the Global Ocean is close to 4km the above condition introduces relatively large space steps which lead to poor spatial resolution and numerical instability. To circumvent stability requirements an implicit numerical scheme to derive the potential function has been constructed (Shigihara *et al.* 2005). The numerical scheme uses Poisson equation (Eq. 16) in the following implicit numerical form:

$$[1+\frac{2}{3}H^2_{j,k}(\frac{1}{h_x^2}+\frac{1}{h_y^2})]\psi^{m+1}_{j,k}-\frac{H^2_{j,k}}{3}(\frac{1}{h_x^2}\psi^{m+1}_{j+1,k}+\frac{1}{h_x^2}\psi^{m+1}_{j-1,k}+\frac{1}{h_y^2}\psi^{m+1}_{j,k+1}+\frac{1}{h_y^2}\psi^{m+1}_{j,k-1})$$
$$=\frac{gH^2_{j,k}}{3}[2(\frac{1}{h_x^2}+\frac{1}{h_y^2})\zeta^{m+1}_{j,k}-\frac{1}{h_x^2}\zeta^{m+1}_{j+1,k}-\frac{1}{h_x^2}\zeta^{m+1}_{j-1,k}-\frac{1}{h_y^2}\zeta^{m+1}_{j,k+1}-\frac{1}{h_y^2}\zeta^{m+1}_{j,k-1}]. \quad (20)$$

In order to solve the Poisson equation, the boundary condition for ψ is constructed from Eq. (15) in the following way:

$$\psi^{m+1}_{j,k}=\frac{H^2_{j,k}}{3T}[\frac{1}{h_x}(u^{m+1}_{j+1,k}-u^{m+1}_{j,k}-u^m_{j+1,k}+u^m_{j,k})+\frac{1}{h_y}(v^{m+1}_{j,k}-v^{m+1}_{j,k-1}-v^m_{j,k}+v^m_{j,k-1})]. \quad (21)$$

Description FNS-VOF Model

The FNS-VOF approach is used in this study to visualize differences and validate NLSW and NLB numerical models. The FNS equations include the vertical component of velocity/acceleration. The FNS-VOF approach solves a transient two-dimensional incompressible fluid flow with free surface. The finite difference solutions of the incompressible FNS equations are obtained on a rectilinear mesh.
Equation of continuity for incompressible fluid

$$\nabla \cdot \mathbf{u} = 0 \tag{22}$$

and the momentum equation

$$\frac{\partial \mathbf{u}}{\partial t} + (\mathbf{u} \cdot \nabla)\mathbf{u} = -\frac{1}{\rho}\nabla p + \nu \nabla^2 \mathbf{u} + \mathbf{g}, \tag{23}$$

are solved in a rectangular system of coordinates. Where $\mathbf{u}(x, y, t)$ is the velocity vector, ρ is the fluid density, p is the pressure, ν is the kinematic viscosity, $\mathbf{g}$ is the gravitational acceleration and t is the time. Solution of the equations is constructed using the two-step method, Chorin (1968); Harlow and Welch (1965). The time discretization of the momentum equation is given by

$$\frac{\mathbf{u}^{m+1} - \mathbf{u}^m}{T} = -(\mathbf{u} \cdot \nabla)\mathbf{u}^m - \frac{1}{\rho^m}\nabla p^{m+1} + \nu \nabla^2 \mathbf{u}^m + \mathbf{g} \tag{24}$$

and it is broken up into two steps as follows:

$$\frac{\tilde{\mathbf{u}} - \mathbf{u}^m}{T} = -(\mathbf{u} \cdot \nabla)\mathbf{u}^m + \nu \nabla^2 \mathbf{u}^m + \mathbf{g} \tag{25}$$

$$\frac{\mathbf{u}^{m+1} - \tilde{\mathbf{u}}}{T} = -\frac{1}{\rho^m}\nabla p^{m+1}. \tag{26}$$

Eq. (26) and the continuity equation (Eq. 22) can be combined into a single Poisson equation for the solution of the pressure as

$$\nabla \cdot [\frac{1}{\rho^m}\nabla p^{m+1}] = \frac{\nabla \cdot \tilde{\mathbf{u}}}{T}. \tag{27}$$

The free surface of the fluid is described by the discrete VOF function, introduced by Nichols and Hirt (1975) and Nichols *et al.* (1980). The Fluid is advected as a Lagrangian invariant, propagating according to

$$\frac{dF}{dt} = \frac{\partial F}{\partial t} + (\mathbf{u} \cdot \nabla)F = 0. \tag{28}$$

The scalar field $F(\vec{x}, t)$ is defined as:

$$F(\vec{x}, t) = \begin{cases} 1 & \text{in the fluid,} \\ 0 < F < 1 & \text{at the free surface,} \\ 0 & \text{in the void.} \end{cases}$$

OBSERVATIONS AND DISCUSSIONS

First, above numerical models are applied to a simplified case for the IOT (one-dimensional channel case) along transect A-A depicted in Fig. 2. This numerical experiment is intended to visualize dispersive effects using FNS-VOF model and test the NLSW (nondispersive) and NLB (dispersive) approaches. Transect A-A extends from 95.48^{o}E, 4.93^{o}N to 81.13^{o}E, 1.8^{o}S with total length of : 1745 Km. At both sides, the channel is bounded by walls, so the lateral interaction of waves is restricted, therefore, neither the wave is radiated from the channel nor outside signal is propagated into

channel. Model parameters and CPU time for the numerical computation are given in Table 1. The chosen time step ensures that water particles travel the computational cell in at least three time steps. In all models, several spatial resolutions have been applied to verify numerical convergence.

Model	δx	δz	δt	Num. of cells	CPU time
NLSW (Trans. A-A)	100 m	——	0.2 s	157059	30 min
NLB "	100 m	——	0.2 s	157059	5 h
FNS-VOF "	(5 – 875) m	(0.2 – 40) m	(0.08 – 0.8) s	800000	72 h

Table 1. Parameters for numerical computations along transect A-A (channel case)

Fig. 3 shows a series of free surface snapshots of the first 2 h of the IOT propagation based on the initial condition given by Kowalik *et al.* (2005). General features of the wave evolution agreed very well in all approaches. However, some differences in reproducing the dispersion phenomena become more noticeable as time advances. For instance, at time ≥ 40 min, the wave dispersion is evident according to NLB and FNS-VOF results. A train of waves which comprises multiple amplitudes and frequency components is formed immediately behind the leading wave. Major wave features are well reproduced by the NLSW method with exception of the train of waves. The leading NLSW wave is taller and shifted forward in space in relation to the dispersive solutions. The nondispersive NLSW approach overpredicts by ~28% the wave height at time 2 h 5 min. A slight advance in time (2 min 15 s) of the NLSW leading wave crest is observed as well. However, the wave front tip of the NLSW leading wave matches very well to its counterpart. This reaffirms the use of NLSW as an accurate approximation for determining the tsunami arrival time.

NLB and FNS-VOF model results agreed better in reproducing the detailed features such as the spatial and temporal distributions of the leading dispersive wave. However the NLB train which follows the leading wave is shifted forward in time with respect to FNS-VOF train. The shift increases in time as the wave diminishes in amplitude and length as shown in the zoomed window of Fig. 3. Values of $kh = (2\pi/L)h$ for the first, second and third waves at time 2 h 5 min according to FNS-VOF results are 0.17, 0.46 and 0.56 respectively ($h = 4810$ m). Their respective wavelengths are L =[179, 89 and 65]km, measured from trough to trough. Although the second and third waves fall into category of intermediate water wave regime ($0.31 < kh < 3.14$) the approximation of the dispersive term in the NLB model gives accurate estimate of the wave speed because the value of $kh < 1$ (Wei and Kirby, 1995). In comparison to the linear dispersion relation, the error is less than 1%. Although the second, third and subsequent NLB model waves shift slightly forward in relation to the FNS-VOF results, the NLB model predicts well the wave height, wave length and number of waves in the wave train.

The study is extended to visualize the wave dispersion effects in two-dimensions in the Bay of Bengal basin. Now, the computational domain is bounded by the window 78^{o}E, 1^{o}N to 100^{o}E, 14^{o}N. In this experiment, only NLB and NLSW models are used. At all open boundaries wave radiation condition is applied. Model parameters and CPU

time for the numerical computation are given in Table 2.

Model	δx	δy	δt	Num. of cells	CPU time
NLSW	1 min	1 min	3 s	1249600	16.0 min
NLB	1 min	1 min	3 s	1249600	1.5 h

Table 2. Parameters for the numerical computation for the two-dimensional case (Bay of Bengal)

Fig. 4 shows wave patterns at time 1 h 40 min using NLSW and NLB methods. Due to the dispersion effects the NLB model shows a series of wave behind the leading wave, therefore, wave patterns are significantly different from that of NLSW model. From the NLB model result, it is seen that length of the wave train in western region is longer than in the eastern region (close to Thailand and Indonesia). As Eqs. (13) and (14) suggest the magnitude of the dispersive term is proportional to the square of water depth, therefore, the dispersion effect in the western region ($H = 4\text{-}5$ km) is stronger than that in the eastern region (which is only of several hundred meters deep). Additionally the dispersion effect in the western region is enhanced through the longer distance of propagation.

Fig. 5 shows temporal variation of the free surface obtained by NLSW and NLB models at locations of numerical gauges given in Fig. 2. Again, over all agreement between nondispersive and dispersive models is very good. The same dispersive pattern is observed as in the channel along transect A-A. At gauge 1, agreement between dispersive and nondispersive solutions is excellent due to the proximity of the gauge to the tsunami source, as dispersive waves do not have time to develop. On the other hand, the sea level recorded at gauges 2 and 3, features dispersive waves since the gauges are located farther away from the tsunami source. The leading wave height is overpredicted again by the NLSW solution by 22% at gauge 2 and by 14% at gauge 3. A shift in time between leading wave crests is noticed as well; 50 s at gauge 2 and 1 min 5 s at gauge 3. Note the good agreement of the NLSW and NLB leading wave front tip in all gauge records.

The last experiment is intended to visualize the implication of dispersive effects on the runup. Two transects, B-B and C-C, have been chosen as indicated Fig. 2. One transect is in the Northwest of Sumatra (close to Banda Aceh); this location was struck by a "near-field" tsunami. In contrast, the other one across the Bay of Bengal, Sri Lanka (close to Yala), experienced a "far-field" tsunami. The rapid arrival of the tsunami to the near-field location in approximately 15 to 20 min, is juxtaposed with a longer arrival time of around 2 h to the far-field location. The numerical domains extend from 95.09^{o}E, 5.47^{o}N to 95.3^{o}E, 5.47^{o}N (transect B-B), and from 81.78^{o}E, 6.35^{o}N to 81.45^{o}E, 6.35^{o}N (transect C-C). At the offshore end of the channels the temporal variations of the free surface from the two-dimensional computation are established as boundary forcing. This experiment is intended to investigate the implication of dispersive effects on the runup, therefore, the two-dimensional contribution is avoided by constructing channels to visualize the approach of the wave train to the shoreline. Unfortunately, the 1 min

resolution is too coarse to represent a runup. For the purpose of this experiment a fine grid size was constructed in the models, using linear interpolation, to fill the gaps in the available bathymetry. A 10 m spatial resolution is applied in both experiments. Model parameters and CPU time for numerical computations are given in Table 3.

Model	δx	δy	δt	Num. of cells	CPU time
NLSW (Trans.B-B)	10 m	--	0.2 s	22680	4 min
NLB "	10 m	--	0.2 s	22680	30 min
NLSW (Trans.C-C)	10 m	--	0.2 s	34020	5 min
NLB "	10 m	--	0.2 s	34020	40 min

Table 3. Parameters for the numerical computation for one-dimensional cases: Banda Aceh, Sumatra (transect B-B) and Yala, Sri Lanka (transect C-C).

Figs. 6, 7 and 8 show tsunami propagation and runup in the coastal regions obtained by the NLSW and NLB models. In both experiments the computed maximum runup heights calculated by both methods are approximately 10 m. These results agree with the observed maximum runup in Yala (http://www.drs.dpri.kyoto-u.ac.jp/sumatra/srilanka-ut/SriLankaU_Teng.html), but underestimate the observed one in Banda Aceh (http://www.eri.u-tokyo.ac.jp/namegaya/sumatera/surveylog/eindex.htm).

Fig. 6 shows snapshots of the runup at Banda Aceh at extreme stages. Regardless of the models, free surface profiles, timing and runup heights match very well. Fig. 7 shows tsunami propagation on the continental shelf at Yala, Sri Lanka. As the wave approaches to the shoreline the dispersive effects are enhanced as revealed through the NLB solution. Subsequent snapshots at the shoreline (Fig. 8) show that the runup heights of the leading wave are almost the same in both models. However, Fig. 8c (3 h 7 min) shows that a higher runup is obtained by the NLB solution (37 min after leading wave runup), which is about 60% higher than the runup obtained by the NLSW model. Thus, dispersion consideration in numerical models is necessary for accurate prediction, since dispersion can produce significant differences in coastal runup. Dispersive waves interacting with the natural frequencies of the continental shelf, bay or harbor tend more often to generate resonance as compared to the long waves.

CONCLUSIONS

We have compared three approaches to compute tsunami, i.e., the nonlinear shallow water (NLSW nondispersive), the nonlinear Boussinesq (NLB) and the full Navier-Stokes aided by the volume of fluid method (FNS-VOF). The FNS-VOF method gives a frame of reference to validate the NLB and NLSW solutions. Since this approach introduces the vertical fluid velocity/acceleration and column-wise discretization, more accurate results are expected. However this method still requires higher computational resources, often not available for practical tsunami computations.

Comparison of the three different methods shows that for practical purpose the NLSW model results are quite reliable, since this model gives consistent results with its counterparts. The NLSW approach is very attractive nowadays for tsunami calculation because this method have very low computational cost and maximum wave height and

runup are often overpredicted, thus increasing safety factor. The NLSW results are useful for preliminary hazard assessment, where a simple and quick estimation of maximum wave height, maximum run-up and locations of maxima are required. Determination of the wave front tip location for the IOT is excellent. This reaffirms its use as an accurate method for determining the tsunami arrival time.

Qualitatively and quantitatively the wave fronts reproduced by the NLB and FNS-VOF solutions share many common features. For the longer integration time the similarity holds only for the main maximum, because the phase differences between secondary maxima increase with travel time (Fig. 3). Tsunami patterns away from the main front including runup have been reproduced by all three methods quite well and the sea level differences are quite small. The dispersion consideration in the numerical models is necessary for accurate prediction since it can produce significant differences in coastal runup when the wave front depicted in Fig. 7 will impinge on the coast creating complicated patterns of oscillations as compared to the NLSW solution given in Fig. 8. Such oscillations arriving to the continental shelf, bays or harbors may enhance the tsunami oscillations through the resonance. As Ortiz *et al.* (2001) pointed out the dispersion mechanism is not clearly established from the coastal observations, because such data are strongly influenced by the local bathymetry. Does IOT provide such validation? The general comparisons between data and NLSW model results given for IOT by Kowalik *et al.* (2005), Lay *et al.* (2005) and Hirata *et al.* (2005) are quite good even though these are nondispersive models. Preliminary results from the dispersive model of IOT presented by Watts *et al.* (2005) still require comparison with the NLSW. The computations in the nearshore regions will shed farther information on the dispersive versus nondispersive processes in IOT, however to undertake this direction fine resolution bathymetry is needed.

REFERENCES

Chorin, A. J. 1968. Numerical solution of the Navier-Stokes equations. *Math. Comp.* 22:745-762.

Dunbar, D., P. Leblond and T. S. Murty. 1991. Evaluation of tsunami amplitudes for the Pacific Coast of Canada. *Prog Oceanog.* 26: 115-177.

Fujima, K. 2001. Long wave propagation on large roughness. *ITS Proceedings, Sec. 7*, 7(22):891-895.

Goto, C. and N. Shuto. 1983. Numerical simulation of tsunami propagations and run-up. In *Tsunami-Their Science and Engineering*, edited by K. Iida and T. Iwasaki, pp 439-451. Tokyo: Terra Scientific Publ. Comp.

Harlow, F. H. and J. E. Welch. 1965. Numerical Calculation of time-dependent viscous incompressible flow of fluid with a free surface. *The Physics of Fluids* 8:2182–2189.

Heinrich, P., F. Schindele and S. Guiborg. 1998. Modeling of the February 1996 Peruvian tsunami. *Geophys. Res. Lett.* 25(14), 2687-2690.

Hirata, K. , K. Satake, Y. Tanioka, T. Kuragano, Y. Hasegawa, Y. Hayashi, and N. Hamada. 2005. The Indian Ocean Tsunami: Tsunami Source Model From Satellite Altimetry. *Proceedings of the International Tsunami Symposium*, edited by G.A. Papadopoulos and K. Satake, Chania Greece, pp 72-76.

Imamura, F., N. Shuto, and G. Goto. 1988. Numerical simulation of the transoceanic propagation of tsunamis. *th Congress Asian and Pacific Regional Division,*

International Association for Hydraulic Research, Kyoto Japan 6: 265-272.

Imamura, F. and N. Shuto. 1989. Tsunami propagation simulation by use of numerical dispersion. *International Symposium on Computational Fluid Dynamics* pp.390-395.

Imamura, F., N. Shuto and C. Goto. 1990. Study on numerical simulation of the transoceanic propagation of tsunamis. Part 2, Characteristics of tsunami propagation over the Pcific Ocean. *Zisin (J, Seismol. Soc. Japan)*, 43,389-402.

Kowalik, Z. and T. S. Murty. 1993a. *Numerical Modeling of Ocean Dynamics*, Singapore: World Scientific.

Kowalik, Z. and T. S. Murty. 1993b. Numerical Simulation of Two-Dimensional Tsunami Runup, *Marine Geodesy*, 16:87-100.

Kowalik, Z., W. Knight, , T. Logan, and P. Whitmore. 2005. Numerical Modeling of the Global Tsunami: Indonesia Tsunami of 26 December 2004. *Science of Tsunami Hazards* 23 (1): 40-56.

Kulikov, E. 2005. Dispersion of the Sumatra Tsunami Waves in the Indian Ocean detected by satellite altimetry. http://www-sci.pac.dfo-mpo.gc.ca/osap/projects/tsunami/documents/195610_0_merged_1107633516.pdf

Lay, T., H. Kanamori, C. J. Ammon, M. Nettles, S. N. Ward, R. C. Aster, S. L. Beck, S. L. Bilek, M. R. Brudzinski, R. Butler, H. R. DeShon, G. Ekstrom, K. Satake, S. Sipkin. 2005. The Great Sumatra-Andaman Earthquake of 26 December 2004. *Science*, 308: 1127-1139.

Liu P.L.-F., Y. B. Cho, S. B. Yoon and S. N. Seo. 1995. Numerical simulation of the 1960 Chilean tsunami propagation and inundation at Hilo, Hawaii. In *Tsunami Progress in Prediction, Disaster Prevention and Warning*, edited by Y. Tsuchiya and N. Shuto. Netherlands: Kluwer Academic Publisher.

Madsen, P. A., and H. A. Schaffer. 1999. A review of Boussinesq-type equations for surface gravity waves. In *Advances in Coastal and Ocean Engineering*, edited by P. L.-F. Liu, vol. 5, pp 1-94. Singapore: World Scientific.

Mader, C. L. 2004. *Numerical Modeling of Water Waves*, Boca Raton: CRC Press.

Nichols, B. D. and C. W. Hirt. 1975. Method for Calculating Multi-Dimensional, Transient Free Surface Flow Past Bodies. *Proc. of the 1st Int. Conf. Num. Ship Hydrodynamics*, Gaithersburg, Maryland.

Nichols, B. D., C. W. Hirt and R. S. Hotchkiss. 1980. SOLA-VOF: A Solution Algorithm for Transient Fluid Flow with multiple Free Boundaries. *LA-8355, Los Alamos National Laboratory*.

Okada, Y. 1985. Surface deformation due to shear and tensile faults in a half-space. *Bulletin of the Seismological Society of America* 75: 1135-1154.

Ortiz, M., E. Gómez-Reyes, H.S. Vélez-Muñoz. 2001. A fast preliminary estimation model for transoceanic tsunami propagation. *ITS 2000 Proceedings* 723-739.

Sato, S. 1996. Numerical simulation of 1993 southwest Hokkaido earthquake tsunami around Okushiri Island. *J. Waterway, Port, Coastal and Ocean Eng.* 122 (5): 209-215.

Shigihara, Y. 2004. A study on application of non-linear dispersive wave theory to the numerical simulation of tsunami. PhD Thesis, Dept. of Engineering, Tohoku University (in Japanese).

Shigihara, Y., K. Fujima, M. Homma and K. Saito. 2005. Numerical methods of linear dispersive wave equation for the practical problems. *Asian and Pacific Coasts, 2005*,

Sept. 4-8, Jeju, Korea, paper pp 14.

Yoon, S. B. 2002. Propagation of distant tsunamis over slowly varying topography. *J. Geoph. Res.* 107 (c10, 4-1): 4-11.

Watts, P., Ioualalen, M., Grilli, S., Shi, F., and Kirby, J. T. 2005. Numerical simulation of the December 26, 2004 Indian Ocean tsunami using high-order Boussinesq model, *Fifth Int. Symp. WAVES 2005, July, 2005, Madrid Spain*, 10pp.

Wei, G. and Kirby, J. T., 1995, A time-dependent numerical code for extended Boussinesq equations, *Journal of Waterway, Port, Coastal and Ocean Engineering*, **120**, 251-261

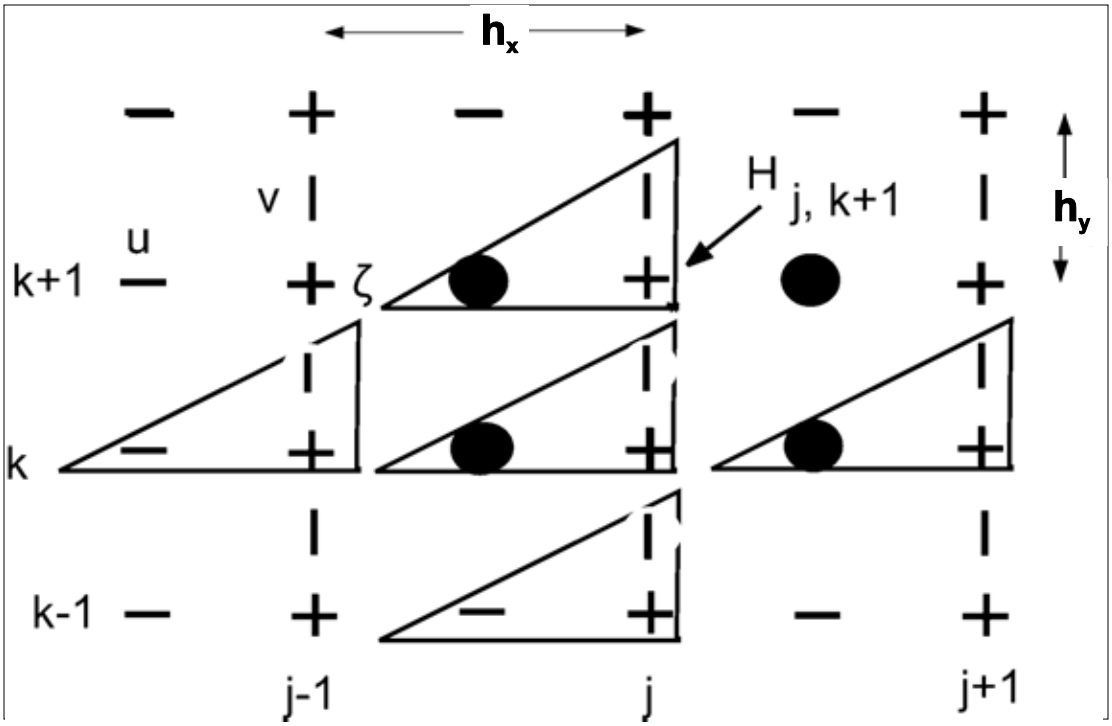

Figure 1. Spatial grid distribution .

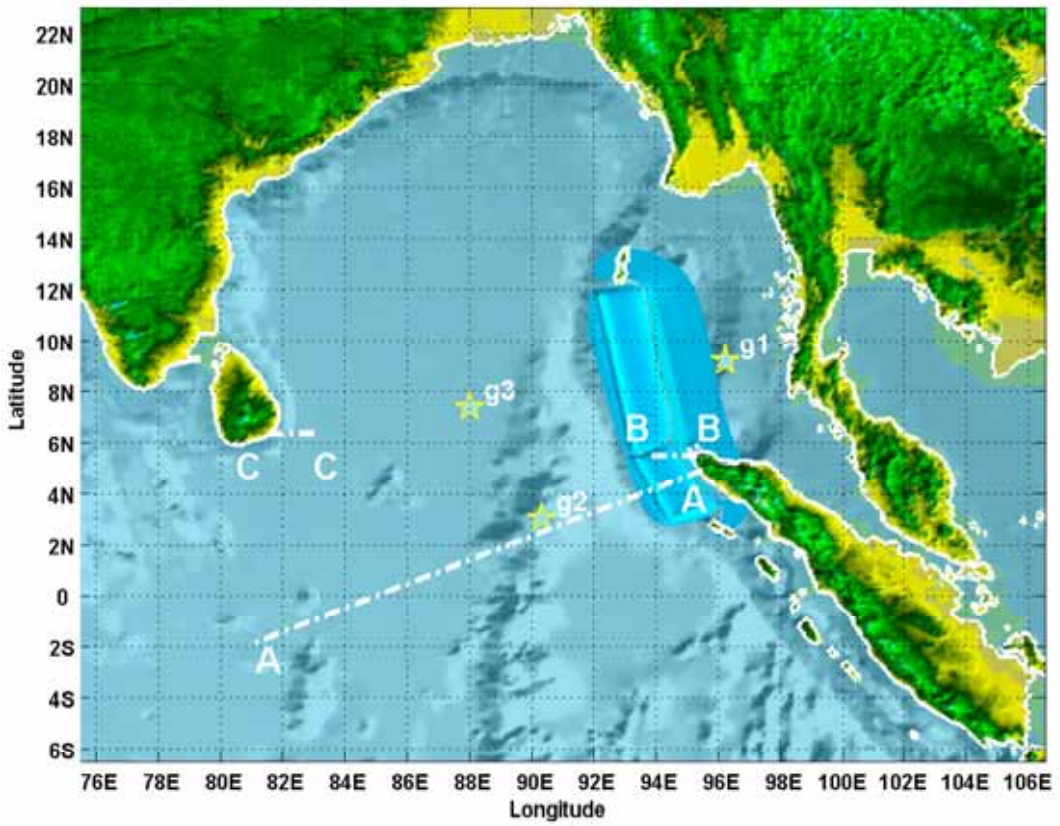

Figure 2. Indian Ocean bathymetry, initial free surface deformation and location of numerical gauges and transects

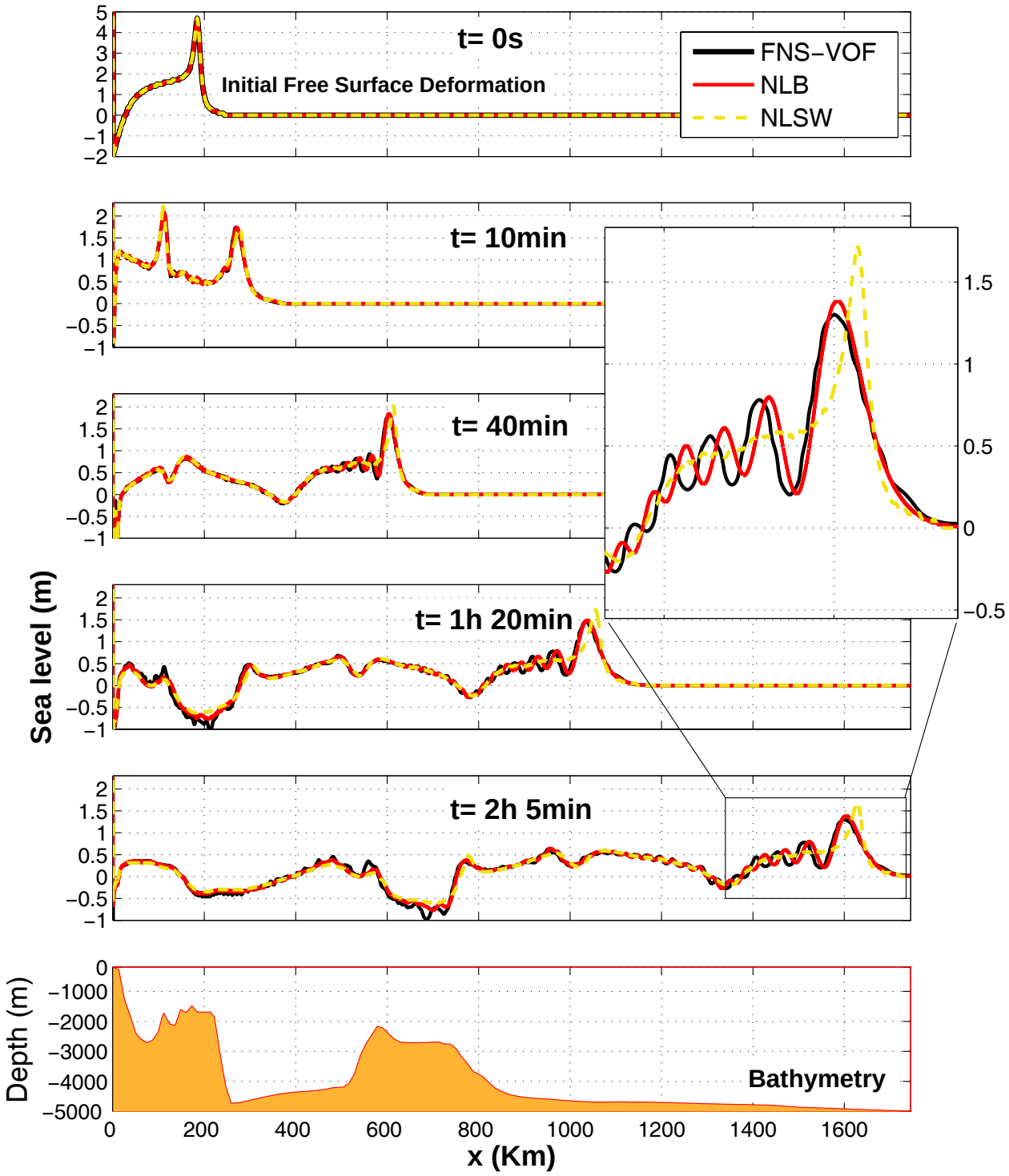

Figure 3. Tsunami propagation along transect A-A computed by three different methods

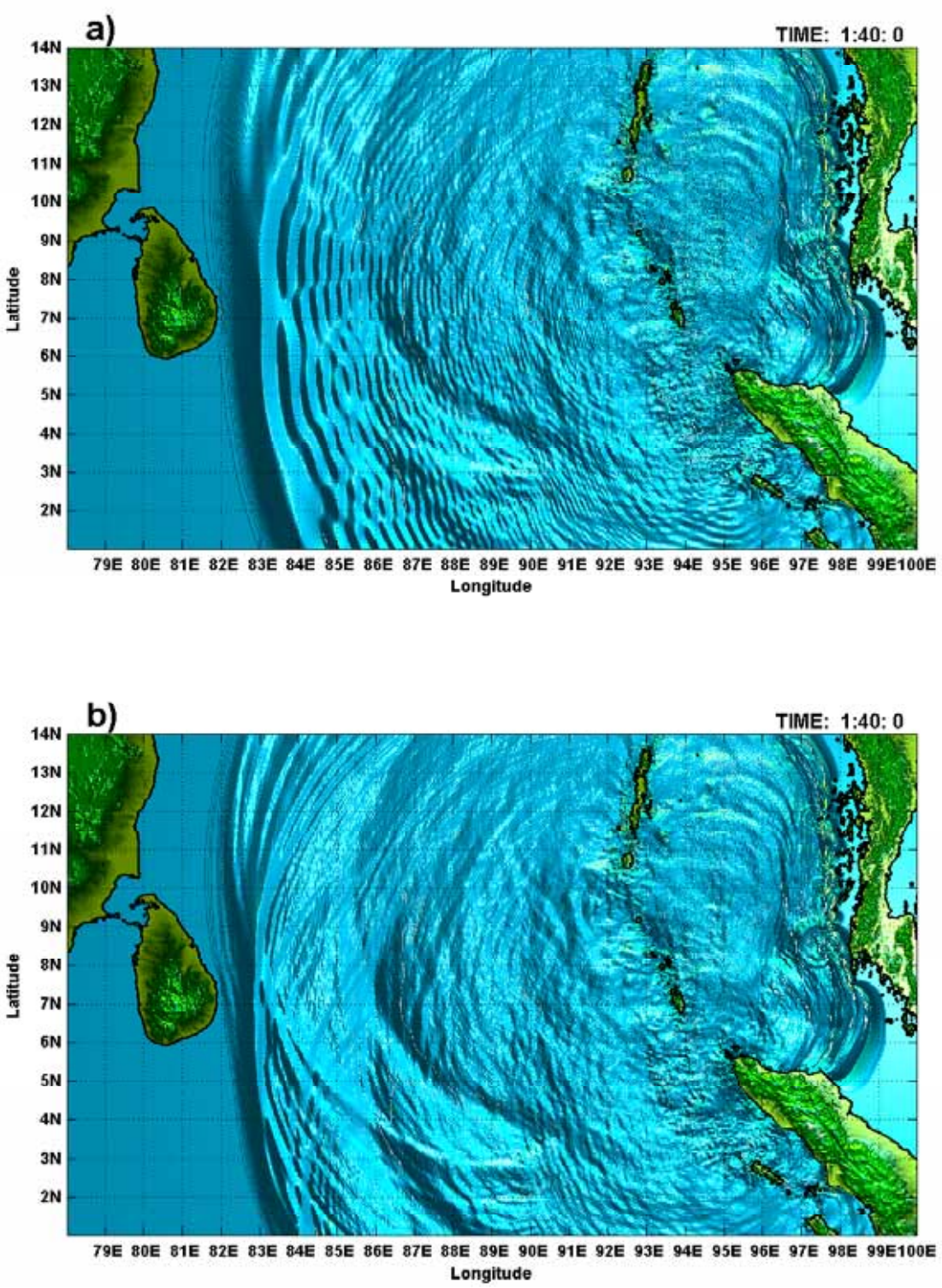

Figure 4. Comparison of water surface computed at 1h 40min from the onset of the earthquake: a) NLB model results, and b) NLSW model results

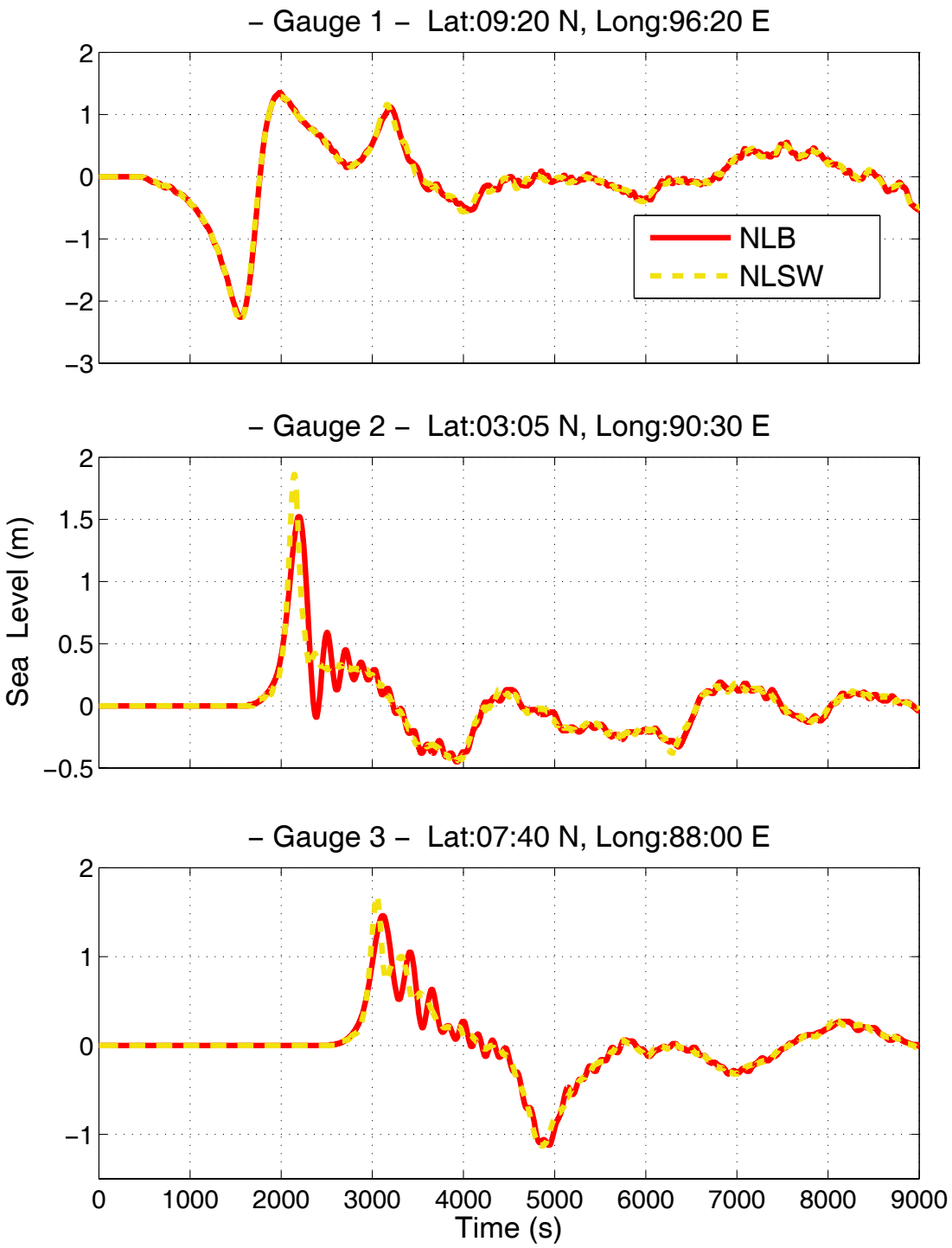

Figure 5. Comparison of water level at different locations (given in Fig. 2) obtained by NLB and NLSW models

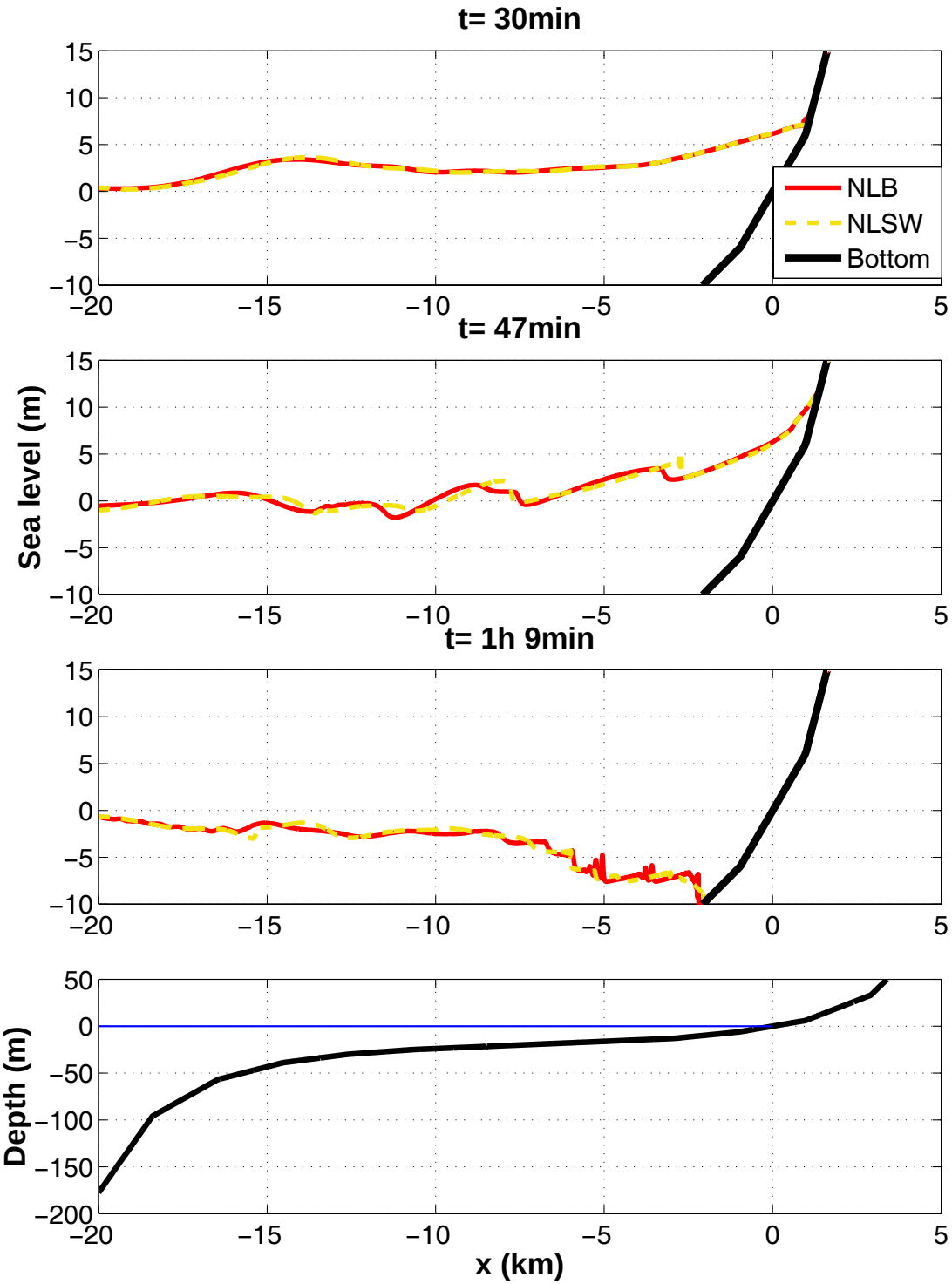

Figure 6. Comparison of tsunami runup/rundown at Banda Aceh, Sumatra (transect B-B), obtained by one-dimensional NLB and NLSW models.

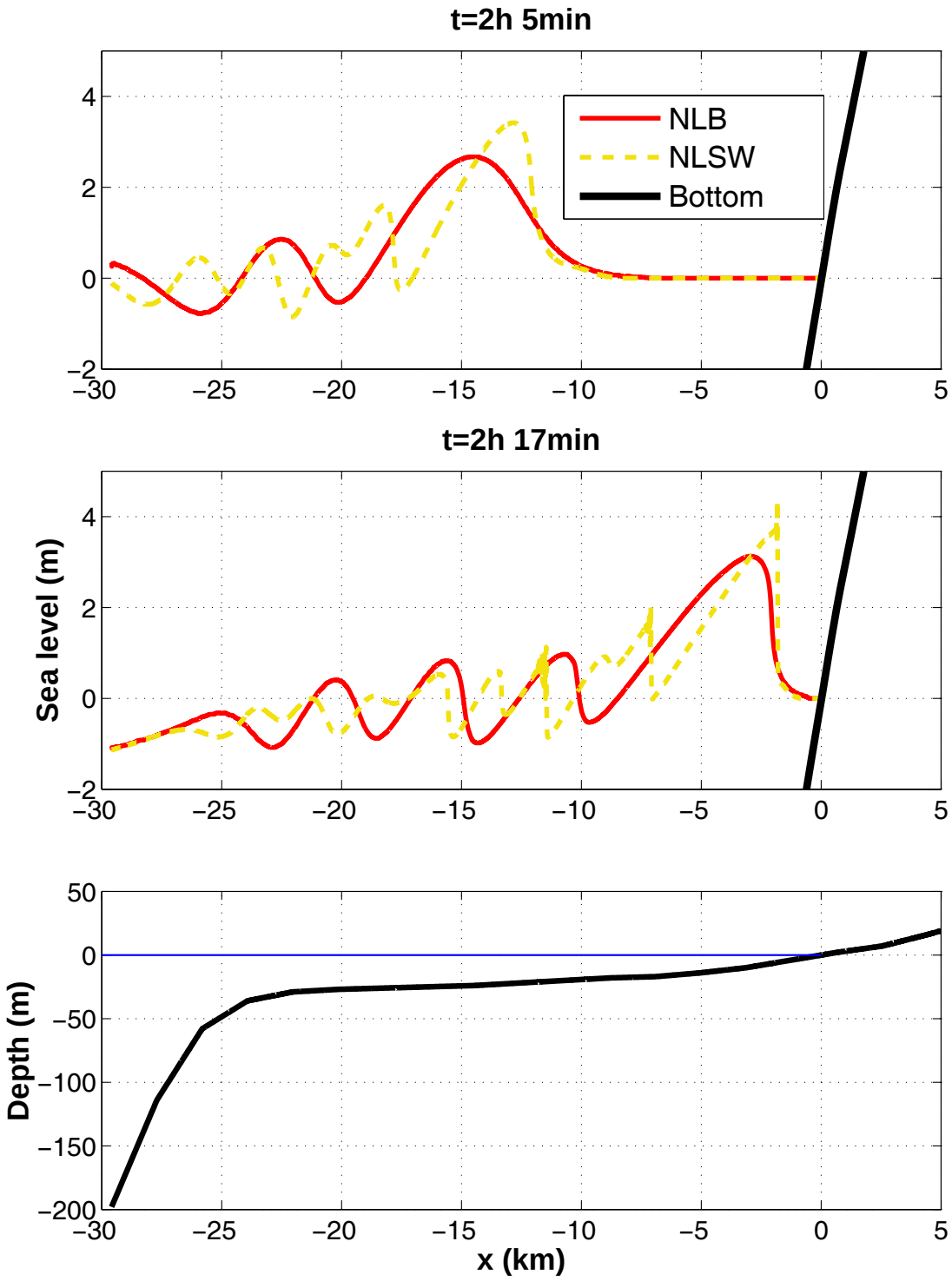

Figure 7. Comparison of tsunami propagation on the continental shelf at Yala, Sri Lanka (transect C-C), obtained by one-dimensional NLB and NLSW models.

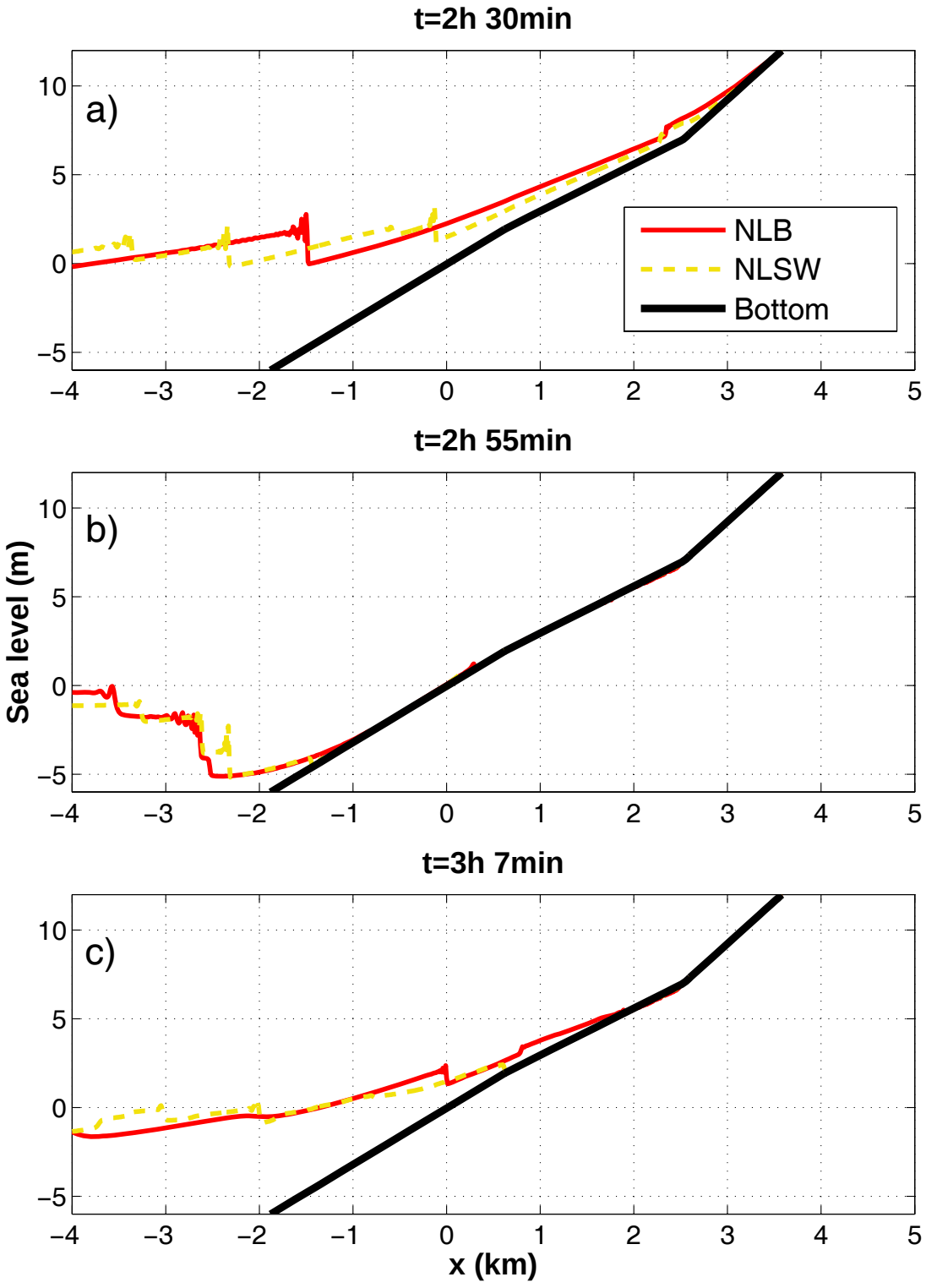

Figure 8. Comparison of tsunami runup/rundown at Yala, Sri Lanka (transect C-C), obtained by one-dimensional NLB and NLSW models.

Science of Tsunami Hazards, Vol 25, No. 1 (2006) ISSN 8755-6839

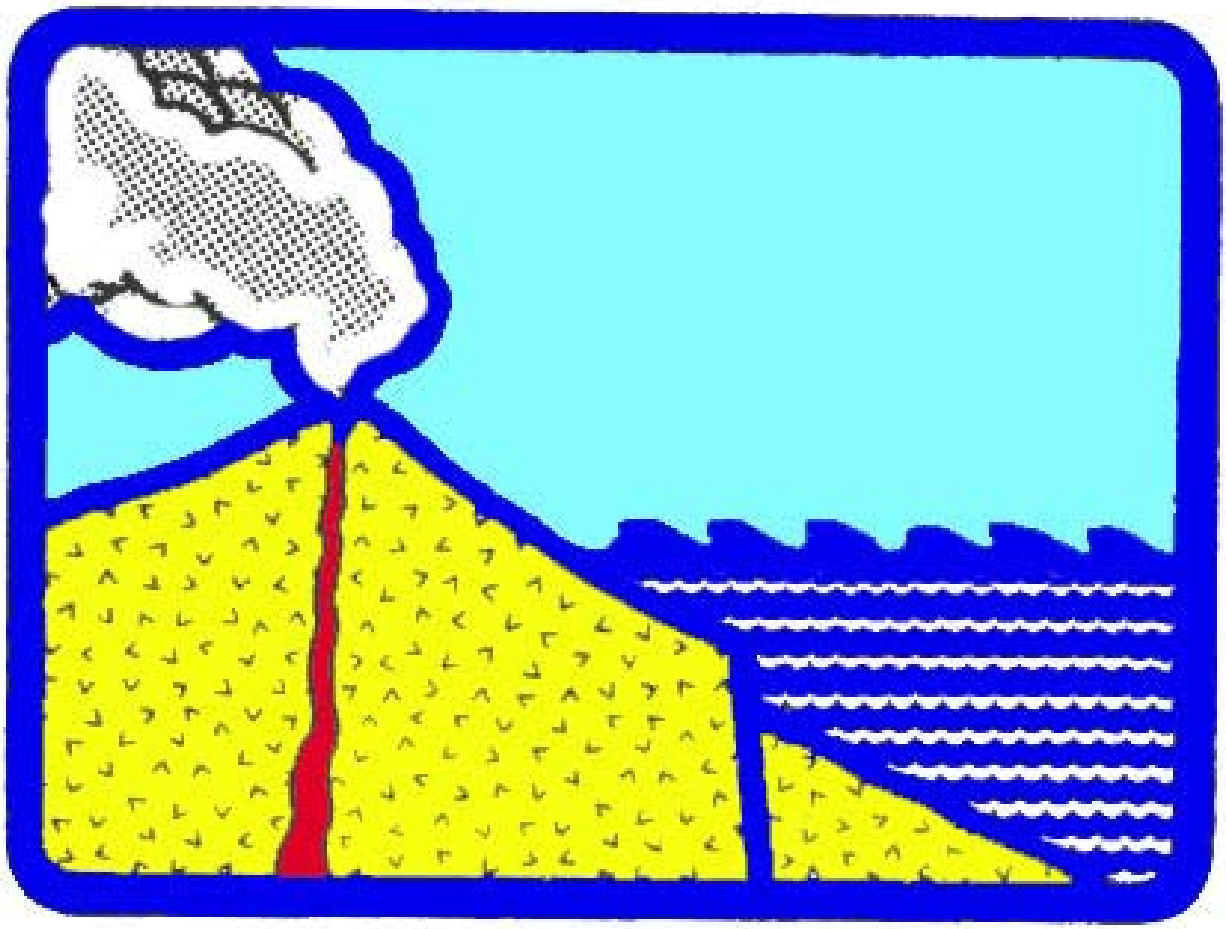

2523 Correa Rd, UH/SOEST, Rm 314 HIG
Honolulu, HI 96822, USA

WWW.STHJOURNAL.ORG